Dissertation

submitted to the
Combined Faculties for the Natural Sciences and for Mathematics
of the Ruperto-Carola University of Heidelberg, Germany
for the degree of
Doctor of Natural Sciences

Put forward by
Diplom-Physikerin Ulrike Böhm
Born in Kühlungsborn

Oral Examination: January, 13th 2016

4Pi-RESOLFT nanoscopy

Referees: Prof. Dr. Stefan W. Hell
Prof. Dr. Rainer H. A. Fink

In loving memory of my parents
Silvia and Karl-Heinz Böhm

Abstract

By enlarging the aperture along the optic axis, the coherent utilization of opposing objective lenses (4Pi arrangement) has the potential to offer the sharpest and most light-efficient point spread functions in three-dimensional (3D) far-field fluorescence nanoscopy. However, to obtain unambiguous images, the signal has to be discriminated against contributions from lobes above and below the focal plane, which has tentatively limited the 4Pi arrangements to the imaging of fixed samples with controllable optical conditions.
In this thesis, the 4Pi scheme was applied to RESOLFT nanoscopy using two-photon absorption for on-switching of fluorescent proteins and low-aberration sample optics. In this configuration, the lobes are so low that low-light level 3D-nanoscale imaging of living cells becomes possible. This methods thus offers robust access to densely packed, axially extended cellular regions that have been notoriously difficult to super-resolve. The approach also entails a fluorescence read-out scheme that translates molecular sensitivity to local off-switching rates into improved signal-to-noise ratio and resolution.

Zusammenfassung

Die Vergrößerung des Öffnungswinkels entlang des optischen Achse eines Mikroskopes durch die kohärente Überlagerung der Foki zweier sich gegenüberstehender Objektive (4Pi-Anordnung) ermöglicht die Erzeugung der lichteffizientesten und schärftesten Punktbildfunktionen, um die dreidimensionale Auflösung in der Fernfeldmikrokopie weit unter die Beugungsgrenze zu bringen. Um bei diesem Verfahren jedoch möglichst eindeutige Aufnahmen zu erhalten, müssen die detektierten Signale, von Hintergrundsignalen über- und unterhalb der Fokalebene getrennt werden. Bisher wurden deshalb hauptsächlich nur fixierte Proben untersucht, da deren Aufnahmebedingungen sehr gut kontrolliert werden können.
In dieser Arbeit stelle ich ein hochauflösendes 4Pi-Verfahren vor, das Aufnahmen von lebenden Zellen mit vernachlässigbarem Hintergrundsignal und Lichtschäden ermöglicht. Basierend auf RESOLFT Mikroskopie mit schaltbaren fluoreszierenden Proteinen und Zweiphotonenaktivierung und in Verbindung mit modifizierten Probenprotokollen und optimierter Optik zur Vorbeugung von Aberrationen, ermöglicht es einen robusten Zugang zu dicht gepackten, entlang der optischen Achse ausgedehnten, zellulären Regionen, die bislang weitesgehend vermieden wurden. Die Auflösung und die Signalqualität der Aufnahmen konnten zudem weiter durch die zeitliche Auswertung des Auslesesignals, auf Grund der hohen molekularen Sensitivität der entwickelten Methode auf lokale Schaltraten der Proteine, verbessert werden.

Contents

Contents

Abbreviations

2ph	two-photon
3D	three-dimensional
ac	activation
BPP	back pupil plane
conf	confocal
CW	continuous wave
det	detection
ef	effective
exc	excitation
FCS	fluorescence correlation microscopy
FWHM	full width at half maximum
GSD	ground state depletion
fl	fluorescence
IR	infrared
MTF	modulation transfer function
n	index of refraction
NA	numerical aperture
OTF	optical transfer function
PALM	photoactivatable localization microscopy
PSF	point spread function
RESOLFT	reversible saturable optical fluorescence transition
ro	read-out
RSFP	reversible switchable fluorescent protein
sat	saturation
SIM	structured illumination microscopy
SLM	spatial light modulator
SNR	signal-to-noise ratio
STED	stimulated emission depletion
STORM	stochastic optical reconstruction microscopy
TIRF	total internal reflection fluorescence
UV	ultraviolet

Chapter 1

Introduction

The 3–7 fold improved axial resolution provided by 4Pi microscopy [1–3] in the 1990s marked a first step in the quest for radically improving the resolution in far-field fluorescence microscopy. Yet the resolution provided by 4Pi microscopy remained diffraction-limited, because by jointly using two opposing lenses for focusing the excitation and/or the fluorescence light, this method just optimized the focusing conditions for feature separation. Modern far-field fluorescence nanoscopy [4], or superresolution microscopy, such as the methods called stimulated emission depletion (STED), reversible saturable optical fluorescence transitions (RESOLFT), and photoactivated localization microscopy (PALM)/stochastic optical reconstruction microscopy (STORM) fundamentally departed from such early concepts by discerning features through a molecular state transition. The use of state transitions for feature separation, typically a transition between a fluorescent (ON) and a non-fluorescent (OFF) state, opened the road to lens-based fluorescence microscopy with resolution that is conceptually not limited by diffraction.
Yet diffraction plays a role in these 'diffraction-unlimited' techniques because the resolution of these 'nanoscopy' methods still benefits strongly from focusing the light as sharply as possible. Whereas in STED and RESOLFT it is the focusing of the illumination light in sample space that matters, in PALM/STORM it is the focusing of the emitted light at the detector. Therefore the optimization of focusing remains very timely. 4Pi arrangements can also facilitate the doubling of the detected fluorescence without compromising the resolution in the focal plane (x,y) and offer significantly sharper axial (z) intensity gradients than single lenses for both the illumination and the detected light. Consequently, the combination of 4Pi with STED, RESOLFT and PALM/STORM approaches currently offers the most powerful optical setting for three-dimensional fluorescence nanoscopy [5–7].
However, 4Pi-type superresolution arrangements are scarcely reported for STED and PALM and are entirely unexplored for RESOLFT, a STED-derivative that typically uses reversibly switchable fluorescent proteins (RSFPs) for providing the

mandatory ON and OFF states. RSFP-based RESOLFT is particularly attractive because it operates with low light levels which makes it gentle to living cells.

In this thesis, I report the first realization of 4Pi-RESOLFT nanoscopy, i.e. of a conceptually diffraction-unlimited resolving method which, by virtues of 4Pi microscopy, provides spatially uniform 3D resolution for imaging (living) cells at the nanometer scale, and operates at low light levels.

The difficulties in realizing a 4Pi setup are commonly attributed to the counter-alignment of the two high numerical aperture lenses. In practice, however, the alignment can be controlled and stabilized over many hours. Instead, a far more general problem that is inherent to all fluorescent imaging modalities comes to the fore. The fluorescence signal (that emanates from each sub-diffraction pixel volume under investigation) needs to be discriminated against 'background' signal from outside of this volume. This 'background' largely stems from optical aberrations that preclude precise spatial control of the illuminating or fluorescent beam positions and, in case of STED, RESOLFT or PALM/STORM, from imperfections in the ON/OFF state (switching) process. Discrimination against this 'background' signal is most challenging along the optical (z) axis, especially when the probed volume is of sub-diffraction dimensions. The lack of sufficient discrimination along the z-axis (optical sectioning) manifests itself as artifacts in the image, in particular as 'ghost features' above and below the real features.
When describing the imaging process in the spatial frequency domain, the appearance of axial lobes corresponds to local depressions in the amplitude of the optical transfer function, i.e. the modulation transfer function (MTF) of the microscope. Structural information of the sample can only be retrieved in those spatial frequency bands where the MTF is strong enough to convey a signal that sufficiently exceeds the local noise level. In a 4Pi microscope, MTF depressions are typically restricted to sharp local minima at the so-called critical frequencies [8]. As their amplitude strongly depends on the aperture angle α of the objective lenses used [8], combinations of 4Pi with diffraction-unlimited superresolution/nanoscopy methods such as isoSTED [5,9,10] and iPALM [6,11], have unfortunately been limited to imaging fixed samples that are more easily accessible with high angle lenses ($\alpha \leq 74°$, as for oil immersion lenses with numerical aperture NA ≥ 1.46). Furthermore, the imaged objects were rather thin and labeled very sparsely. Both of these properties ease the requirements on optical sectioning, i.e. on suppressing the signal ('background') from above and below the focal plane.
In course of this thesis, I will show how the developed and implemented combination of 4Pi microscopy and RESOLFT nanoscopy tackles the above mentioned issues successfully such that robustly imaging of densely labeled and axially extended living cells becomes possible.

1.1 Outline of the thesis

The thesis is structured as follows:

Chapter 2 gives an introduction to image formation in far-field light microscopy (2.1) and diffraction-unlimited fluorescence microscopy (2.2). Then the basic concepts of the developed and implemented 4Pi-RESOLFT nanoscopy scheme are described (2.3).

Chapter 3 summarizes the experimental realization of the 4Pi-RESOLFT nanoscope. This includes detailed descriptions of the used switching patterns for 3D nanoscopy (3.1), the microscope design (3.2), the data acquisition (3.3), the special 4Pi sample mount for live-cell imaging (3.4) and the 4Pi unit operation (3.5).

Chapter 4 demonstrates how the 4Pi-RESOLFT scheme already offers huge advantages for the optical sectioning capability in 4Pi microscopy even without the implementation of a '3D-doughnut' deactivation pattern for super-resolved images. First the principles of this approach are explained and compared to former approaches (4.1). Then the first results are presented (4.2) and the potential of this method is discussed (4.3).

Chapter 5 describes how the system is used for three-dimensional 4Pi-RESOLFT nanoscopy when implementing a '3D-doughnut' deactivation pattern. First the basic principles are described and compared to former approaches (5.1). Then a rate-gated fluorescence read-out scheme which was developed and implemented for the 3D 4Pi-RESOLFT nanoscopy scheme is introduced (5.2). Finally the first results are shown (5.3) and the potential of this method is discussed. (5.4).

Chapter 6 summarizes the results of this study and gives an outlook for future developments.

Chapter 2

Theoretical foundations

The following chapter describes the theoretical foundations of the developed 4Pi-RESOLFT imaging scheme.
In the first section (2.1), the principles of image formation in far-field light microscopy are explained. Key aspects are the diffraction limit in microscopy and early approaches like 4Pi microscopy to push this barrier. The second section (2.2) introduces super-resolution fluorescence imaging techniques like STED, RESOLFT and PALM / STORM. It explains how these techniques take advantage of the transition between different molecular states (ground, excited, and dark states) of fluorescent labels in order to overcome the limiting role of diffraction. The last section (2.3) describes the developed and realized concepts of 4Pi-RESOLFT nanoscopy, a new approach for low-light level 3D-nanoscale imaging of living cells.

2.1 Image formation in far-field light microscopy

Let a point-like source S be imaged to a point F by an ideal lens. This point source can be for example a single fluorophore whose fluorescence is imaged onto a detector. Due to the wave nature of light, its image is blurred to a 3D distribution around F, called the focal spot. The electric field distribution $E(\vec{r})$ can be described according to the 3D scalar diffraction theory using Fresnel approximation [12]:

$$E(\vec{r}) = A \int_0^\alpha \sqrt{\cos\theta} \sin\theta J_0\left(k\sqrt{x^2+y^2}\sin\theta\right) \exp(ikz\cos\theta) d\theta \tag{2.1}$$

where A denotes a normalization constant, J_0 is the zero order Bessel function of first kind, θ denotes the polar aperture angle and α is its maximum. The wave number k is defined as $k = 2\pi n/\lambda_0$ with λ_0 the vacuum wavelength and n the refractive index. The field distribution is also called amplitude point spread function (PSF).
Since most electronic detectors see the intensity rather than the electric field, it is instructive to define the intensity distribution or point spread function which is given by the square of the absolute value of the amplitude PSF:

$$h(\vec{r}) = |E(\vec{r})|^2 \tag{2.2}$$

This PSF is cylindrical symmetric and its maximum resides at the focal point. The intensity distribution is clearly elongated along the z direction. Furthermore, the intensity profile in the focal plane features a pronounced main maximum and progressively weaker minima and maxima which can be easily seen in the semi-logarithmic plots (Figure 2.1). The pattern is referred to as Airy pattern and the central region which extends to the first zero is known as the Airy disk [13].
This image construction can be expanded from one single point source to a 3D self-luminous object (e.g. a distribution of fluorophores) by integrating the images of every single emitter of the object. The image $I(\vec{r})$ of an object emitter density $O(\vec{r})$ is therefore given by the convolution ($\otimes$) of the object with the PSF $h(\vec{r})$:

$$I(\vec{r}) = \int O(\vec{r}') \cdot h(\vec{r} - \vec{r}') d\vec{r}' = O(\vec{r}) \otimes h(\vec{r}) \tag{2.3}$$

Note that the image of the object is blurred by the PSF. In order to create a sharp image, it is necessary that the PSF is as well localized as possible.
The imaging process which is characterized by the PSF in the spatial domain can also be considered from a frequency domain view. Here, the object and the image are described by their spatial frequencies. The imaging system is therefore

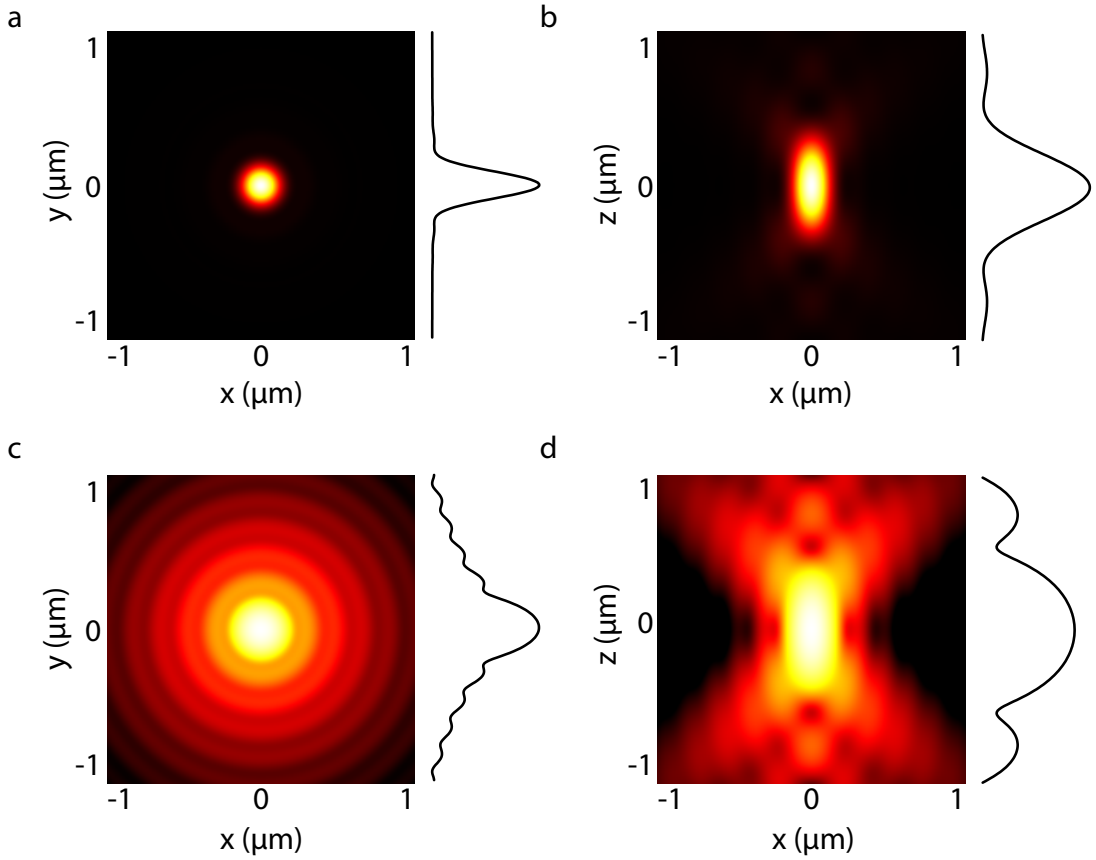

Figure 2.1: Airy disk resulting from a point source. Projections of the intensities of the whole focus onto the xy and xz planes, (a,b) in linear scale, (c,d) in logarithmic scale. The plots to the of the images show the normalized cross section through the middle of the displayed PSF. Simulation parameters: NA = 1.4, λ = 491 nm.

characterized by its transmittance of spatial frequencies. Fourier transformation of equation 2.3 and application of the convolution theorem yields

$$\mathcal{F}(I(\vec{r})) = \mathcal{F}(O(\vec{r}) \otimes h(\vec{r})) = \mathcal{F}(O(\vec{r})) \cdot \mathcal{F}(h(\vec{r})) \tag{2.4}$$

The frequency spectrum of the image $\mathcal{F}(I(\vec{r}))$ is thus given by the product of the frequency spectrum of the object $\mathcal{F}(O(\vec{r}))$ and the Fourier transform of the PSF $\mathcal{F}(h(\vec{r}))$. If $\mathcal{F}(h(\vec{r}))$ has very small or zero amplitudes for particular spatial frequencies, these frequencies are transmitted very badly or not at all by the microscope. Consequently, details of the object which are described by these spatial frequencies are missing in the image and cannot be reconstructed from it. The

normalized Fourier transform of the PSF is usually referred to as the optical transfer function (OTF). Its absolute value, the modulation contrast function (MTF), measures how faithfully contrast (modulation) is transmitted. The MTF is used later to evaluate the performance of the built nanoscope.

2.1.1 Diffraction limit

In 1873, the physicist Ernst Abbe first realized that the resolution of optical imaging instruments is fundamentally limited by the diffraction of light [14]. His finding indicated that ultimately the resolution of an imaging instrument is not only constrained by the quality of the instrument, but also by the wavelength of light used and the aperture of its optics. He stated that a microscope could not resolve two objects located closer than $\lambda/2\mathrm{NA}$, where λ is the wavelength of light and NA is the numerical aperture of the imaging lens. His theory was later refined by John William Strutt 3^{rd} Baron Rayleigh in 1896. According to the Rayleigh criterion [15], two incoherently radiating point sources can still be separated if the main maximum of the Airy pattern of one image falls into the first minimum of the other images. The Airy disk's radius serves therefore as a measure for the resolution Δr in the lateral direction:

$$\Delta r = 0.61 \frac{\lambda_0}{\mathrm{NA}} \tag{2.5}$$

Analogous to Δr, the resolution in the axial direction Δz (often called depth of field) can be defined to be half the distance between the first minima.

$$\Delta z = 2.00 \frac{n\lambda_0}{\mathrm{NA}^2} \tag{2.6}$$

The Airy pattern is often approximated by a Gaussian which fits the main maximum quite well and only omits the weak rings. The resolution in the lateral direction $\Delta\tilde{r}$ and in the axial direction $\Delta\tilde{z}$ can then be conveniently defined by its full width at half maximum (FWHM):

$$\Delta\tilde{r} = 0.51 \frac{\lambda_0}{\mathrm{NA}} \tag{2.7}$$

and

$$\Delta\tilde{z} = 1.77 \frac{n\lambda_0}{\mathrm{NA}^2} \tag{2.8}$$

z-response

A good benchmark for the optical sectioning capability of an imaging system is its z-response [2], which corresponds to the detected fluorescence emitted by an infinitesimal thin layer parallel to the xy plane whose position is scanned along the z axis:

$$h_{\mathrm{Z}}(z) = \int h_{\mathrm{ef}}(\vec{r})dxdy \tag{2.9}$$

If a microscope system is capable of optical sectioning, its z-response rapidly decreases for increasing distance between the fluorescent layer and the focal plane. This measure is used later to evaluate the optical sectioning capabilities of the built nanoscope.

2.1.2 Pushing the limits of the diffraction barrier

Several ideas have been put forth to address the resolution problem in far-field optics.

Confocal microscopy

In a spot-scanning confocal microscope the sample is illuminated with a diffraction-limited focused spot and the fluorescence emission is confocally detected with a symmetrically arranged point detector, which is usually realized by inserting a detection pinhole. The intensity distribution of the imaged light source is the read-out (illumination) PSF $h_{\mathrm{ro}}(\vec{r})$ of the system. The intensity distribution created by an emitter of the sample on the detector is the detection PSF $h_{\mathrm{det}}(\vec{r})$ of the system. The effective PSF of a confocal microscope is given by the product of both intensity distributions. It is denoted by

$$h_{\mathrm{conf}}(\vec{r}) = h_{\mathrm{det}}(\vec{r}) \cdot h_{\mathrm{ro}}(\vec{r}) \tag{2.10}$$

in the limiting case of an infinitesimal small detection pinhole. However, in practice, a finite pinhole size is necessary in order to collect sufficient signal. The real detection PSF if given by the 2D convolution of the detection PSF $h_{\mathrm{det}}(\vec{r})$ with the pinhole function $p(\vec{r})$. The function $p(\vec{r})$ describes the opening of the detector that is conjugated to the focal plane, e.g. the area of a confocal pinhole. If no pinhole is used, $p(\vec{r}) = 1$.
The confocal detection does not, however, really provide a higher resolution. Theoretically, the width of the effective focal spot or PSF is reduced by a factor of

$\sqrt{2}$ [16–18]. This improved spatial information is however usually heavily damped and thus lost in noise. The biggest benefit of detecting through a pinhole is a superb background rejection, which significantly improves 3D-imaging and which is the reason why the confocal laser scanning microscope was for a long time considered as the workhorse of fluorescence 3D-microsocpy.

Two-photon fluorescence microscopy

Another approach that has often been connected with resolution improvement is the use of two-photon excitation. Here, the simultaneous absorption of two photons results in excitation of the fluorophore. The wavelength of the excitation light is thereby usually chosen to be double the wavelength λ that would be used for conventional one-photon excitation [19–21]. The resulting non-linear squared dependence of the fluorescence emission on the excitation intensity establishes a clear reduction of the width of the effective focal spot or PSF by a factor of $\sqrt{2}$. Unfortunately, doubling the wavelength (2λ) comes with a doubling of the size of the diffraction spot, i.e. in total the spatial resolution of a two-photon microscope is usually slightly poorer than its one-photon counterpart [22]. The same arguments are valid for m-photon absorption processes, because they usually require an even longer wavelength $m\lambda$. The advantage of a multi-photon microscope lies in other factors such as a deep penetration depth, low scattering, the restriction of photobleaching to the focal spot and the capability of producing confocal imaging properties (e.g., sectioning) without using a point detector.
The effective PSF in two-photon microscopy is given by

$$h_{\mathrm{2ph}}(\vec{r}) = h_{\mathrm{ro}}^2(\vec{r}) \tag{2.11}$$

If a point detector is added in a confocal arrangement, the PSF is given by

$$h_{\mathrm{2ph,conf}}(\vec{r}) = h_{\mathrm{det}}(\vec{r}) \cdot h_{\mathrm{ro}}^2(\vec{r}) \tag{2.12}$$

4Pi confocal fluorescence microscopy

In the two previously described imaging techniques, the axial resolution is lower than the lateral resolution (Figure 2.1). An intuitive explanation for the elongation along the optical axis is that the converging spherical wavefront is only a section of a complete spherical wavefront. If a complete spherical wavefront with uniform amplitude were to be used, the PSF would have a spherical shape and the elongation would vanish. Following this reasoning, the aperture of a confocal fluorescence microscope can be enhanced with a second microscope objective placed opposite

the first one. When both illuminate the common focal point with coherent wavefronts and constructive interference takes place, the read-out (illumination) PSF approaches a more spherical shape and the axial resolution is enhanced. A similar consideration applies also to the confocal detection. Thus, the basic idea of the 4Pi confocal fluorescence microscope is to use two microscope objectives with a common focus to increase the aperture of the microscope (Figure 2.2a) which in turn increases the system's axial resolution and improves its optical sectioning capability [2]. Since a solid angle of 4π is practically not achievable, the term 4Pi was chosen to indicate the basic idea with a simple and straightforward term. Unfortunately, the interference of incomplete spherical wavefronts also produces so-called sidelobes that are located at about half a wavelength above and below the focal plane (Figure 2.2b). Moreover, these primary lobes are accompanied by weaker periodic lobes that increase in height with decreasing semi-aperture angle α of each objective lens. The lobes produce ghost images that have to be removed by mathematically post-processing the 3D data. The accuracy with which these ghost images can be removed depends on the relative height of the sidelobes compared to the main peak. As a rule of thumb, the primary lobe height should never exceed ~ 50 % of the main focal spot. Furthermore, note that although 4Pi microscopy improves the resolution along the optic axis, the lateral resolution remains the same as in confocal microscopy.
4Pi confocal fluorescence microscope comprises three different types of imaging that feature higher axial resolution [23]. Their effective PSFs are given by

Type-A: Only the two read-out wavefronts interfere in the sample:

$$\begin{aligned} h_{\text{4Pi-A}}(\vec{r}) &= h_{\text{det}}(\vec{r}) \cdot h_{\text{4Pi,ro}}(\vec{r}) \\ &= |\vec{E}_{\text{det}}(\vec{r})|^2 \cdot |\vec{E}_{1,\text{ro}}(\vec{r}) + \vec{E}_{2,\text{ro}}(\vec{r})|^2 \end{aligned} \tag{2.13}$$

Type-B: Only the two detection wavefronts interfere in the detector:

$$\begin{aligned} h_{\text{4Pi-B}}(\vec{r}) &= h_{\text{4Pi,det}}(\vec{r}) \cdot h_{\text{ro}}(\vec{r}) \\ &= |\vec{E}_{1,\text{det}}(\vec{r}) + \vec{E}_{2,\text{det}}(\vec{r})|^2 \cdot |\vec{E}_{\text{ro}}(\vec{r})|^2 \end{aligned} \tag{2.14}$$

Type-C: Both the detecting and the read-out wavefronts interfere:

$$\begin{aligned} h_{\text{4Pi-C}}(\vec{r}) &= h_{\text{4Pi,det}}(\vec{r}) \cdot h_{\text{4Pi,ro}}(\vec{r}) \\ &= |\vec{E}_{1,\text{det}}(\vec{r}) + \vec{E}_{2,\text{det}}(\vec{r})|^2 \cdot |\vec{E}_{1,\text{ro}}(\vec{r}) + \vec{E}_{2,\text{ro}}(\vec{r})|^2 \end{aligned} \tag{2.15}$$

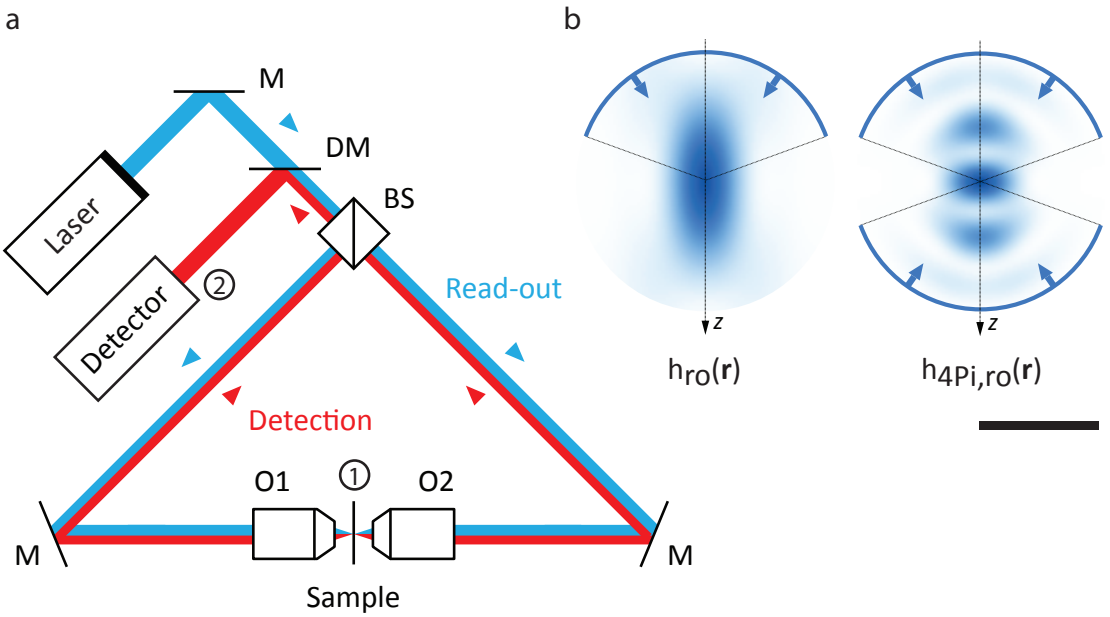

Figure 2.2: Principles of 4Pi microscopy. (a) Sketch of a 4Pi microscope. Read-out light originating from a laser is divided by a beam-splitter (BS) and focused onto the same spot by the opposing lenses $O1$ and $O2$. Fluorescence is collected by both lenses, recombined at the BS and directed towards a detector. Interference takes place during the read-out in the sample (1) and / or at the detector (2) depending of the 4Pi imaging type; M: mirror, DM: dichroic mirror. (b) xz-sections of a confocal read-out PSF $h_{\mathrm{ro}}(\vec{r})$ and a 4Pi read-out PSF $h_{\mathrm{4Pi,ro}}(\vec{r})$. Scale bar: 500 nm.

Here $\vec{E}_{\text{1-2,det}}(\vec{r})$ and $\vec{E}_{\text{1-2,ro}}(\vec{r})$ denote the electric field from each objective lens at the detection and the read-out.
All 4Pi imaging types can be realized with multi-photon read-out which improves in particular the imaging performance of type-C 4Pi microscopy. Two-photon type-C 4Pi microscopy obtains an ~ 30 % better resolution than its type-A counterpart, and its sidelobes are below 10 % of the height of the central maximum. A detailed description of multi-photon type-C 4Pi PSFs is given in section A.1.
But although the 3–7 fold improved axial resolution has allowed the observation of living cellular structures with larger detail and has given a significantly improved insight into cellular functions [24–28], the spatial resolution of this technique is still limited, i.e. it does not break the diffraction barrier, but it rather pushes diffraction to its limits.

2.2 Breaking the diffraction barrier

A real breakthrough for the surpassing of the diffraction barrier was the insight that the properties of the fluorophore itself can be used to attain unlimited (actually molecular-size) spatial resolution in the far-field [29–31]. It was realized that one can take advantage of the transitions between different states of the fluorescent label, i.e. its spectroscopic properties, to modify the fluorescence emission in such a way as to overcome the limiting role of diffraction [29]. Until then, fluorophores were primarily regarded as indicators of molecular species or environmental conditions (such as pH, ion concentrations). That they should also hold the key to nanoscale resolution in a far-field microscope was a major change in the perception of this idea. Stimulated emission depletion (STED) [31–33], ground state depletion (GSD) [30, 34] and reversible saturable optical fluorescence transition (RESOLFT) [35–37] microscopy emerged as the first concrete and viable physical concepts to overcome the limiting role of diffraction in a lens-based optical microscope (Section 2.1.1). While these approaches reversibly inhibit the occupation of a molecular state (usually the emissive state) at defined spatial coordinates using deterministic scanning (coordinate-targeted approaches, Section 2.2.1), subsequent developments such as (fluorescence) photoactivation localization microscopy (FPALM) ((F)PALM) [38, 39] or stochastic optical reconstruction microscopy (STORM) [40] transfer the fluorophores to their emissive state stochastically in space and utilize the spatial localization of single isolated molecules based on the fluorescent labels with discernible emission properties (coordinate-stochastic approaches, Section 2.2.2). The most prominent example is a pair of a bright (fluorescent) ON- and a dark (non-fluorescent) OFF-state, where at least one transition such as the ON-to-OFF transition is driven by light. The molecular states involved do not necessarily have to be dark and bright states. They can also differ in other fluorescence properties such as absorption cross-section, emission wavelength, fluorescence lifetime or other properties, i.e. their detected signal has to be discernible. For simplicity, we keep to the notation of ON- and OFF-states and denote the light driving the OFF-ON and ON-OFF transition by 'turn-on' and 'turn-off' light.

2.2.1 The coordinate-targeted nanoscopy

The initially developed coordinate-targeted approaches STED, GSD or RESOLFT utilize an illumination pattern (Figure 2.3a). Specifically, an intensity distribution of either the turn-on or turn-off laser light is created that features at least one intensity zero to transiently confine the occupation of usually the ON-state, i.e. the fluorescence emission, to sub-diffraction sized areas or volumes. Increasing the intensity of this modified laser above a certain threshold basically turns off the detected fluorescence emission. The restriction of the occupation of ON-states and

thus (detected) fluorescence emission to sub-diffraction dimensions is ensured by (1) an overlay of the turn-off laser with the fluorescence excitation (or turn-on) laser, and (2) an intensity of the turn-off laser above the mentioned threshold.
A unique feature of this principle is that the size of the effective observation area / volume and thus the spatial resolution of the microscope is tuned by the intensity of the turn-off laser. More specifically, it has been shown that, for example, the lateral resolution is given by the diameter (or FWHM) of the observation area:

$$d \approx \lambda / \left(\mathrm{NA} \sqrt{1 + I/I_{\mathrm{sat}}} \right) \tag{2.16}$$

which approximately scales with the inverse square-root of the intensity I of the turn-off laser light [35,36,41]. Here, I_{sat} is the above-mentioned threshold intensity (often denoted as saturation intensity), which is a characteristic of the fluorophore (involving the light absorption cross-section of the ON-OFF transition and the lifetime of the involved states) and of the steepness of the edges of the intensity zeros. Driving the intensity I further up creates continuously smaller observation areas down to the size of a single molecule.
In practice, the wavefront of the turn-off laser is modified by the insertion of a phase plate or a grating in such a way that the focusing creates one or multiple intensity zeros. In the case of the single-point scanning microscope usually a doughnut-like intensity distribution with a central intensity zero is preferred [42, 43] which improves the spatial resolution along the lateral direction. Scanning of the marked reduced-size observation spot then renders a direct image of the distribution of fluorescently marked molecules with nanoscale spatial resolution (Figure 2.3a). However, as will be discussed later on, other intensity distributions have been realized as well, for example confining the fluorescence along the axial z-direction [33, 44, 45] or even along all spatial directions, creating an almost isotropic spot [5,46–48]. In case of the wide-field microscope, usually a standing-wave-like pattern with multiple zero-intensity lines such as in SIM is created. The camera images recorded for multiple scanning positions of the zeros are then post-processed to reconstruct the final image [49–52]. As shown recently, a preferred mode is to scan multiple points or doughnuts instead of rotating entire lines [53]. In any case, for $I >> I_{\mathrm{sat}}$, alike features closer together than the diffraction-limited of about 200 nm are now distinguishable, since they are switched on and detected separately in time. For the wide-field approach, this requires neighboring intensity zeros to be separated by more than the diffraction-limit of about 200 nm.
It is obvious that an improved resolution comes along with a reduction of the scanning step size; the molecules that were 'off' initially have to be turned 'on' later, etc. Therefore, an accurate acquisition of nanoscale details requires an increasing number of scanning steps and consequently longer acquisition times. Nevertheless, this coordinate-targeted approach offers all features of a conventional microscope

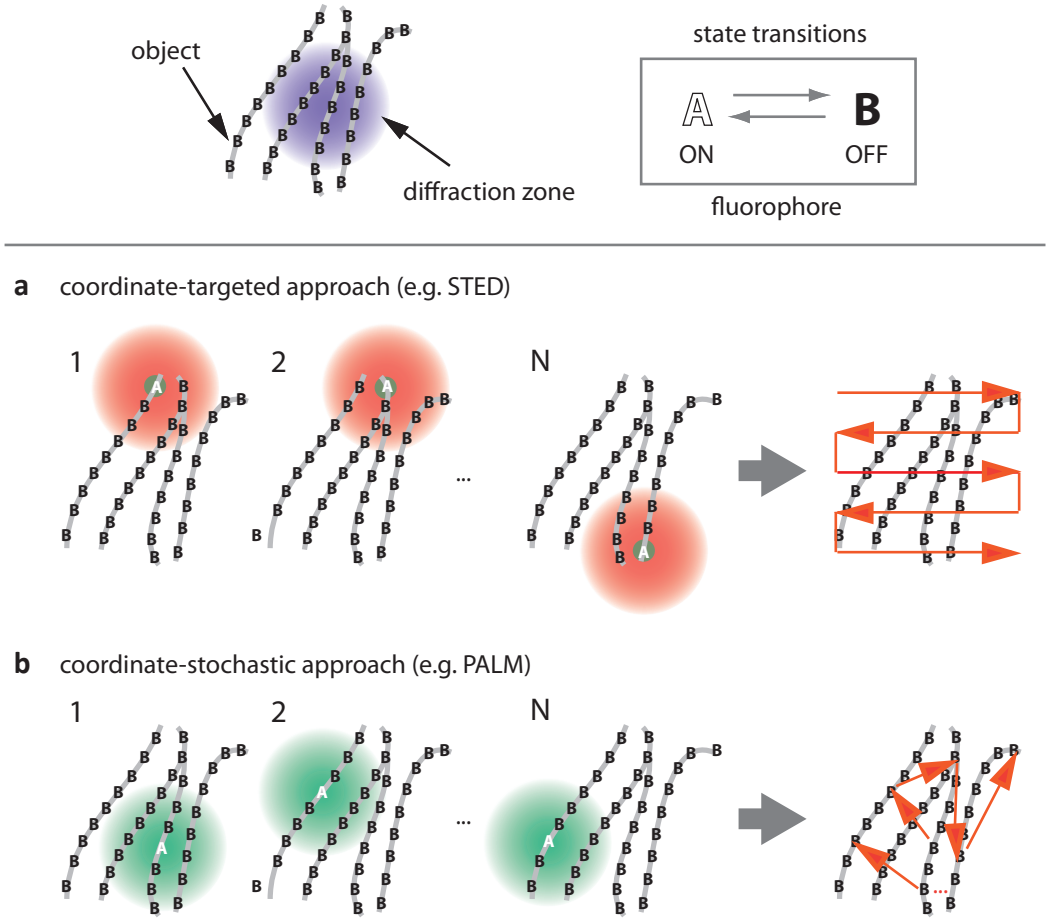

Figure 2.3: Targeted versus stochastic time-sequential read-out of fluorophores of a nanostructured object within the diffraction zone. A and B denote a bright and a dark state, respectively. (a) In the targeted read-out mode, one of the two states (here A) is established at a subdiffraction-size spot at the position of a zero to read-out an unknown number of fluorophores. The image is assembled by deliberate translation of the zero intensity. The zero can also be a groove. (b) In the stochastic read-out mode, a single switchable fluorophore from a random position within the diffraction zone is switched to a stable state A, while the other molecules remain in B. The coordinate is calculated from the centroid of the diffraction fluorescence spot measured by a pixelated detector. The coordinates appear stochastically depending on where the interrogated marker molecules are located.

from multicolor and 3D image acquisition over single-molecule detection to deep-tissue or in-vivo imaging.

STED

In STED nanoscopy, the pair of molecular states are the fluorophore's ground (dark OFF) state S_0 and the excited (fluorescent ON) state S_1, respectively. Being initially in the S_0 OFF-state, excitation to the S_1 ON-state and thus fluorescence emission is driven by the excitation laser, while switching back to the S_0 is realized by stimulated emission using a second laser, the STED laser. Above a certain threshold intensity the STED light causes stimulated S_1 to S_0 de-excitation to outperform spontaneous emission, i.e. the detected (spontaneous) emission is inhibited. The threshold or saturation intensity $I_{\mathrm{sat}} \propto (\tau\sigma_{\mathrm{STED}})^{-1}$ of the STED light is defined by the photon cross-section σ_{STED} of stimulated emission at the wavelength λ_{STED} of the STED laser and the lifetime τ of the unperturbed excited S_1 state. With lifetimes in the range of $1-4$ ns and stimulated emission cross-sections in the range of 10^{-17} cm^2 (i.e. photon cross-sections $\sigma_{\mathrm{STED}} \approx 25-30$ cm^2/J) STED intensities are usually $I_{\mathrm{sat}} >> 1-10$ MW/cm^2 have to be applied to realize a sufficient large fluorescence inhibition.

3D STED nanoscopy

So far STED nanoscopy which confines fluorescence emission and thus improves spatial resolution along the lateral direction has been highlighted only using the mentioned doughnut-like intensity distribution. The combination of this modality with evanescent wave illumination (TIRF) scheme for excitation [54,55] is sufficient for selectively imaging membranes of flat cells with penetration depths of < 100 nm, and the combination with two-photon excitation realized imaging in ~ 800 nm thick sections with deep penetration depths [56–61]. However, the imaging of intracellular structures such as the Golgi apparatus or mitochrondria often requires both a deeper penetration depth and an improvement of the spatial resolution along the axial z-direction as well. Four approaches have been applied so far: (1) The use of a phase plate that, upon interference, inhibits fluorescence along z and preferentially its combination with the doughnut-shaped plate creates the desired fluorescence restriction along all spatial directions [46,47,62,63]. (2) The use of the doughnut-shape STED focus in conjunction with illumination by two opposing objects (as a 4Pi) was used to create an effective isotropic observation volume with a spatial volume of down to 30 nm along all spatial directions [5,7,48]. Such an isoSTED microscope has given new insights into mitochrondrial structure, for example for the first time in resolving the mitrochindrial cristae with an optical microscope [9]. (3) Recently, a combination of STED with single plane illumination microscopy

(SPIM) realized an almost two-fold improvement in axial resolution along with a 1.3-fold improvement along the lateral directions compared to conventional SPIM. Applying this illumination scheme, STED-SPIM should allow penetration depths of > 100 μm and thus realize imaging inside zebra fish [64]. (4) Adaptive optics allows the correction of aberrations occurring predominately when imaging in 3D deep inside tissue [65, 66].

RESOLFT with RSFPs

But stimulated emission is only one way to reversibly transfer molecules between states of different fluorescence properties. Similarly, other state transitions may be applied for sub-diffraction optical microscopy (nanoscopy). The key is to identify a pair of ON- and OFF-states between which at least one transition can be driven by light [35, 36, 67]. The different mechanisms used so far significantly differ in the molecular states involved, the required intensity and the choice of label. Of interest are in particular molecular switches between states of very long lifetimes. The advantage is obvious: the utilization of states with very long lifetimes τ (or even the elimination of spontaneous transitions) would allow applying very low laser intensities for driving a fluorophore to a certain state. Reversible photoswitching between states with very long τ can be realized through changes in molecular conformation. A prominent example is photoinduced cis-trans isomerization involving fluorescent and dark (or non-detectable) isomeric counterparts, which can be switched back and forth by light of different wavelengths. In reversible switchable fluorescent proteins (RSFPs) the differently isomerized states are usually stabilized by the protein barrel surrounding the chromophore (and often involve differently protonated states) [68–71]. It was therefore an RSFP, asFP595, that was first used to experimentally prove the viability of the general RESOLFT concept [37]. Deliberate screening for fast and high-contrast monomeric RSFPs which should hardly show spontaneous decay of the involved states and, most importantly, survive 1000 and more photoswitching cycles was performed [72]. This screening ended in an RSFP variant of GFP (rsGFP: reversible switchable GFP), and its use in RESOLFT nanoscopy realized down to 40 nm spatial resolution in live-cell imaging [73]. Similarly, the RSFPs Dreiklang was created and applied to RESOLFT imaging, where suitable wavelengths for on and off switching and fluorescence excitation were completely disentangled, minimizing any action cross-talk [74]. Applying laser intensities of only 1 kW/cm^2, the RESOLFT concept applying RSFPs is highly suited for live-cell applications. Further improvements have come with the development of RSFPs with faster photoswitching times and decreased switching fatigue [75], as well as with additional emission wavelength ranges [76] for multi-color observations. Phototoxic effects of the (often UV) photoswitching light may be avoided by the use of IR light in a two-photon mode [77].

2.2.2 The coordinated-stochastic nanoscopy

The challenges posed by repeated cycling between molecular states for the coordinate-targeted STED/RESOLFT approaches are alleviated when transferring individual molecules between different states stochastically in space (Figure 2.3b). For example, molecules that are initially OFF may be individually driven to their ON-state at unknown spatial coordinates. The molecules' coordinates can be determined with sub-diffraction precision from their images on a camera. While the image of a single molecule is again blurred by diffraction, the molecular position can be determined by calculating the centroid of the blurred image spot. Restrictions are: (1) only single isolated molecules further apart than the distance given by diffraction can be imaged at a time to avoid any bias in localization of molecular positions from overlapping (blurred) spots, and (2) molecules, once in their ON-state, have to emit a sufficient number of photons N, since the localization precision scales with the inverse square root of N. It is however important to realize that localization *per se* cannot provide super-resolution, i.e. finding a position of an object with arbitrary precision is not the same as resolution. Resolution is about separating similar objects at small distances. This is why, although it had routinely been applied for decades, specifically for spatiotemporal tracking of single isolated particles or molecules, localization on its own did not provide nanoscale images. Resolution requires a criterion to discern neighboring molecules such as realized by driving molecular transitions between different states. Therefore, an approach first suggested as (F)PALM or STORM assembles a super-resolved image by determining spatial positions molecule by molecule using molecular transitions: (1) only a few isolated molecules are stochastically transferred (or activated) into their ON-state at once; (2) these molecules are imaged onto a camera and their spatial coordinates are determined through localization and saved; (3) molecules are transferred into an OFF-state; (4) stochastic activation of another subset of isolated molecules allows the read-out of neighboring molecules; and (5) repetition of this cycle realizes the reconstruction of an image with sub-diffraction resolution from the spatial coordinates of all images molecules (Figure 2.3b). The setup for this stochastic-switching based nanoscopy concept is a simple expansion of a conventional camera-equipped wide-field or TIRF microscope, updated by a stronger excitation laser and / or a second laser for controlling the switching of the molecules.

3D (F)PALM / STORM nanoscopy

Sectioning or 3D imaging has been implemented for coordinate-stochastic switching-based nanoscopy. Sectioning along the axial direction is provided when activating molecules via two- or multi-photon processes [78–80]. On the other hand, most

(F)PALM / STORM-based experiments have applied a TIRF illumination scheme from the very start, i.e. only planes of the sample that are within < 100 nm near the microscope cover glass are selected and the out-of-plane background is rejected. Several different approaches have been proposed and demonstrated to supply real 3D resolution (whether in wide-field or TIRF illumination mode), such as the introduction of astigmatism by the use of cylindrical lenses [80–82] or adaptive optics [83], double-plane detection using two camera channels [82, 84], two opposing objectives in a 4Pi illumination and detection mode [6, 85], a double-helix modification to the emission path of the microscope [86–89], bisected pupil 3D imaging [90], an Airy-beam PSF [91], other novel information-optimal point spread function designs [92] or a combination of two opposing objectives and astigmatism [93]. A nice example of 3D STORM nanoscopy recently presented novel details of the spatial organization of actin and other cytoskeletal filaments in mammalian cells [93] and axons [94]. Observing single-molecule fluorescence from deep inside samples such as tissue may prove itself difficult due to enhanced background signal stemming from scattered light or out-of-focus fluorescence. A remedy of this limitation may be the combination of the (F)PALM / STORM-based readout with selective-plane-illumination microscopy (SPIM) [95] and / or the use of adaptive optics to correct for aberrations [83].

2.2.3 Coordinate-targeted versus -stochastic nanoscopy

Both branches of nanoscopy – coordinated-targeted STED / RESOLFT and coordinate-stochastic (F)PALM – are ultimately based on the same basic principles: transferring fluorescent labels between states of different emission characteristics (such as a bright ON- and a dark OFF-state) that allow the discerning of nearby objects [67]. Both branches are complementary and have their own advantages and disadvantages. The advantage of stochastically switching is obvious: Whereas in the coordinate-targeted STED/RESOLFT read-out mode a molecule has to undergo many ON-OFF cycles, in the stochastic switching mode, a single OFF-ON-OFF cycle per molecule is in principle enough to produce an image, thus avoiding switching fatigue. However, in contrast to STED / RESOLFT nanoscopy, which usually creates a direct image of molecular distributions, computational algorithms are generally applied for (F)PALM / STORM to reconstruct the final image, a potential source of bias. For example, some molecules may be localized more precisely than others because the number of photon emission N follows a statistical distribution. Therefore, to ensure a certain resolution, the stochastic read-out mode usually defines a brightness threshold (e.g. N > 50) and molecules emitting less than this threshold in a bunch are discarded without contributing to the image. In a sense, this rejection of molecular events is to the stochastic read-out what switching fatigue (or photobleaching) is to its coordinate-targeted counterpart;

the higher the required resolution, the more molecular event are discarded. Often (F)PALM / STORM-based experiments have achieved focal plane resolution of <20 nm at the expense of discarding molecules [96,97]. In addition, some molecules may not be activated at all or counted several times, i.e. the molecular number assigned to the final image may be biased. While this imperfect assignment may not corrupt images of filament-like structures such as of microtubules, actin, mitochrondrial or ER membrane renditions, it may compromise the accurate characterization of protein clusters [98].

In general, coming along with the increased sensitivity of the nanoscopy approach, greater care has to be taken when labeling cellular samples, especially with respect to unspecific background staining [99]. Artifacts due to, for example, improper fixation in immunolabeling or unspecific binding may not be observed in confocal but may be visible in nanoscopy images, due to the improved spatial resolution in the latter [100, 101]. Also, due to the increased spatial resolution, the term 'co-localization' may become invalid since two objects (especially when labeled via a primary and secondary antibody as in most immunolabeling approaches) cannot occupy the same spot.

It is worth noting that the enhanced sensitivity of all nanoscopy concepts to artifacts calls for elaborate control measurements. For example, the results of previous protein cluster analyses using STED nanoscopy were ascertained using different labels as well as different STED setups, potentially introducing different switching fatigues [102]. At the same time, the multitude of different nanoscopy methods allow new ways of validating results. For example, both nanoscopy branches, the coordinate-targeted and the coordinate-stochastic, may exploit the same molecular transitions and may thus be applicable to the same samples. Consequently, both techniques could be applied for the validation of a specific result. Of course, while complementary, one approach may be more suitable for a concrete measurement than the other, and this argues for research environments having access to several of the above methodologies. For example STED / RESOLFT has proven to be able to record fast live-cell dynamics, even deep inside tissue and *in vivo*, yet to maintain reasonable signal-to-noise or -background levels, brightly labeled samples are often favored. On the other hand, (F)PALM / STORM-based experiments have shown remarkable results when imaging faintly labeled structures such as actin, but due to their acquisition mode have proven to be less versatile for dynamic live-cell and deep-tissue imaging, even if recent developments may improve their applicability in this regard.

2.3 Concepts of 4Pi-RESOLFT nanoscopy

In the combined use of 4Pi microscopy and RESOLFT nanoscopy in 4Pi-RESOLFT nanoscopy, the transitions of the negative-switching RSFP DronpaM159T [72,103, 104] were used. DronpaM159T stands out by relatively fast switching kinetics with comparatively low switching background. The peculiarity of negative-switching RSFPs is that they are switched off at a wavelength that is also used for generating the fluorescent signal. Hence their fluorescence signal is time-dependent. It decreases during the read-out.
The state cycle of DronpaM159T works as follows (Figure 2.4): Dronpa markers can be transferred from their inactive state (OFF, C) by one- (405 nm) or two-photon (780 nm) activation to their active state (OFF, B) (state transition: C → B). Then light with a wavelength around 491 nm can excite these fluorophores from their active state. While they cycle between the active (OFF, B) state and the excited (ON, A) state and emit fluorescence around 515 nm, a part will also be transferred to their inactive (OFF, C) state, i.e. while they are read-out by light of 491 nm, they are also switched off by it (B ↔ A → C). The cycle starts again with the activation of Dronpa.
In a 4Pi-RESOLFT nanoscope local DronpaM159T molecules are cycled at each scanning position through their ON- and OFF-states by consecutive light pulses with specific (4Pi) intensity patterns.

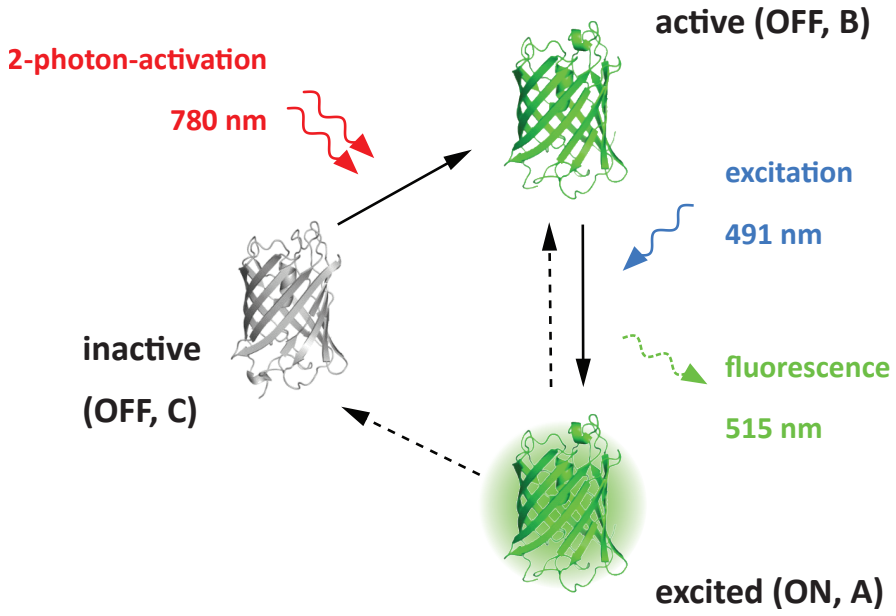

Figure 2.4: RSFP (Dronpa type) state cycle.

The implemented 4Pi-RESOLFT pulse sequence (per pixel) works as follows (Figure 2.5):

1. **activation:** An activation light pulse at 780 nm (activation pattern X) transfers local markers to their meta-stable 'active'-state by two-photon activation (state transition: C → B).

2. **deactivation:** The activated area is subsequently partially deactivated (off-switching) by a deactivation pulse at 491 nm (deactivation pattern Y), i.e. active RSFPs outside the targeted pixel volume (e.g. above and below the focal plane) are driven back to their inactive state which effectively denies them a further excitation to the fluorescent ON-state and thus improves the spatial ON/OFF-contrast during the following 'read-out' pulse (B ↔ A → C). Fluorescence generated during this process is discarded.

3. **read-out:** Finally, the remaining active markers are probed by a second pulse at 491 nm (read-out pattern Z) (B ↔ A → C). The fluorescence generated by the ON-state A is detected.

In 4Pi-RESOLFT nanoscopy the patterns X, Y and Z required in the different steps are created by the 4Pi arrangement (focal 4Pi patterns, Section 2.1.2) and/or by phase plates (the switching patterns for 3D nanoscopy in Section 3.1) depending on which final targeted pixel volume is desired.

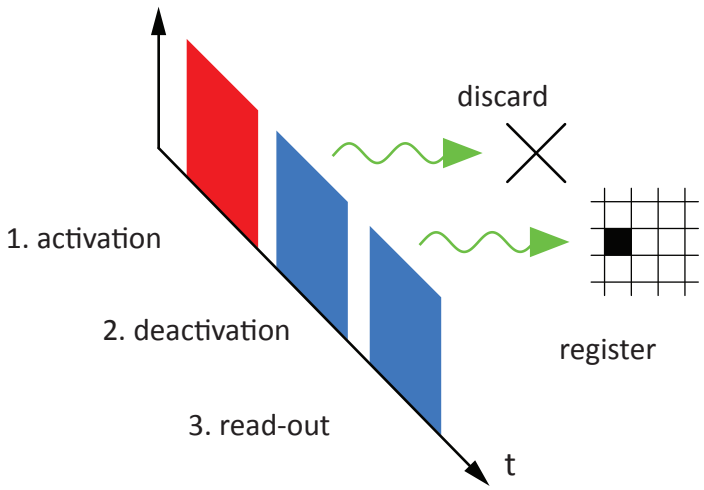

Figure 2.5: RESOLFT pulse sequence (per pixel).

In this thesis 4Pi interference patterns of 780 nm and 490 nm were used for the activation $h_{\mathrm{4Pi,ac}}(\vec{r})$ (pattern X) and the read-out $h_{\mathrm{4Pi,ro}}(\vec{r})$ (pattern Z), respectively (Figure 2.6). The axial positions of the sidelobes of these pattern are different due to wavelength disparity. To create a sphere-like sub-diffraction effective PSF for 3D 4Pi-RESOLFT nanoscopy, the intensity pattern during the deactivation step $h_{\mathrm{deact}}(\vec{r})$ (pattern Y) of the pulse sequence must have zero intensity in the focal center and be surrounded by non-zero intensities in all directions (Figure 2.6). In Chapter 3 is described how such a hollow intensity distribution and other useful patterns for 3D nanoscopy are created. Its application and performance are later discussed in Chapter 5.

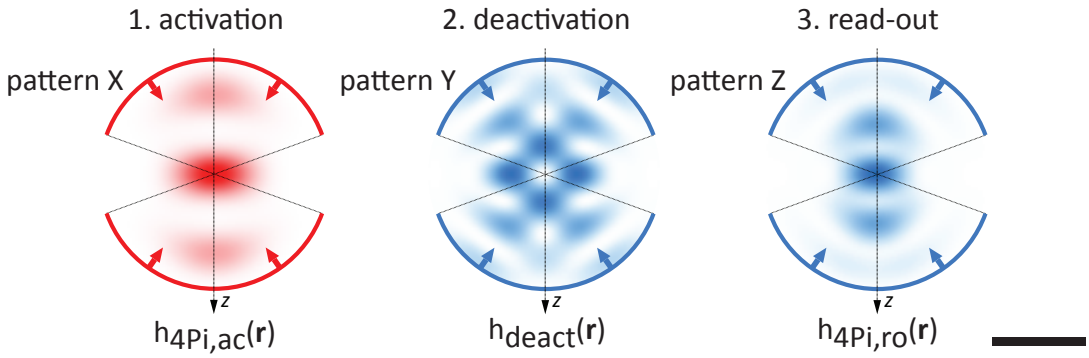

Figure 2.6: Focal patterns in 4Pi-RESOLFT nanoscopy. Scale bar: 500 nm

In general this 4Pi-RESOLFT scheme entails a number of advantages for live-cell 3D-imaging. First, RSFPs are inherently live-cell compatible protein markers, and selection of sufficiently bright and stable RSFPs is readily available [72, 73, 75]. Second, optical sectioning benefits from the additional switching step (activation) involved in the RSFP switching cycle with respect to modalities that do not make use of a meta-stable state like STED. This additional switching cycle becomes especially powerful if it is mediated by 2-photon absorption in a 4Pi configuration, as the 4Pi activation and 4Pi read-out pattern can be set up to a limited zone of overlap in the focal region. While overlapping several pattern also forms the basis of 4Pi microscopy of type-C using 2-photon excitation [28] (Section 2.1.2), here we do not require coherent double-lens (4Pi) detection of the emitted fluorescence. The scheme presented here thus acts to the same effect with less technical complexity. This aspect is discussed in detail in Chapter 4. Finally, activation by 2-photon absorption entails much less photo damage than 2-photon excitation, as it takes place at a time during the switching cycle when virtually no markers can assume their excited fluorescent state.

Optical sectioning – a general formalism for coordinate-targeted super-resolution imaging modalities

To understand the strong optical sectioning capability of 4Pi-RESOLFT nanoscopy better, we now define an expression for the effective point spread function (PSF) $h_{\mathrm{ef}}(\vec{r})$ of coordinate-targeted superresolution imaging modalities. This expression quantifies the 3D-coordinate range where the fluorescent molecules are allowed to yield measurable signal.

If the fluorophores from a certain range are imaged onto a (confocal point) detector, $h_{\mathrm{ef}}(\vec{r})$ is given by the normalized distribution $S^{\mathrm{ON}}(\vec{r})$ showing where the molecule is allowed to be in the ON state at the time of read-out, multiplied by the detection probability distribution $h_{\mathrm{det}}(\vec{r})$ which describes the probability to detect emission of a molecule in the ON state at position $\vec{r}$:

$$h_{\mathrm{ef}}(\vec{r}) = S^{\mathrm{ON}}(\vec{r}) \cdot h_{\mathrm{det}}(\vec{r}) \tag{2.17}$$

$S^{\mathrm{ON}}(\vec{r})$ is proportional to a product of normalized terms $h^{\mathrm{on}}(\vec{r})$ and $\tilde{h}^{\mathrm{off}}(\vec{r})$ that describe the generation of the ON-state by the use of on- and off-switching processes, respectively:

- $h^{\mathrm{on}}(\vec{r})$ describes the spatial probability distribution to assume the ON-state in the absence of off-switching light. It can typically be written as a product of terms $h_i^{\mathrm{on}}(\vec{r})$ that each express the relative probability for absorption of a single photon that drives a transition to a (virtual) state, and therefore scales with the intensity of the light pattern used (e.g. $h_{\mathrm{ro}}^{on} \propto I_{\mathrm{ro}}^{on}$ for single-photon read-out with intensity I_{ro}^{on}; in case of two-photon read-out: $h_{\mathrm{2ph\text{-}ro}}^{on} = h_{\mathrm{ro}}^{on} \cdot h_{\mathrm{ro}}^{on}$)
- $\tilde{h}^{\mathrm{off}}(\vec{r})$ describes the effect of the off-switching light on a potential ON-state distribution. This suppression factor is given by [105]:

$$\tilde{h}^{\mathrm{off}}(\vec{r}) = e^{-\ln 2 \cdot \left[h_{\mathrm{off}}(\vec{r}) \cdot \frac{I_{off}}{I_{sat}} \right]} \tag{2.18}$$

  where I_{sat} is the effective saturation intensity which is defined as the intensity at which the probability of fluorescence emission is reduced by half (Section 2.2.1), $h_{\mathrm{off}}(\vec{r})$ is the pattern of the off-switching light and I_{off} is its intensity.

We formally set $h_{\mathrm{det}}(\vec{r})$ as the first on-switching term $h_1^{\mathrm{on}}(\vec{r}) \equiv h_{\mathrm{det}}(\vec{r})$ (because of its similar effect on $h_{\mathrm{ef}}(\vec{r})$) and obtain:

$$h_{\mathrm{ef}}(\vec{r}) = \left(\prod_{i=1}^{O^{on}} h_i^{\mathrm{on}}(\vec{r}) \right) \cdot \tilde{h}^{\mathrm{off}}(\vec{r}) \tag{2.19}$$

Here, the number of on-factors O^{on} denotes the on-(switching) order of $h_{\mathrm{ef}}(\vec{r})$, e.g. $O^{\mathrm{on}} = 2$ (excitation by single-photon absorption and confocal detection) for a typical confocal (STED) microscope. A collection of on-factors O^{on} for different types of microscopes is listed in Section A.7.

Optical sectioning can generally be improved

- by engineering $\tilde{h}^{\mathrm{off}}(\vec{r})$ such that molecules in out-of-focus areas are switched off more effectively, and/or
- by requiring the absorption of multiple photons for the occupation of the ON-state, which increases O^{on}. This can be realized directly
  - through 2-photon absorption [20, 60, 80, 106], and/or
  - by requiring the sequential occupation of multiple real states in order to reach the ON-state [29]. Such sequential state occupation is easily realized using the switching steps offered by RSFPs (that are central to the RSFP-based RESOLFT concept [4, 107]).

The implemented coordinate-targeted 4Pi-RESOLFT modality resorts to all processes mentioned above which speaks for a good optical sectioning capability. Its performance will become apparent in Chapter 4 and Chapter 5.

Chapter 3

4Pi-RESOLFT nanoscope

This chapter focuses on the materials used and the methods for the experimental realization of 4Pi-RESOLFT nanoscopy with reversible switchable fluorescent proteins (RSFPs).
First the implemented 'deactivation' (off-switching) phase patterns for 3D nanoscopy are introduced (3.1) and then the microscope design (3.2) and the data acquisition (3.3). Finally the special 4Pi sample mount for live-cell imaging (3.4) and the associated 4Pi unit operation (3.5) are explained in detail.

3.1 Switching patterns for 3D nanoscopy

The off-switching patterns that are used for point scanning nanoscopy are characterized by a local intensity minimum at the focal center and flanked by preferably steep gradients. This shape is usually generated by phase modulation of a large angle focused wavefront, e.g. by means of a phase mask at (or imaged to) the back pupil plane of the objective lens, and/or by control of the phase between the counter propagating wavefronts that form a 4Pi focus. The following patterns are of particular relevance to 3D nanoscopy:

- The '*z-doughnut*' [33] (Figure 3.1a) is generated by single-lens focusing of a top hat shaped wavefront which was the first switching pattern used for 3D switching since most of its intensity is concentrated in two lobes above and below the focal plane and the gradients close to the focal center are comparatively low. These properties make it ideally suitable for dedicated side-lobe suppression in a two-focus setup as described in this work (Figure 3.1a and 5.6).

- The '*3D-doughnut*' [5] (Figure 3.1b) results from 4Pi focusing of a circularly polarized beam that has been imprinted with an azimuthal phase ramp oriented in countersense to the rotation of the field vector. It represents a very narrow single-focus 3D configuration for ON-state confinement that becomes virtually isotropic at large focusing angles. The precise axial-to-lateral aspect ratio also depends on the distributions of orientation and mobility of the fluorophore dipoles, as lateral and axial confinement is mediated by orthogonal field components (h^{ax}, h^{lat}, Figure 3.1b). Secondary minima with down to zero intensity are present above and below the focal plane and result in areas of little to no side-lobe suppression.

Figure 3.1 *(facing page)*: Switching patterns for 3D nanoscopy. Total focal intensity (h, blue) and its decomposition into lateral (h^{lat}, red) and axial (h^{ax}, green) components of three fundamental single-focus switching patterns: (a) 'z-doughnut' ($h_{\mathrm{zd}}(\vec{r})$), axial component shown at four times actual strength), (b) '3D-doughnut' ($h_{\mathrm{3d}}(\vec{r})$) and (c) 'aberrated 3D-doughnut' ($h_{\mathrm{3d'}}(\vec{r})$), along their corresponding back pupil phase patterns (right column) and circular polarization states (direction of rotation as marked for an arbitrary field vector $\hat{E}$), normalized to half the peak intensity obtained from single-lens focusing with a flat phase pattern. Phase patterns of opposing lenses (b,c) exhibit mirror-symmetry. Radii relative to pupil radius (r), r_{zd} = 0.71·r, $r_{\mathrm{3d'}}$ = 0.84·r. Numerical aperture 1.20, refractive index 1.362, constant total power, 4Pi phase 0.0, scale bar 1 µm.

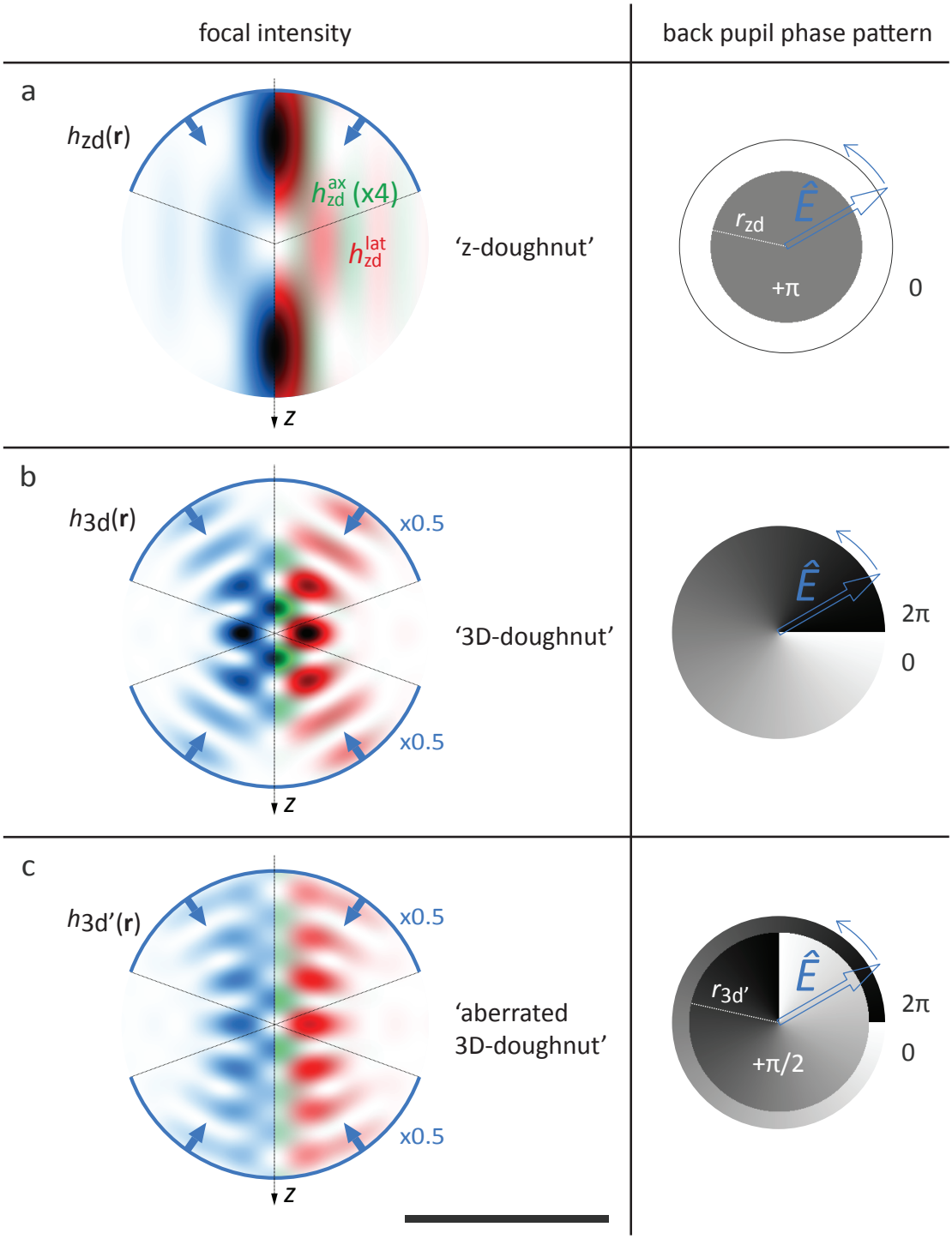
focal intensity
back pupil phase pattern
a
$h_{zd}(\mathbf{r})$
h_{zd}^{ax} (x4)
h_{zd}^{lat}
z
'z-doughnut'
r_{zd}
$\hat{E}$
+π
0
b
$h_{3d}(\mathbf{r})$
x0.5
x0.5
z
'3D-doughnut'
$\hat{E}$
2π
0
c
$h_{3d'}(\mathbf{r})$
x0.5
x0.5
z
'aberrated 3D-doughnut'
$r_{3d'}$
$\hat{E}$
+π/2
2π
0

- The '*aberrated 3D-doughnut*' (Figure 3.1c); a 3D-doughnut that has been modified by a further quarter-wave retardance added to each initial wavefront over a top hat profile, in order to create a single-focus 3D switching pattern with higher secondary minima (Figure 3.2) and thus improved suppression of on-axis lobes. With respect to a pure 3D-doughnut, light is diffracted outwards which flattens the gradients by a factor of 0.5. Just as in case of the z-doughnut, implementation of the modified phase mask involves a more elaborate alignment due to its dependence on the pupil diameter, which can be facilitated by the use of adaptable phase retarders (e.g. spatial light modulators [108, 109]). An aberrated 3D doughnut may also be obtained by moderrate defocussing of the deactivation beam to reduce the side minima [110].

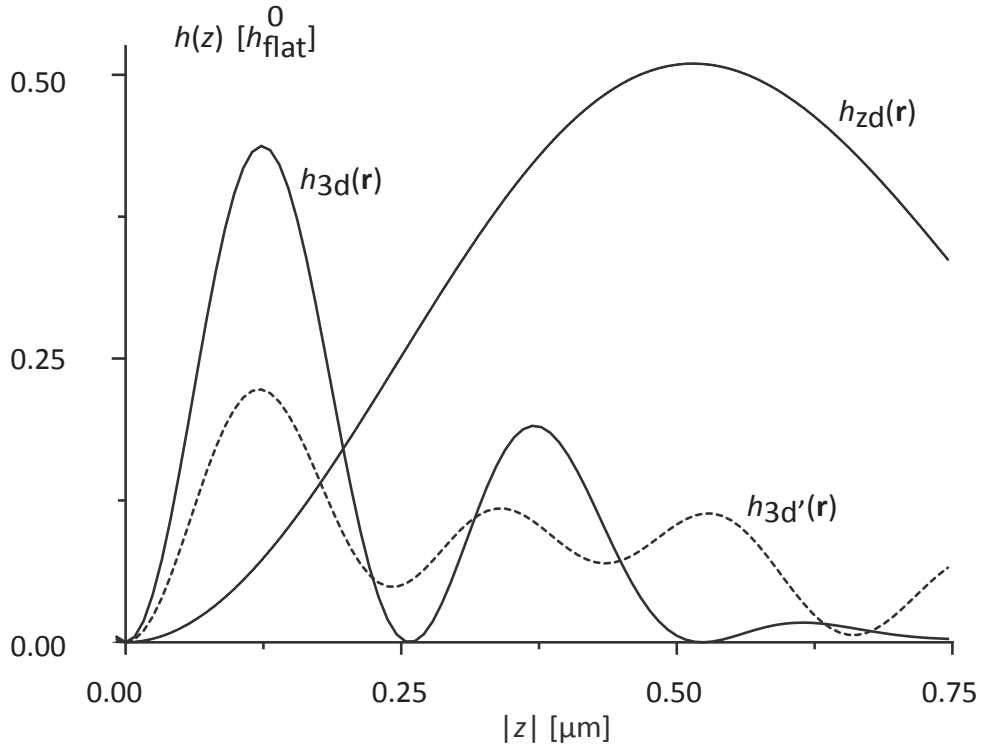

Figure 3.2: On-axis profiles of the '*z-doughnut*', '*3D-doughnut*' and '*aberrated 3D-doughnut*' pattern from Figure 3.1.

3.2 Main optical layout

The 4Pi-RESOLFT nanoscope is assembled as shown in Figure 3.3.
Light pulses (170 ps-pulses at 90 MHz) from a mode-locked Ti:Sapphire laser (Chameleon-XR, Coherent, Santa Clara, CA) are used for two-photon activation of RSFPs at 780 nm (4Pi activation pattern $h_{\mathrm{4Pi,ac}}(\vec{r})$). Telescopes are used to adjust the beam diameter and to defocus the beam in order to compensate an axial focus offset due to axial chromatic aberrations of the objectives. Before the beam is co-aligned with the beam path of the read-out and deactivation beams by a 5-mm-thick dichroic beam splitter (z740sprdc, Chroma), its polarization is adjusted with a half-wave plate to ensure that the beam is equally separated in the 4Pi arms of the 4Pi unit of the nanoscope. The active state of this beam is controlled by an acousto-optical light modulator.
Light for the read-out (4Pi read-out pattern $h_{\mathrm{4Pi,ro}}(\vec{r})$) and for the 3D deactivation ('3D-doughnut' $h_{\mathrm{3d}}(\vec{r})$, Figure 3.1b) at 491 nm (CW) emanates from a diode-pumped solid state laser (Cobolt Calypso, Cobolt, Vretenvägen, Sweden) which is spatially filtered by polarization maintaining single-mode fibers to remove aberrations in the beam to guarantee appropriate wavefronts. The final adjustment of the polarization and therefore the intensity of the beam in the 4Pi arms is done by a half-wave plate right before entering the 4Pi unit. To imprint the '3D-doughnut' deactivation pattern $h_{\mathrm{3d}}(\vec{r})$ onto the beam in the corresponding beam path, a vortex phase plate is used (VPP-1A, RPC Photonics, Rochester, NY). The beams are co-aligned with the beam path of the activation beam by a 5-mm-thick dichroic beam splitter (zt491rdcxt, Chroma). The active states of these beams are controlled by a combination of one acousto-optic tunable filter and electro-optical light modulators.
A further diode laser (Cobolt MLD, 488 nm, Cobolt, Vretenvägen, Sweden) provides a 488 nm beam (CW) for the auxiliary deactivation of side-maxima ('z-doughnut' $h_{\mathrm{zd}}(\vec{r})$, Figure 3.1a). Since its 'z-doughnut' pattern is only generated by single-lens focusing (section 3.1), it is necessary to adjust the polarization such that the beam only enters one arm of the 4Pi unit. To imprint the 'z-doughnut' deactivation pattern $h_{\mathrm{zd}}(\vec{r})$ onto the beam, a top hat phase plate (MgF_2 deposited onto fused silica, custom built in our optics workshop) is used.
The vortex phase plate and the top hat phase plate are imaged to the back pupil plane (BPP) of each objective lens (1.20 NA HCX PL APO, 63x, Leica Microsystems, Wetzlar, Germany) in order to generate the desired focal light patterns (Figure 3.1). Faraday isolators (FI) are integrated into the beam paths to prevent unwanted feedback of the reflected beams into the laser cavities. Furthermore, the power of all beams can be separately adjusted by a combination of a polarizing beam splitter and a half-wave plate. Scanning of the sample was implemented by a

galvanometric beam scanner (Yanus IV, TILL Photonics, Gräelfing, Germany), located at a conjugated plane with respect to both BBPs, and a piezo driven sample stage (P-541.ZCD, Physik Instrumente, Karlsruhe, Germany) with added optical stabilization.
To finally create the circular polarized light which is required for the formation of the '3D-doughnut' pattern at the foci of both lenses (Section 3.1), a combination of a polarizing beam splitter and a quarter-wave plate is placed directly in front of each objective lens.

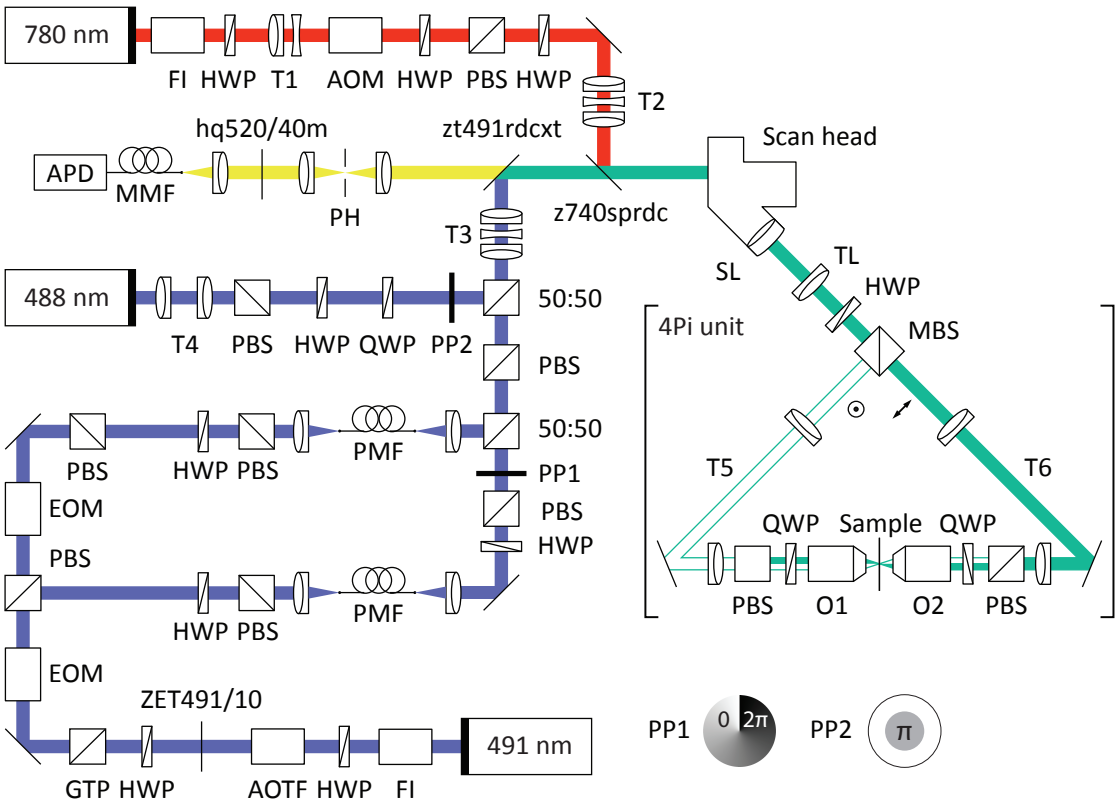

Figure 3.3: Optical layout of the 4Pi-RESOLFT nanoscope. AOTF, AOM: acousto-optic modulator; EOM: electro-optic modulator; FI: Faraday isolator; HWP: half-wave plate; QWP: quarter-wave plate; GTP: Glan-Thompson polarizer; PBS: polarizing beam splitter; 50:50: non-polarizing beam splitter; MBS: 4Pi main beam splitter (polarizing); T1-6: telescopes; PH: pinhole; APD: avalanche photodiode; PMF: polarization-maintaining fiber; MMF: multi-mode fiber; SL: scan lens; TL: tube lens; O1-2: objective lens; PP1: vortex phase plate; PP2: top hat phase plate

The fluorescence emerging from the sample is collected by both objective lenses, descanned, and directed towards a confocal pinhole (PH), after which the fluorescence is detected with an avalanche photodiode (APD, SPCM-AQRH-13, Excelitas Technologies Corp., Waltham, MA, USA). A bandpass filter (hq520/40m, Chroma) in front of the detector suppress the residual laser light.

3.3 Data acquisition

Data acquisition was controlled by a Python-scripted Imspector framework (Imspector, MPIbpc, Göttingen, Germany) running on a personal computer. Physical connection to downstream hardware (e.g. trigger logic, scanner, 4Pi slow control) and the detector (avalanche photo diode, SPCM-AQR-13-FC, PerkinElmer, Salem, MA) was provided by two I/O-modules (PCI-6259, National Instruments, Austin, Texas, USA) and a USB interface. Pulse sequences and duration for the RESOLFT imaging were shaped by acousto- and electro-optical light modulators (Figure 3.3) connected to a pulse generator (Model 9518, Quantum Composer, Bozeman, MT, USA).

3.4 4Pi sample mount for live-cell imaging

In a 4Pi arrangement, the refractive index (RI, n) difference between the material of the living mammalian cell ($n \approx 1.35 - 1.40$) [111] under observation and the surrounding culture medium (typically $n \approx 1.33$) is a major source of optical aberrations [112]. The aberrations generally reduce the attainable signal-to-noise ratio (S/N) by blurring the light intensity distributions in the focal region and by raising the intensity of the central minimum of the off-switching light pattern (Figure 3.1) [113–115]. A mounting procedure was therefore devised that minimizes optical aberrations by increasing the RI of a standard cell culture medium to $n = 1.362$ (section A.3) and by designing the optical setup accordingly (Figure 3.4): The 4Pi foci are jointly created by two 1.20 NA water immersion objectives that are outfitted with individual tip-/tilt-correction to prevent aberrations that arise from lens-coverslip misalignment [116]. The refractive indices of the embedding ($n = 1.362$) and immersion media ($n = 1.35$), the correction collar setting, and the cover slip thickness were chosen to minimize spherical aberrations [117] over at least 10 µm of the sample depth. The changes in the optical path lengths of the two 4Pi-interferometer arms due to z-scanning of the sample were compensated [118] by synchronous position adjustment of the main beam splitter cube (MBS, Figure 3.3).

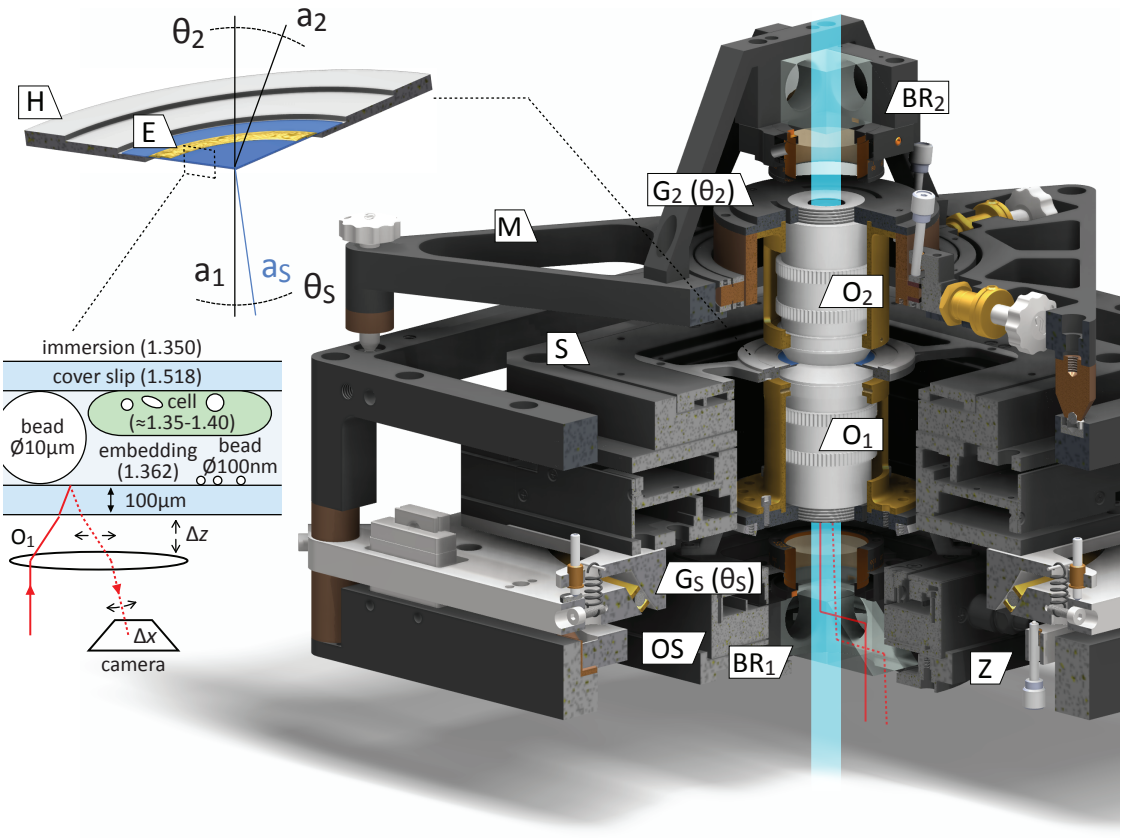

Figure 3.4: The upright 4Pi unit of the microscope and the 4Pi sample mount. Cells are mounted on a ring shaped sample holder (H), between two cover glasses fixed at 10 µm separation distance by spacer beads and epoxy resin (E). The set of refractive indices of the immersion and embedding medium, cover slip thickness and correction collar settings of the objective lenses (O_1, O_2) diminish aberrations from the sample. The sample stage (S) is mounted on a vertically movable (Z) goniometer (G_s) which accepts the sample holder (H) and provides five degrees of freedom for coarse xyz-positioning and z-scanning of the sample, as well as tip-/tilt-alignment (θ_s) of the cover slip normal (a_s) to the optic axis of $O_1(a_1)$. The objective O_1 itself is mounted on an xyz-piezo stage (OS) that provides online fine control over the displacement of both foci. A triangular mount (M) with goniometer (G_2) allows tip-/tilt(θ_2) and coarse xyz-alignment of O_2 (axis a_2) with respect to O_1, and can conveniently be detached in order to change the sample. Two polarizing beam splitter/quarter-wave retarder pairs ($BR_{1,2}$) clean up and tune the polarization of the incident beam pairs to opposing circular states. One beam of the splitters further serves as a port for an alignment laser beam that provides optical feedback for online-stabilization of the axial sample position (Δz); the beam traverses the respective objective lens off-axis (solid red path), gets reflected at the embedding medium interface, and is imaged onto a camera (dotted red path).

3.5 4Pi unit operation

The construction of the 4Pi unit was geared to combine easy handling with minimal drift during measurements. Its geometry and material composition (Figure 3.4 and A.1) were chosen such that the thermal expansion of corresponding components cancel out at the focus position in order to minimize thermal drift. The rigidity of each objective lens was increased by a lens cage ($L_{1,2}$) (Figure A.1) that fixes the movable lens cap to its base.
Optical contact between each objective lens and the sample was established by a droplet of refractive index liquid (Series AAA, $n_D = 1.35$, Cargille Laboratories, Cedar Grove, NJ, USA). The individual PSFs of each objective lens as well as their joint 4Pi PSFs were deduced from images of fluorescent reference beads inside the sample. The initial alignment of the unit (Figure A.1) is adherent to standard procedures [119] and involves minimizing the PSF extent along the optical axis by means of the correction collar ($C_{1,2}$), straightening of the PSFs by collinearization of the objective lenses and sample axes (θ_2, θ_S), and coarse superposition of the fields of view (FOV) of both lenses ($\Delta X, Y, Z_{\mathrm{FOV}}$).
During routine operation, the upper objective mount (with objective O_2) was detached in order to change the sample, and subsequently reattached with about 2 µm accuracy, which lies well within the travel of the lower objective piezo stage ($30 \times 30 \times 10$ µm, P-733.3DD, Physik Instrumente, Karlsruhe, Germany) used for FOV fine control ($\Delta xyz_{\mathrm{FOV}}$). Sample orientation ($\theta_S$) and coarse axial position (Z_S) were realigned as necessary. Axial travel of the goniometer platform could be locked against the outer frame by four clamp screws (P) for improved long term stability (Figure A.1). An automated online (drift) correction for the 4Pi phase ($\Phi_{4\mathrm{Pi}}$) and diverging FOV was implemented as a Python script within the data acquisition framework. Scanning was periodically switched from the region of interest (ROI) to the location of predefined 100 nm reference beads in order to assess the current $\Phi_{4\mathrm{Pi}}$ and FOV mismatch. The corresponding corrections were then applied to the main 4Pi beam splitter (MBS, Figure 3.3) and $\Delta xyz_{\mathrm{FOV}}$, and scanning of the ROI finally resumed.
A notable feature of the optical layout of the 4Pi unit (Figure 3.3) is the suppression of the transmitted light; in a typical 4Pi arrangement, light that is focused on the sample is usually picked up and re-collimated by the opposing objective lens, and therefore directed towards the detector where it needs to be filtered out in order to prevent it from generating an image background. Here, due to the polarization state of the transmitted light, it is already attenuated by a factor of 10^{-1}-10^{-2} at the polarizing beam splitter adjacent to the respective objective lens (Figure 3.3, 4Pi unit, hollow and solid beam paths), which relaxes the requirements on further filters.

Chapter 4

4Pi microscopy with RSFPs

This chapter describes how the optical sectioning of live-cell 4Pi microscopy already strongly benefits from the 4Pi-RESOLFT scheme even without the implementation of a '3D-doughnut' deactivation pattern for super-resolved images.
The first section of this chapter explains the basic principle of the implemented 4Pi-RESOLFT approach (4.1). The first results in living cells are then shown (4.2) and finally the potential of this method is discussed (4.3).

4.1 Principles

4Pi microscopy is a powerful technique to increase the axial resolution of a far-field light microscope and therefore it optical sectioning performance. Unfortunately, the interference of the wavefronts of two opposing lenses which increases the resolution also creates sidelobes which appear like ghost images (Section 2.1.2). Although it is possible to remove these lobes mathematically to some extent, it is advantageous to remove them initially. For this, additional optical techniques for lobe suppression have to be implemented, among which the most effective are:

- Confocal detection: The fluorescence emitted from out-of-focus planes is detected less efficiently, thus suppressing the fluorescence detection from the sidelobes (Section 2.1.2).
- Two-photon excitation: The quadratic dependence of the excitation efficiency on the illumination intensity lowers the excitation sidelobe height relative to the central peak. Additionally, due to the longer wavelength of the near-infrared light used, the sidelobes are shifted away from the focal plane and are better suppressed by the confocal pinhole (Section 2.1.2).
- Combined interference of the excitation and the detection: The wavelength disparity leads to different axial positions of the excitation and the detection sidelobes. As a result, the fluorescence originating from the excitation sidelobes is weakened by incomplete detection. Using two-photon excitation [2, 23, 28] entails a pronounced and very useful wavelength disparity (Section 2.1.2).

The potential of these lobe-suppression techniques was already recognized in the early stages of 4Pi microscopy [2,23]. In fact, the use of two-photon excitation with confocal detection has been the method of choice ever since. The third technique is more difficult to realize. The optical setup must be designed so that not only the excitation light interferes at the sample (type-A 4Pi), but also the detection light interferes at the point of detection (type-C 4Pi) (Section 2.1.2). Due to the different dispersion in the glasses and in air, dispersion compensation is necessary to ensure the interference of the fluorescence signal at the detector by matching the optical path lengths in the 4Pi arms of the 4Pi unit for the emission spectrum of the marker. This is implemented by a pair of adjustable glass wedges in one of the interferometric arms. The mean thickness of the wedge pair is precompensated in the other arm by a glass window of the average thickness of the wedges. The effective dispersion can be tuned by displacing the wedges against each other.
The two-photon excitation type-C 4Pi microscopy mode combines all three mechanisms and thus features the lowest achievable sidelobes. This greatly simplifies the

image restoration process. It obtains an ~ 30 % better resolution than its type-A counterpart and side lobes below 10 % of the height of the central maximum [120]. The effective PSF of a two-photon read-out type-C 4Pi microscope (equation 2.19) is given by:

$$\begin{aligned} h_{\text{ef,4Pi-C,2ph-ro}}(\vec{r}) &= \prod_{i=1}^{O^{\text{on}}} h_i^{on}(\vec{r}) \\ &= h_{\text{4Pi,det}}(\vec{r}) \cdot h^2_{\text{4Pi,ro}}(\vec{r}) \\ &= |\vec{E}_{1,\text{det}}(\vec{r}) + \vec{E}_{2,\text{det}}(\vec{r})|^2 \cdot |\vec{E}_{1,\text{ro}}(\vec{r}) + \vec{E}_{2,\text{ro}}(\vec{r})|^4 \end{aligned} \tag{4.1}$$

In this chapter 4Pi microscopy with RSFPs and two-photon activation was implemented. It combines of the interferences of the activation and of the read-out of the RSFPs. This scheme is less technical complex than type-C 4Pi microscopy since a broad-band intra-cavity dispersion compensation is not required. Furthermore, the two-photon activation entails much less photodamage than the two-photon excitation, as it takes place during the switching cycle when virtually no markers can assume their excited fluorescent state [17]. The effective PSF of this approach (equation 2.19) is given by:

$$\begin{aligned} h_{\text{ef,4Pi-RSFP,2ph-ac}}(\vec{r}) &= \prod_{i=1}^{O^{\text{on}}} h_i^{on}(\vec{r}) \\ &= h_{\text{det}}(\vec{r}) \cdot h^2_{\text{4Pi,ac}}(\vec{r}) \cdot h_{\text{4Pi,ro}}(\vec{r}) \\ &= |\vec{E}_{\text{det}}(\vec{r})|^2 \cdot |\vec{E}_{1,\text{ac}}(\vec{r}) + \vec{E}_{2,\text{ac}}(\vec{r})|^4 \cdot \\ &\quad |\vec{E}_{1,\text{ro}}(\vec{r}) + \vec{E}_{2,\text{ro}}(\vec{r})|^2 \end{aligned} \tag{4.2}$$

Thus, although both approaches for high optical sectioning implement a combination of two interference patterns in the focal plane with pronounced wavelength disparities realized by two-photon read-out or activation, the realization of the second approach is much more straightforward and less invasive.
Under ideal conditions, the effective PSF in RSFP-based 4Pi microscopy is virtually free of axial lobes. In practice, optical aberrations may give rise to lobe amplitudes that are still relevant. To counteract these effects, dedicated lobe deactivation by $h_{\text{zd}}(\vec{r})$ ('*z-doughnut*' in Section 3.1) can be applied, in addition to the developed low-aberration [117], live-cell 4Pi optics (Figure 3.4 and Section (3.4)).

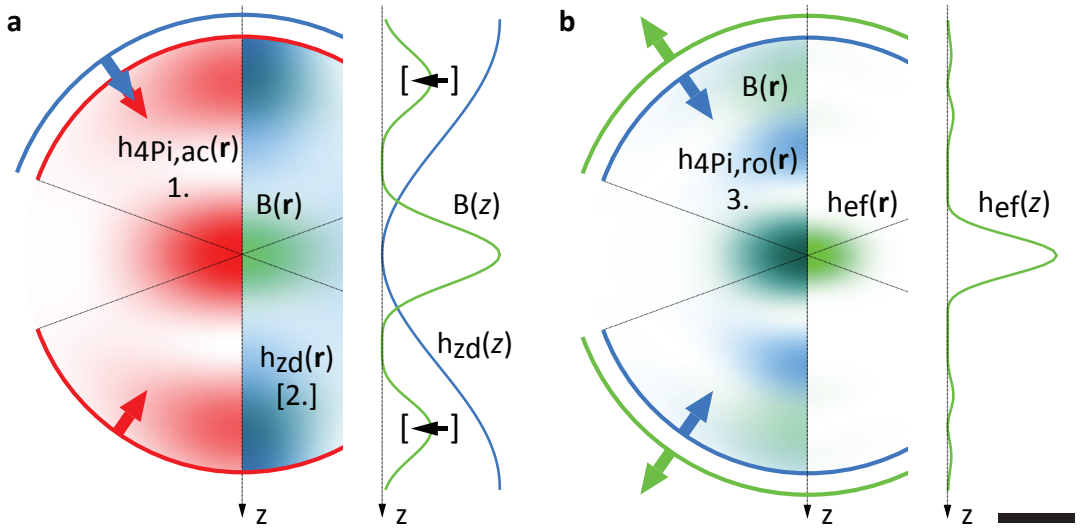

Figure 4.1: Principle of 4Pi microscopy with RSFPs. 4Pi activation pattern $h_{\mathrm{4Pi,ac}}(\vec{r})$) (a red), activated area $B(\vec{r})$ (= $h^2_{4Pi,ac}(\vec{r})$) (a green, b green (left)), deactivation pulse $h_{\mathrm{zd}}(\vec{r})$ (a blue), 4Pi read-out pattern $h_{\mathrm{4Pi,ro}}(\vec{r})$ (b blue), effective PSF $h_{\mathrm{ef}}(\vec{r})$ (b green (right)). Profiles show on-axis values. Scale bar: 200 nm.

In this case equation 4.2 has to be completed by the additional deactivation factor (see equation 2.18):

$$\tilde{h}^{\mathrm{off}}(\vec{r}) = e^{-\ln 2 \cdot \left[h_{\mathrm{zd}}(\vec{r}) \cdot \frac{I_{zd}}{I_{sat}}\right]} \tag{4.3}$$

The complete pulse scheme works now as follows: First the RSFPs are activated with an activation pulse (4Pi activation pattern $h_{\mathrm{4Pi,ac}}(\vec{r})$) for a few µs per pixel (Figure 4.1a, red) which induces two-photon activation of RSFPs in a pattern $B(\vec{r})$(= $h^2_{4Pi,ac}(\vec{r})$) (Figure 4.1a, green) with axial side-maxima (lobes). The lobes are optionally suppressed for a few µs per pixel by a subsequently applied deactivation pulse $h_{\mathrm{zd}}(\vec{r})$ (Figure 4.1a, blue and Figure 3.1a). The mutual overlap of the lobes of $B(\vec{z})$ and $h_{\mathrm{zd}}(\vec{z})$ is displayed in Figure 4.1a. Finally, the remaining activated RSFPs are read-out for a few µs per pixel by a 4Pi read-out patterns $h_{\mathrm{4Pi,ro}}(\vec{r})$ (Figure 4.1b, blue). Its mutual overlap with the activated area $B(\vec{r})$ (Figure 4.1b, green (left)) is constrained to the focal center, resulting in an effective PSF $h_{\mathrm{ef}}(\vec{r})$ (Figure 4.1b, green (right)) that exhibits ~ 100 nm axial FWHM, and exceptionally low side-maxima. The profile of the effective PSF is displayed in Figure 4.1b. Since $h_{\mathrm{ef}}(\vec{r})$ has almost negligible sidelobes, a deconvolution of the recorded images with this scheme is not necessary. The complete pulse scheme per pixel with the respective focal patterns is displayed in Figure 4.2.

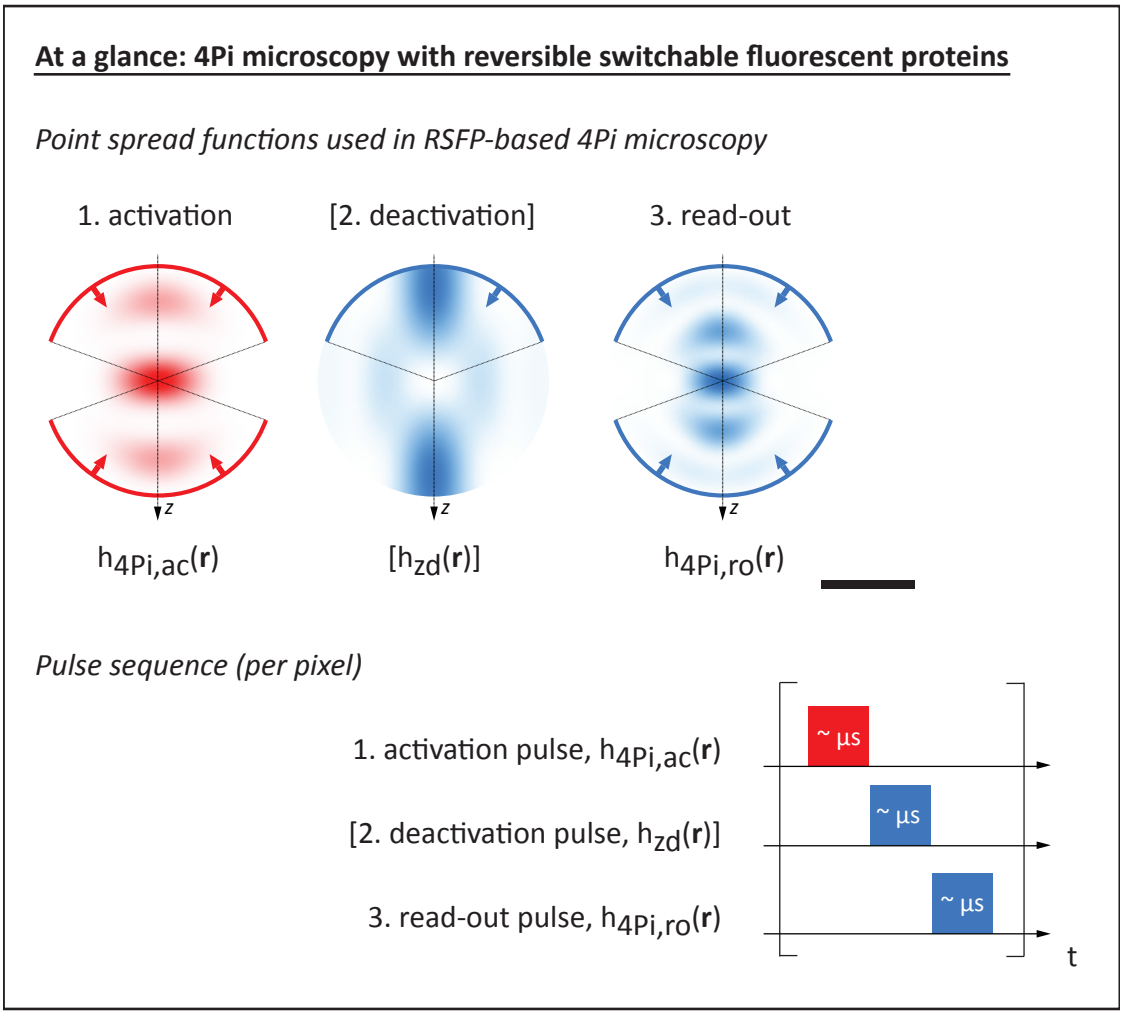

Figure 4.2: PSFs and pulse sequences for 4Pi microscopy based on RSFPs. 4Pi microscopy based on RSFPs offers the opportunity to shape the effective PSF with the combination of the interferences of the activation $h_{\mathrm{4Pi,ac}}(\vec{r})$ and of the read-out $h_{\mathrm{4Pi,ro}}(\vec{r})$. An additional deactivation pattern $h_{\mathrm{zd}}(\vec{r})$ can be used to suppress unwanted sidelobe amplitudes. Scale bar: 500 nm.

4.2 Results

To explore the imaging capability of 4Pi microscopy based on RSFPs, xz-sections of living CV-1 (*cercopithecus aethiops monkey kidney*) cells were recorded whose (a) lumen of mitochondria, (b) actin microfilaments and (c) intermediate filaments were labeled with the RSFP DronpaM159T. The cells were prepared according to the protocol in Section A.3, with the plasmids described in Section A.4.

Mitochondria are membrane bound organelles found in most eukaryotic cells, ranging in size from 0.5 to 1.0 µm in diameter and located in the cell's cytoplasm outside the nucleus. These structures are often dubbed "the powerhouse of the cell" because they generate most of the cell's supply of adenosine triphosphate which is used as the main source of chemical energy. Actin filaments and intermediate filaments are components of the cytoskeleton. They are widely distributed throughout the cell. An actin filament is flexible and ranges from 5-9 nm in diameter. Intermediate filaments are roughly 8 to 12 nm in diameter.

Figures 4.3 and 4.4 show xz-sections and volume renderings of living CV-1 cells. They were taken according to the following recording scheme: First the sample was activated by two-photon activation with the 4Pi activation pattern $h_{\mathrm{4Pi,ac}}(\vec{r})$ for 50 µs with 1.6 mW per pixel. Then the pattern $h_{\mathrm{zd}}(\vec{r})$ at 488 nm was used for 50 µs with 1.8 µW per pixel to suppress the sidelobes. Finally the sample was read out by the 4Pi read-out pattern $h_{\mathrm{4Pi,ro}}(\vec{r})$ at 491 nm for 50 µs with 3.1 µW per pixel. All used patterns are displayed in Figure 4.2.
The data shows that with 4Pi microscopy based on RSFPs, it is possible to record images with axial (z) resolutions in the range of 100 nm, axial lobes below 15 % of the main peak of the z-response, i.e. measured on laterally integrated data and no noticeable bleaching. These recordings did not need mathematical post-processing (i.e. deconvolution) dedicated to lobe-removal which is usually would be required for 4Pi-based methods.

Figure 4.3 *(facing page)*: 4Pi microscopy with RSFPs of living cells (xz-sections). 4Pi-RESOLFT raw data of DronpaM159T targeted to (a) lumen of mitochondria, (b) actin microfilaments, and (c) intermediate filaments of the cytoskeleton. The sample in (a) was subject to PFA fixation in order to freeze the motion of mitochondria; image in (b) and (c) were recorded from living cells. Estimates of the z-response (right), measured as box profiles over extended structures, exhibit only minor axial lobes in the range of 15 % of the main peak of the z-response. Pulse parameters; E_{ac}, E_{zd}, E_{ro} = 1.6 µW · 50 µs, 1.8 µW · 50 µs, 3.1 µW · 50 µs. Scale bars 1 µm.

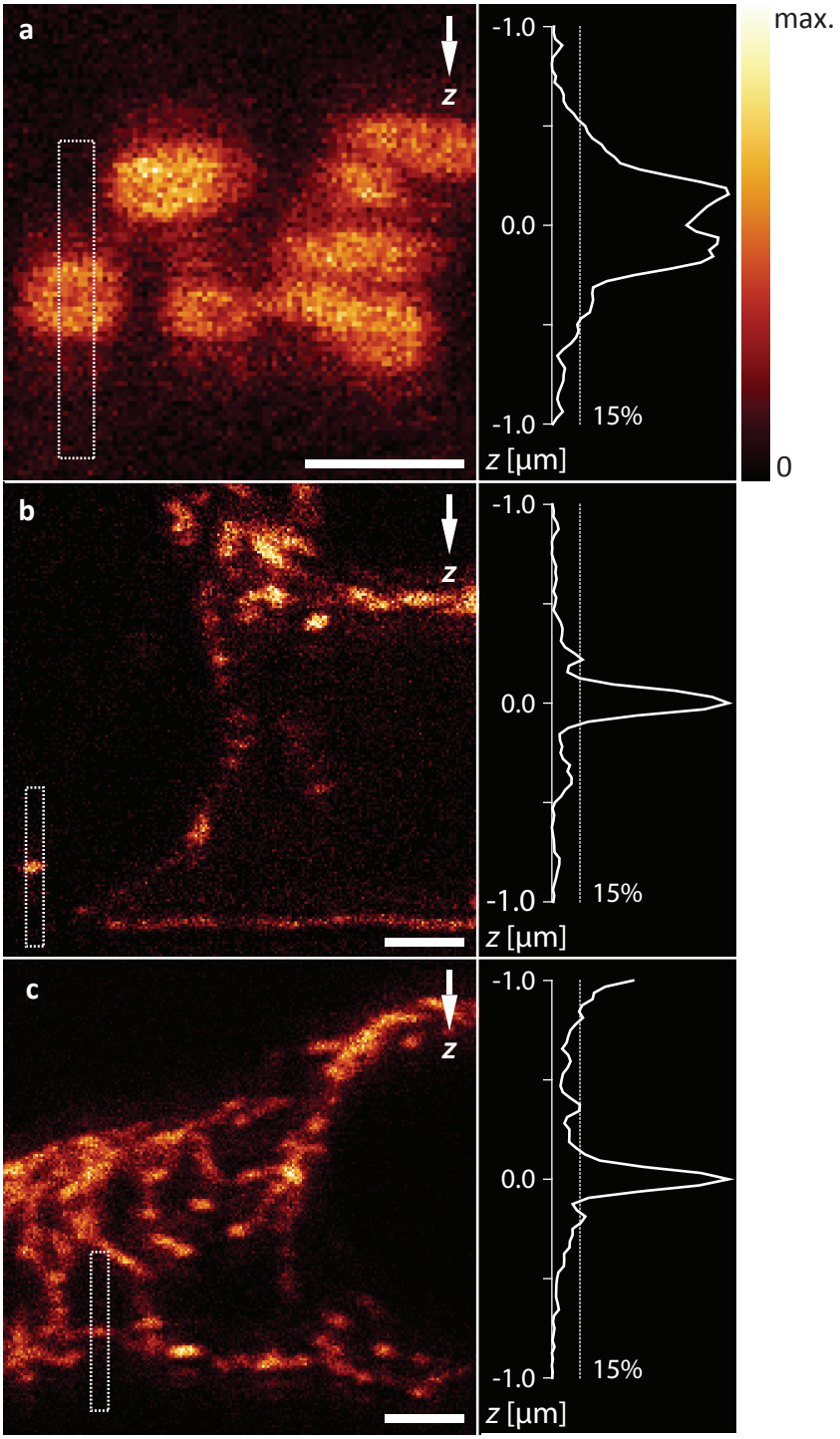
a
z
-1.0
0.0
-1.0
15%
z [µm]
max.
0
b
z
-1.0
0.0
-1.0
15%
z [µm]
c
z
-1.0
0.0
-1.0
15%
z [µm]

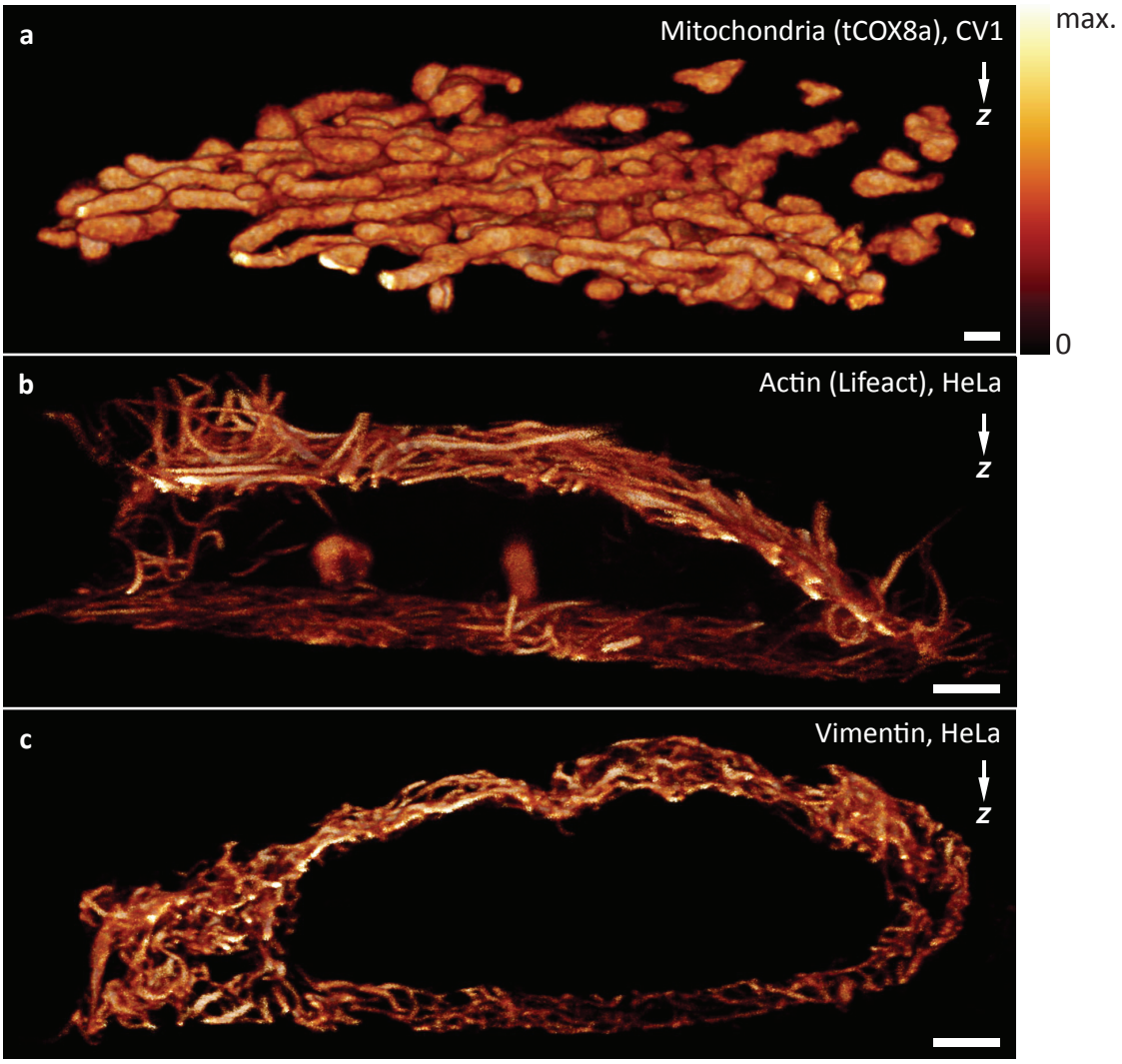

Figure 4.4: 4Pi microscopy with RSFPs of living cells (volume renderings). Volume surrounding the xz-sections of the images of Figure 4.3. Scale bars 1 µm.

Because the acquisition time of 11–16 s/µm^3 was short enough, subtly moving actin microfilaments at contact regions between adjacent living cells could be observed. For highly mobile organelles such as mitochondria (Figure 4.3a and Figure 4.4a), fixation of the sample by paraformaldehyde incubation (Section A.3) offered a means to prevent motion blur. While this treatment irreversibly arrests the cell, its potential to introduce structural artifacts is very low with respect to staining / embedding protocols that involve membrane permeabilization.

4.3 Discussion

For the first time, the improvement of optical sectioning in 4Pi microscopy was achieved by the use of sequential occupation of multiple real states in order to reach the ON-state [29] (Section 2.3). The sequential state occupation was realized using the switching steps offered by RSFPs.

The coherent superposition of the two-photon activation spherical wavefront pairs of two opposing lenses in conjunction with that of their read-out in this RSFP-based 4Pi microscopy approach (Figure 4.2) led to axial resolutions of ~ 100 nm in 3D imaging of aqueous samples with only minor axial lobes and no noticeable bleaching (Figure 4.3, Figure 4.4 and Section A.5).

Compared with other related imaging modes (e.g. type-A 4Pi microscopy), the reported 4Pi approach is more resilient to periodic artifacts induced by interference. This is due to the rather low interference sidelobes of the PSF (Figure 4.1b), which is equivalent to a contiguous and well-filled OTF. The quadratic intensity dependence and strong activation/read-out wavelength disparity brought about by two-photon activation considerably contributes to the improvement in optical performance. The system's performance is similar to that of a two-photon type-C 4Pi microscope, but with the advantage of being less technically complex, while operating at low light levels. Further, the two-photon activation entails much less photodamage than two-photon excitation in type-C 4Pi microscopy because it takes place during the switching cycle when virtually no markers can assume their excited fluorescent state.

Thus the use of sequential state occupation given by RSFPs is advantageous in 4Pi microscopy. Additional real states in order to reach the ON-state (combinations with dark states occupations etc.) might push the performance even further. The recording time could be decreased by parallelization of the system using a multi-spot scanning arrangement [121].

However, the spatial resolution of this approach is still limited, i.e. it does not break the diffraction barrier, but it rather pushes diffraction to its limits along the optical axis. To overcome this limit, an additional '3D-doughnut' deactivation pattern for 3D nanoscopy was implemented in Chapter 5 to achieve 3D-nanoscopic imaging in living cells.

Chapter 5

3D 4Pi-RESOLFT nanoscopy

This chapter describes the use of the built nanoscope for three-dimensional 4Pi-RESOLFT nanoscopy when implementing a '3D-doughnut' deactivation pattern for 3D nanoscopy. This scheme enables the image formation with super-resolved isotropic resolution in living cells at low light levels with strong optical sectioning. First the basic principles of this application are explained (5.1), followed by the description of a rate-gated read-out scheme to further improve the signal-to-noise ratio in the image and the resolution (5.2). The first results in living mammalian cells are then shown (5.3) and the potential of the method is discussed (5.4).

5.1 Principles

In order to visualize structures below the diffraction limit in 3D, several approaches have been put forward in far-field fluorescence microscopy (Section 2.2.1 and Section 2.2.2).
Methods based on sharpening of the PSF are especially attractive for imaging deep inside a cell. First, because they detect molecular ensembles and allow the tuning of the signal strength by varying the spot size, which is particularly important for nanoscale imaging inside living cells. Second, since they are ensemble methods, schemes relying on PSF sharpening can in conjunction with confocal detection effectively suppress the background which renders them single molecule-sensitive in the bulk. Directing the focal spot to an arbitrary coordinate in the sample allows direct probing of sites of interest in the cellular interior. However, to unfold its full potential the effective PSF must be spherical.
To create such a spherical PSF which would allow resolving smaller features with the 4Pi-RESOLFT nanoscope, a switching pattern for deactivation of the RSFPs around the focal center was implemented: A hollow '3D-doughnut' $h_{3d}(\vec{r})$ (Figures 3.1a) which features light intensity everywhere around a focal intensity zero. This pattern was created by a single focused 4Pi beam pair [48] and allowed to tune $h_{ef}(\vec{r})$ to a near-isotropic resolution below the diffraction limit (Figure 5.1).

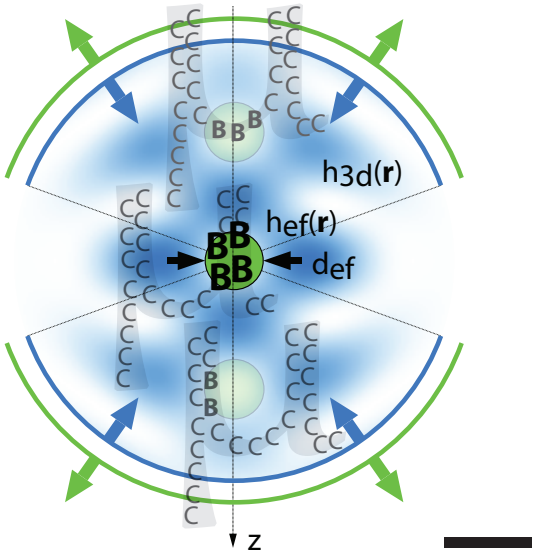

Figure 5.1: A hollow switching pattern $h_{3d}(\vec{r})$ (blue) confines the central effective PSF $h_{ef}(\vec{r})$ (green) to a spot with diameter d_{ef} by switching activated markers (B) back to their inactive state (C). μ, labeled structure. Scale bar: 200 nm.

A similar pattern had already been implemented in isoSTED [5], which combines opposing lenses (4Pi arrangement) with the switching of adjacent markers by stimulated emission depletion (STED). In isoSTED, a 3D hollow pattern $h_{\bar{3}\mathrm{d}}(\vec{r})$ generated by two focused 4Pi beam pairs is combined with a 4Pi read-out pattern $h_{\mathrm{4Pi,ro}}(\vec{r})$ to create a spherical spot that can be arbitrarily downscaled in size. The effective PSF of an isoSTED microscope (see equations 2.19 and 2.18) is given by:

$$\begin{aligned} h_{\mathrm{ef,isoSTED}}(\vec{r}) &= \left(\prod_{i=1}^{O^{\mathrm{on}}} h_i^{\mathrm{on}}(\vec{r})\right) \cdot \tilde{h}^{\mathrm{off}}(\vec{r}) \\ &= h_{\mathrm{det}}(\vec{r}) \cdot h_{\mathrm{4Pi,ro}}(\vec{r}) \cdot \tilde{h}^{\mathrm{off}}(\vec{r}) \\ &= |\vec{E}_{\mathrm{det}}(\vec{r})|^2 \cdot |\vec{E}_{1,\mathrm{ro}}(\vec{r}) + \vec{E}_{2,\mathrm{ro}}(\vec{r})|^2 \cdot e^{-\ln 2 \cdot \left[h_{\bar{3}\mathrm{d}}(\vec{r}) \cdot \frac{I_{\bar{3}d}}{I_{sat}}\right]} \end{aligned} \tag{5.1}$$

With isoSTED it was possible to create nearly spherical focal spots of 40-45 nm in diameter to visualize 3D nanostructures of polymers [10] and organelles in the interior of fixed cells [9] that had until then required electron microscopy.
When using the state transitions between different conformational states of RSFPs with two-photon activation and the hollow switching pattern $h_{3\mathrm{d}}(\vec{r})$ (Section 3.1) in the built 4Pi-RESOLFT nanoscope, the effective 4Pi-RESOLFT or iso-RESOLFT PSF (see equations 2.19 and 2.18) is given by:

$$\begin{aligned} h_{\mathrm{ef,isoRESOLFT}}(\vec{r}) &= \left(\prod_{i=1}^{O^{\mathrm{on}}} h_i^{\mathrm{on}}(\vec{r})\right) \cdot \tilde{h}^{\mathrm{off}}(\vec{r}) \\ &= h_{\mathrm{det}}(\vec{r}) \cdot h_{\mathrm{4Pi,ac}}^2(\vec{r}) \cdot h_{\mathrm{4Pi,ro}}(\vec{r}) \cdot \tilde{h}^{\mathrm{off}}(\vec{r}) \\ &= |\vec{E}_{\mathrm{det}}(\vec{r})|^2 \cdot |\vec{E}_{1,\mathrm{ac}}(\vec{r}) + \vec{E}_{2,\mathrm{ac}}(\vec{r})|^4 \cdot \\ &\quad |\vec{E}_{1,\mathrm{ro}}(\vec{r}) + \vec{E}_{2,\mathrm{ro}}(\vec{r})|^2 \cdot e^{-\ln 2 \cdot \left[h_{3\mathrm{d}}(\vec{r}) \cdot \frac{I_{3d}}{I_{sat}}\right]} \end{aligned} \tag{5.2}$$

When comparing equations (5.1) and (5.2), the advantages of a 4Pi-RESOLFT imaging approach become clearer: (1) The additional activation step increases the on-switching order O^{on} (Section 2.3), which improves the shape of the effective PSF $h_{\mathrm{ef}}(\vec{r})$ of the imaging system, (2) the use of two-photon increases the on-switching order O^{on} as well (Section 2.3) and introduces an additional wavelength disparity which impacts the effective PSF $h_{\mathrm{ef}}(\vec{r})$ (Section 4.1) and (3) the state transition which is used in RESOLFT with RSFPs requires less intensity, therefore the saturation intensity I_{sat} in $\tilde{h}^{\mathrm{off}}(\vec{r})$ is lower (Section 2.2.1), resulting in less intensity required to achieve super-resolved isotropic resolution.

The improved z-response $h_z(z)$ of the implemented 4Pi-RESOLFT scheme in comparison to isoSTED is shown in Figure 5.2a.
Furthermore, calculations using a vectorial diffraction theory [122] predicted on-axis modulation transfer function (MTF) values $H(k_z)(z)$ (Section 2.1) of over 40 % of the MTF maximum within the MTF bandwidth up to a resolution of 30 nm. This feature keeps the signal well over the noise level in most applications and exemplifies the improvement brought about by higher order on-switching (Section 2.3 and Section A.7) in comparison to modalities of 2^{nd}-order such as those reported in isoSTED microscopy [5] (Figure 5.2b).
Under ideal conditions, the effective PSF even without the deactivation pattern $h_{3\mathrm{d}}(\vec{r})$ should be virtually free of axial lobes (Chapter 4). In practice, this is not always the case and those remaining lobes due to ineffective switching at low off-center $h_{3\mathrm{d}}(\vec{r})$ amplitudes when applying the hollow deactivation pattern $h_{3\mathrm{d}}(\vec{r})$ for isotropic nanoscale resolution increase in relative strength as d_{ef} is reduced (Figure 5.1). In this case the use of the additional deactivation pattern $h_{\mathrm{zd}}(\vec{r})$ may also be recommended. If $h_{\mathrm{zd}}(\vec{r})$ is applied, equation 5.2 has to be completed by the additional deactivation factor:

$$\tilde{h}^{\mathrm{off}}(\vec{r}) = e^{-\ln 2 \cdot \left[h_{\mathrm{zd}}(\vec{r}) \cdot \frac{I_{zd}}{I_{sat}}\right]} \tag{5.3}$$

The complete pulse scheme per pixel with the respective focal patterns is displayed in Figure 5.3 and works as follows: First the RSFPs are activated with the two-photon 4Pi activation pattern $h_{\mathrm{4Pi,ac}}(\vec{r})$ for a few µs per pixel. Then the activated fluorescent proteins are deactivated by the hollow deactivation pattern $h_{3\mathrm{d}}(\vec{r})$ for a few ms per pixel and if required by the deactivation pattern $h_{\mathrm{zd}}(\vec{r})$ for a few µs per pixel. Finally the 4Pi read-out pattern $h_{\mathrm{4Pi,ro}}(\vec{r})$ collects the signal which has not been deactivated in its operating regions for a few ms per pixel.
During read-out in this 4Pi-RESOLFT scheme the fluorescence signal of DronpaM159T decreases with a distinct multi-exponential decay, hinting at the contribution of multiple deactivation rates. Thus, a 'rate-gated' RESOLFT detection scheme was introduced that could improve both the signal-to-noise ratio in the image and the resolution by discriminating individual signal components (Section 5.2 and Figure 5.4).

Figure 5.2 *(facing page)*: Simulated (a) z-response $h_{\mathrm{Z}}(z)$ and (b) axial MTF profile $H(k_{\mathrm{Z}})$ of the 4Pi-RESOLFT nanoscope (4^{th} on-order switching, solid lines) of a labeled xy-plane at different target resolutions d_{ef}. DL, diffraction limit. Graphs for an isoSTED microscope under similar conditions are included for resolution reference (2^{nd} on-order, dotted lines).

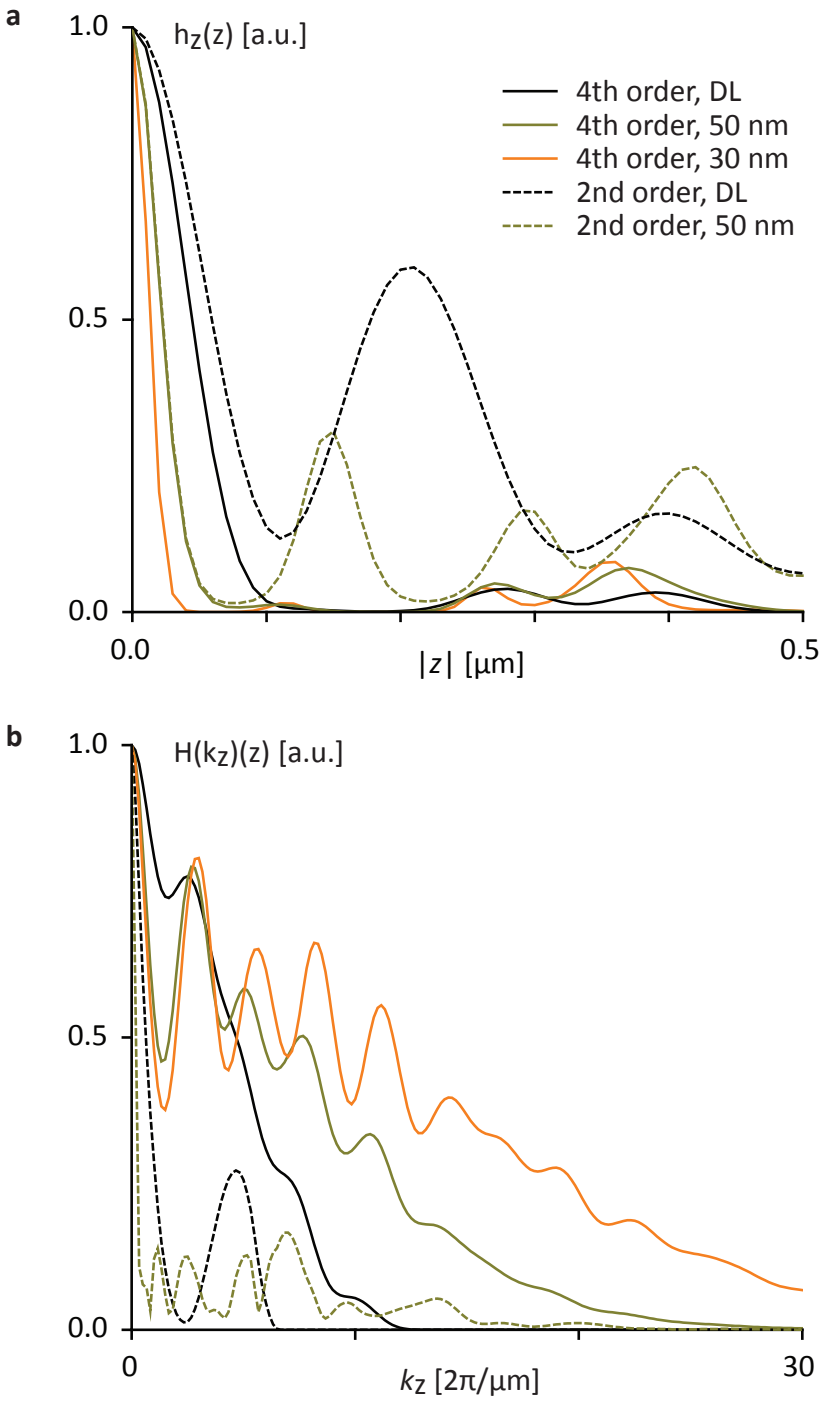
a
1.0
0.5
0.0
$h_z(z)$ [a.u.]
4th order, DL
4th order, 50 nm
4th order, 30 nm
2nd order, DL
2nd order, 50 nm
0.0
0.5
|z| [µm]
b
1.0
0.5
0.0
$H(k_z)(z)$ [a.u.]
0
30
k_z [2π/µm]

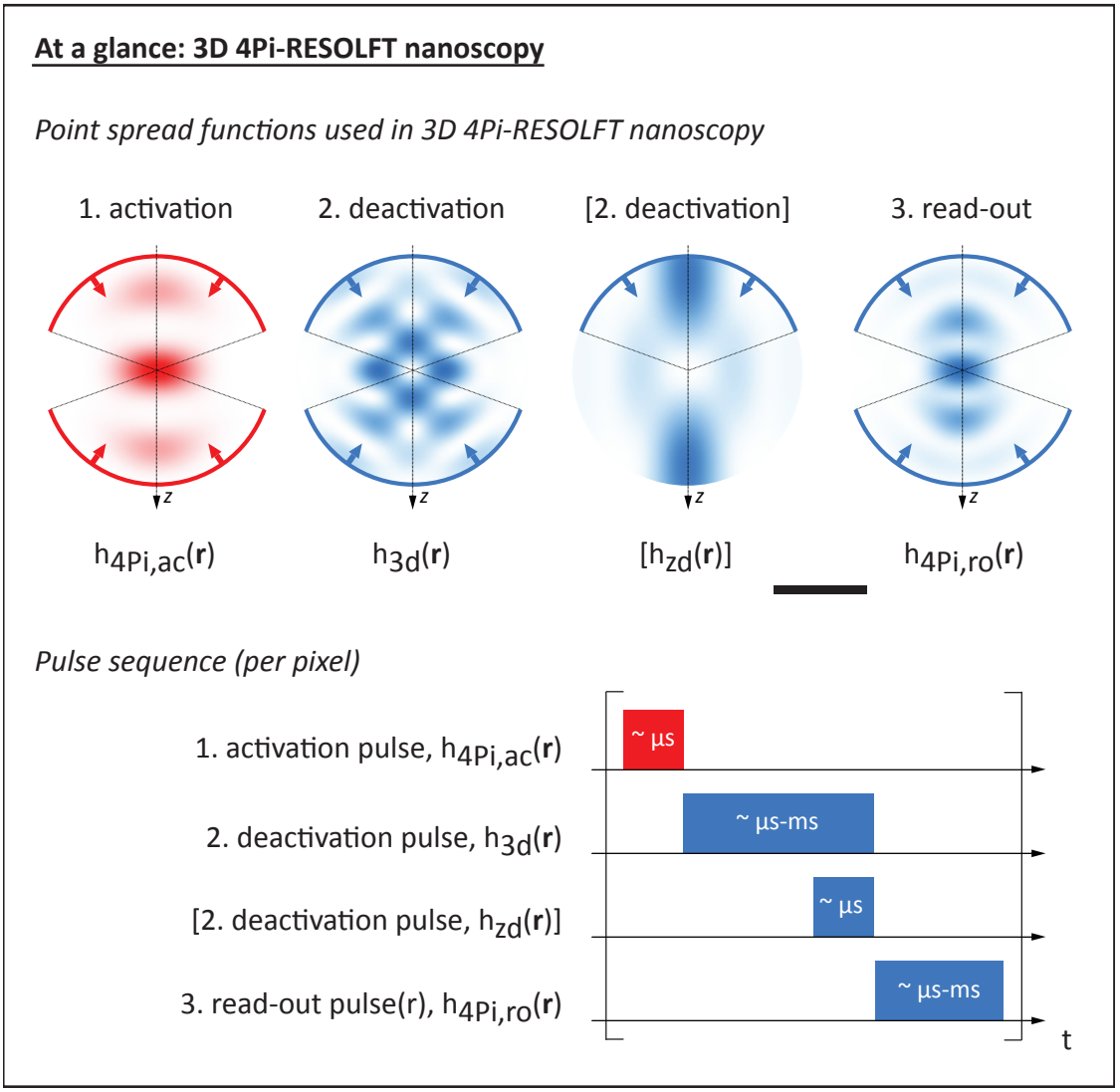

Figure 5.3: PSFs and pulse sequences used in 3D 4Pi-RESOLFT nanoscopy. 3D 4Pi-RESOLFT nanoscopy offers the opportunity to shape the effective PSF with the combination of the interference of the activation $h_{\mathrm{4Pi,ac}}(\vec{r})$ and the interference of the read-out $h_{\mathrm{4Pi,ro}}(\vec{r})$ and a 3D hollow switching pattern $h_{\mathrm{3d}}(\vec{r})$ to a sphere-like sub-diffraction spot. An additional deactivation pattern $h_{\mathrm{zd}}(\vec{r})$ can be used to suppress possible background signal even further. Scale bar: 500 nm.

5.2 Rate-gated detection in RESOLFT imaging

In the present case of RESOLFT imaging of negative switching RSFP, deactivation of fluorophores during read-out gives rise to a time-dependent signal and hence a time-dependent effective PSF $h_{\mathrm{ef}}(\vec{r},t)$ (Section 2.3). The time-resolved image $g(\vec{r},t)$ obtained by imaging a structure $s(\vec{r})$ is thus given by

$$g(\vec{r},t) = s(\vec{r}) \otimes h_{\mathrm{ef}}(\vec{r},t) \tag{5.4}$$

We simply assume a deactivation rate $\lambda(\vec{r})$ that only depends on the read-out intensity $I_{\mathrm{ro}}(\vec{r})$ and therefore obtain

$$h_{\mathrm{ef}}(\vec{r},t) = h_{\mathrm{ef}}(\vec{r}) \cdot e^{-\lambda(\vec{r})\cdot t} = h_{\mathrm{ef}} \cdot e^{-\lambda \cdot I_{ro}(\vec{r})\cdot t} \tag{5.5}$$

with t denoting time relative to the start of the read-out pulse. The deactivation pattern $h_{3\mathrm{d}}(\vec{r})$ typically confines the effective volume from which fluorescence is collected to a region of FWHM d_{ef} around the primary zero of the switch-off pattern. This region is much narrower than the FWHM d_{ro} of the diffraction pattern used for read-out:

$$d_{\mathrm{ef}} << d_{\mathrm{ro}} \tag{5.6}$$

The read-out intensity can then be considered constant, and $h_{\mathrm{ef}}(\vec{r},t)$ follows a mono-exponential decay at a rate that only depends on the peak read-out intensity $I^0_{\mathrm{ro}} := I_{\mathrm{ro}}(0)$. Thus, $g(\vec{r},t)$ becomes separable and transforms into:

$$g(\vec{r},t) = g(\vec{r}) \cdot g(t) := \left(s(\vec{r}) \otimes h_{\mathrm{ef}}(\vec{r})\right) \cdot e^{-\lambda \cdot I^0_{ro}\cdot t} \tag{5.7}$$

On the other hand, data from test structures exhibit a distinct multi-exponential behavior that requires additional components for a proper fit (Figure 5.4):

$$\hat{g}(\vec{r},t) = \sum_{i=0}^{n-1} \hat{c}_i(\vec{r}) \cdot e^{-\hat{\lambda}_i(\vec{r})\cdot t} \tag{5.8}$$

where n components with ordered switching rates $\hat{\lambda}_i$, $\hat{\lambda}_i > \hat{\lambda}_{i+1}$ and coefficients $\hat{c}_i$ are fitted to the data ('$\wedge$' marks fit results). While we attribute the fastest rate $\hat{\lambda}_0$ to signal from unimpaired RSFP at the focal center, the presence of additional rates suggests the co-existence of RSFP species that exhibit significantly slower switching kinetics. A slowed-down switching observed after fixation supports this notion. Unintended processes during image recording also potentially contribute

to the observed signal behavior. e.g. the re-activation of RSFP by the read-out light which generates a constant background.
Without loss of generality, we assume a position independent mixture of n species with discreet switching rates λ_j. Since the deactivation pattern $h_{3\mathrm{d}}(\vec{r})$ shrinks the effective PSF by a λ-dependent factor, $h_{\mathrm{ef}}(\vec{r},t)$ has to be generalized to a superposition of n individual $h^j_{\mathrm{ef}}(\vec{r})$ that each correspond to a certain λ_j. Furthermore, we assume our experimental parameters chosen such that the in-focus part $h_{\mathrm{fast}}(\vec{r})$ of $h^0_{\mathrm{ef}}(\vec{r})$ obeys the analog to 5.6, and pool the remaining contributions in $h_{slow}(\vec{r})$:

$$\begin{aligned} h_{\mathrm{ef}}(\vec{r},t) &= h_{\mathrm{fast}}(\vec{r},t) + h_{\mathrm{slow}}(\vec{r},t) \\ &:= h_{\mathrm{fast}}(\vec{r}) \cdot e^{-\lambda_0 \cdot I^0_{ro} \cdot t} + \sum_{j=1}^{n-1} h^j_{\mathrm{slow}}(\vec{r}) \cdot e^{-\lambda_j \cdot I_{ro}(\vec{r}) \cdot t} \end{aligned} \tag{5.9}$$

Consequently, the apparent resolution of the acquired image is less than the potential resolution provided by $h_{\mathrm{fast}}(\vec{r})$ and declines over time, as faster components vanish first (Figure 5.4).

In order to access the full image information that is mediated by $h_{\mathrm{fast}}(\vec{r})$, we implemented an unmixing scheme that isolates the fastest switching signal component (rate λ_0), and that we hence termed 'rate-gating': According to 5.4, the image generated by a PSF 5.9 takes on the form:

$$\begin{aligned} g(\vec{r},t) &= g_{\mathrm{fast}}(\vec{r},t) + g_{\mathrm{slow}}(\vec{r},t) \\ &:= g_0(\vec{r}) \cdot e^{-\lambda_0 \cdot I^0_{ro} \cdot t} + \int_0^{\lambda_1} c(\vec{r},\Lambda) \cdot e^{-\Lambda \cdot t} d\Lambda \end{aligned} \tag{5.10}$$

whereby $g_{\mathrm{slow}}(\vec{r},t)$ is represented by a continuum of exponentials with switching speeds $\Lambda \in [0,\lambda_1]$ and coefficients $c(\vec{r},\Lambda)$ as the result of $s \otimes h_{\mathrm{slow}}(\vec{r})$.
Hence, a fit $\hat{g}(\vec{r},t)$ to an imaged structure according to 5.8, in principle, provides a position invariant estimate for $\lambda_0 = \hat{\lambda}_0 / I^0_{\mathrm{ro}}$ by $\hat{g}_{\mathrm{fast}}$, on top of a local approximation of $g_{\mathrm{slow}}(\vec{r},t)$. In practice, however, an insufficient photon count often prohibits local fitting of 5.10. We therefore implemented a robust approximation scheme for $g_{\mathrm{fast}}(\vec{r})$ that only relies on parameters that can be extracted from a fit $\hat{g}(t)$ to the global (i.e. from a region much larger than the corresponding diffraction limit) spatial average $\bar{g}(t)$ of the measured data:

First, we estimate the time t_0 at which the integrated signal exhibits the maximum S/N with respect to g_{fast}:

$$t_0 := \text{argmax}\left(\frac{\int_0^T \bar{g}_{\text{fast}}(t)dt}{\sqrt{\int_0^T \bar{g}_{\text{fast}}(t) + \bar{g}_{\text{slow}}(t)dt}}\right) \tag{5.11}$$

Locally calculated values for t_0 would slightly differ, but as this only affects the statistically error of the result, 5.11 is usually sufficiently precise. Second, we determine a cut-off time t_1 such that

$$g_{\text{fast}}(t) << g_{\text{slow}}(t) \quad (t > t_1) \tag{5.12}$$

which is usually the case for $t_1 = 2t_0$. By further choosing t_2 and t_3 such that $t_i > t_{i+1}$ $(i = 0 \ldots 3)$, we partition the measured signal into time bins $\Sigma_{0,1,2}$ (Figure 5.5),

$$\Sigma_{0,1,2}(\vec{r}) := \int_{0,t_1,t_2}^{t_0,t_2,t_3} g(\vec{r},t)dt \approx F(\vec{r}) + S_0(\vec{r}),\ S_1(\vec{r}),\ S_2(\vec{r}) \tag{5.13}$$

with $F(\vec{r})$ and $S(\vec{r})$ denoting the time integrals over the fast and slow components:

$$F(\vec{r}) := \int_0^{t_0} g_{\text{fast}}(\vec{r},t)dt, \quad S_{0,1,2} := \int_{0,t_1,t_2}^{t_0,t_2,t_3} g_{\text{slow}}(\vec{r},t)dt \tag{5.14}$$

Finally, we estimate $F(\vec{r})$, and thereby $g_0(\vec{r})$, by linear extrapolation in either 0th or 1st order:

$$F(\vec{r})^{0th} := \Sigma_0(\vec{r}) - u \cdot \Sigma_1(\vec{r}) \tag{5.15}$$

$$F(\vec{r})^{1st} := F(\vec{r})^{0th} - v \cdot (\Sigma_1(\vec{r}) - \Sigma_2(\vec{r})) \tag{5.16}$$

with $u, v = u, v(t_{0\ldots3})$ denoting geometrical factors that account for the particular choice of the $t_{0\ldots3}$. Narrowing the integration interval defined by $t_{0\ldots3}$ and moving them closer to $t = 0$, just as the inclusion of the first extrapolation order, reduces the systematic error, but also raises the statistic error due to a reduced photon count. In order to mitigate this effect, the owing to 5.12, we substitute the $\sum_{1,2}$ with their respective resolution neutral local averages, e.g. by applying a Gaussian filter with a FWHM sufficiently far below the FWHM of $h^{1,2}_{\text{slow}}$.

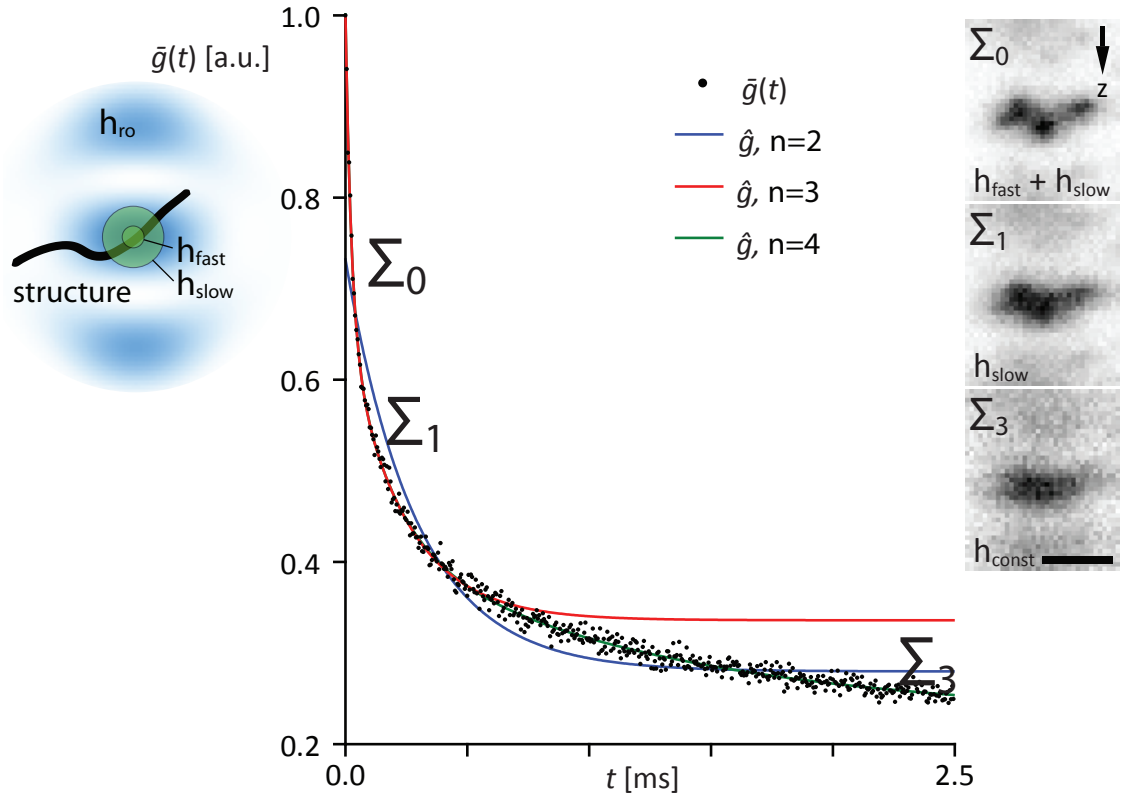

Figure 5.4: Normalized time-resolved, mean fluorescence signal $\bar{g}(t)$ collected from an xz-section through an actin fiber bundle (structure) in a cell expressing Lifeact-DronpaM159T. Target resolution 50 nm, 4Pi read-out pattern $h_{4\mathrm{Pi,ro}}(\vec{r})$ with a total power of $P_{\mathrm{ro}} = 3.1$ µW incident on the sample. An n-component multi-exponential fit to the data corresponds to n apparent switching speeds $\hat{\lambda}_i$. A minimum of n = 3 is required to adequately represent the data from the beginning of the read-out pulse t = 0 up to 0.5 ms, $\hat{\lambda}_i$ = 40.5, 4.3, 0.0 ms^{-1} (for up to 2.5 ms: n = 4, $\hat{\lambda}_i$ = 41, 5.9, 0.85, 0.0 ms^{-1}). Images $\sum_{0,1,3}$ integrated over time regimes that are dominated by fast ($h_{\mathrm{fast}}(\vec{r})$), slow ($h_{\mathrm{slow}}(\vec{r})$) and about constant PSF components ($h_{\mathrm{const}}(\vec{r})$) exhibit a declining resolution. Scale bar: 250 nm.

To confirm the effectiveness of the introduced rate-gating scheme, xz-sections were taken perpendicular to the run of solitary actin fiber bundles.

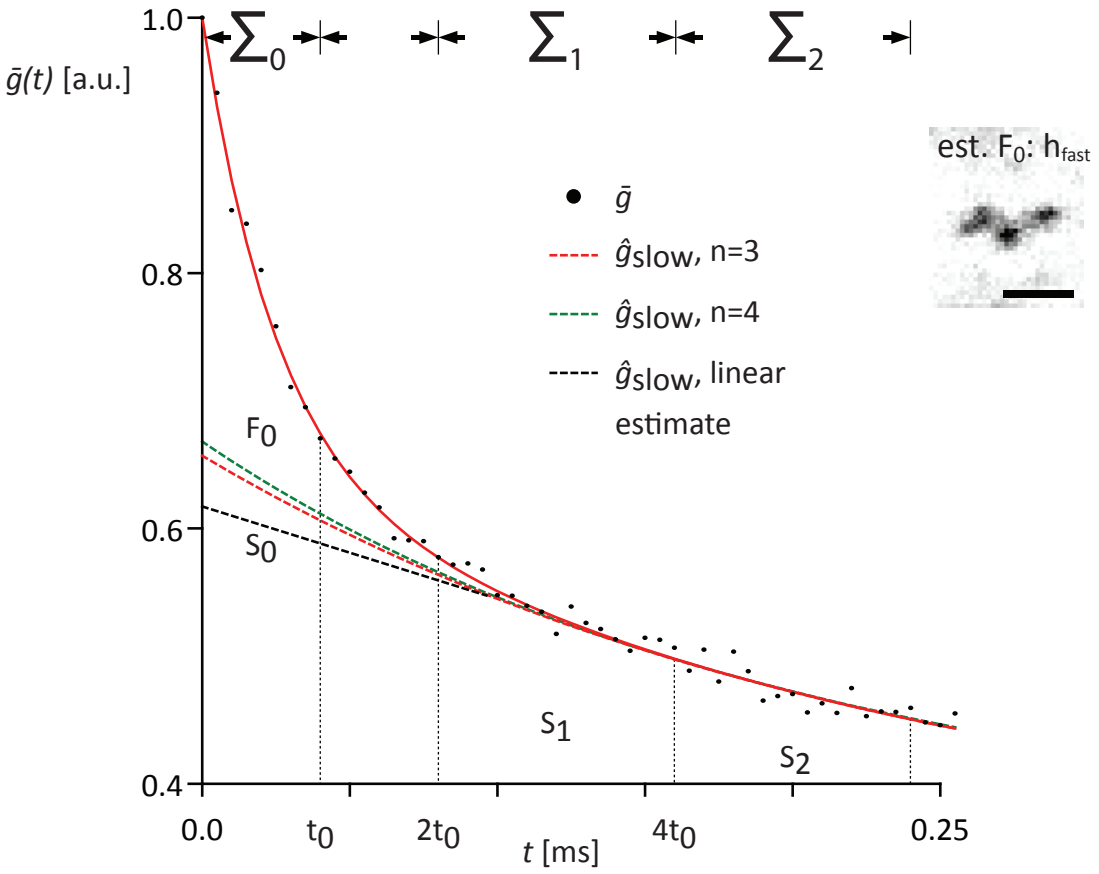

Figure 5.5: Rate-gated 4Pi-RESOLFT; Extrapolation of the initial contribution of $h_{\text{slow}}(\vec{r})(= S_0)$, based on integrated images $\sum_1(\approx S_1)$ and $\sum_2(\approx S_2)$, $t_0 = 40$ µs, provides an estimate of the partial image generated by $h_{\text{fast}}(\vec{r})$ ($F_0 \approx \sum_0 - S_0$, inset), improving resolution and image fidelity over $\sum_0$. Simulation parameters: numerical aperture 1.20, refractive index 1.363, pinhole diameter 0.5 Airy units, E_{ac}, E_{3d}, E_{ro} =1.6 mW · 0.2 ms, 1.3 µW · 1.6 ms, 3.1 µW · 2.5 ms. Scale bar: 250 nm.

The improvement of the image resolution and image fidelity when extracting the fast switching component by removing the slow and the constant contributions are clearly visible in the insets on the left in Figure 5.4 and Figure 5.5.

5.3 Results

Following the schemes introduced in Section 5.1 and in Section 5.2, images of Lifeact labeled with the RSFP Dronpa-M159T expressed in CV-1 (*cercopithecus aethiops monkey kidney*) and HeLa (*human epithelial carcinoma*) cells were recorded in which the rate-gating and the RESOLFT sequence for target resolution of 30-50 nm had been adjusted. The parameters were established by a PSF simulation using measured rate kinetics. The CV-1 and HeLa cells were prepared according the protocol in section A.3, with the plasmid in Section A.4.

Lifeact, a 17-amino-acid peptide, stains filamentous actin (F-actin) structures in eukaryotic cells and tissues. It does not interfere with actin dynamics in vitro and in vivo and in its chemically modified peptide form allows visualization of actin dynamics in nontransfectable cells [123]. Actin filaments are with a diameter of approximately 7 nm the thinnest filaments of the cytoskeleton and are thus perfectly suitable for performance measurement of the built 4Pi-RESOLFT nanoscope. These linear polymers are flexible and relatively strong, resisting buckling by multi-piconewton compressive forces and filament fracture by nanonewton tensile forces [124]. The actin cytoskeleton is crucial for the study of many fundamental biological processes.

Figure 5.6 shows an xz-section taken perpendicular to the run of actin fiber bundles of CV-1 cells. The image confirms the overall shape of the effective PSF (Figure 5.6). It was recorded with an open detection pinhole to boost out-of-focus signal to facilitate the visualization of the overall shape of the effective PSF. The measured (y-integrated) sidelobe structure (Figure 5.6b) closely resembles the numerical prediction (Figure 5.6a). Illumination with the z-doughnut-shaped ($h_{\mathrm{zd}}(\vec{r})$) focus for 1 ms at an average light power of 1.8 µW (488 nm, CW) was sufficient to virtually eliminate lobe background from the image (Figure 5.6c), while the low gradients around the central zero of $h_{\mathrm{zd}}(\vec{r})$ with respect to $h_{3\mathrm{d}}(\vec{r})$ facilitated the mutual alignment of these patterns (Section 3.1). With these constructed sphere-like effective PSF, several xz-sections of more crowded actin filament regions were taken in the following to test the imaging scheme under more challenging conditions (pinhole diameter 0.5 Airy units).

Figure 5.7 indicates how far the performance of the nanoscope can be pushed in finer structured actin networks inside the CV-1 cell body. While one cannot make out the fine structured network in the xz-section in Figure 5.7a, which displays a simulated confocal image of the xz-region, the filaments become visible when the RSFPs are activated and read-out with 4Pi focal pattern according to the scheme introduced in Chapter 4 in Figure 5.7b. Sidelobes were hardly visible and the axial

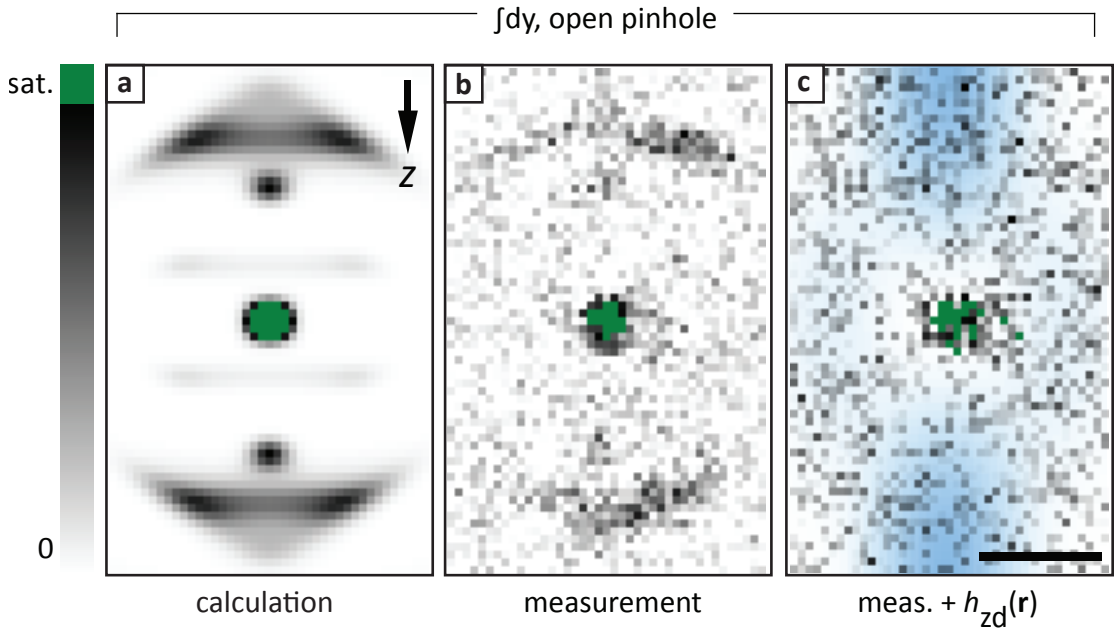

Figure 5.6: Rate-gated xz-section through actin fibers, recorded with open pinhole to boost out-of-focus signal. The measured (y-integrated) sidelobe structure (b) closely resembles the numerical prediction (a) and can be further suppressed (c) by an additional z-doughnut $h_{\mathrm{zd}}(\vec{r})$ (overlay, $E_{\mathrm{zd}} = 1.8\ \mu\mathrm{W} \cdot 1.0$ ms). Simulation parameters: numerical aperture 1.20, refractive index 1.363, E_{ac}, E_{3d}, $E_{\mathrm{ro}} = 1.6$ mW $\cdot$ 0.2 ms, 1.3 µW $\cdot$ 1.6 ms, 3.1 µW $\cdot$ 0.5 ms. Scale bar: 250 nm

extension improved 5-fold to ~ 100 nm, but is still diffraction limited. Figure 5.7c was taken with the additional 3D focal pattern $h_{\mathrm{3d}}(\vec{r})$ in the pulse sequence per pixel of the same xz-section with a pixel size of 7.5 nm. The use of an additional z-doughnut $h_{\mathrm{zd}}(\vec{r})$ was not necessary. Feature sizes well below 40 nm have been measured in this section along different directions as indicated in the Lorentzian fits in Figure 5.7d. Renderings of the volume surrounding the xz-section in Figure 5.7 are shown in Figure 5.8. While the stack in Figure 5.8a was taken without the use of a '3D-doughnut' pattern, the stack in image 5.8b displays the fine structure of the network much clearer when it is applied. A bleaching of the fluorophores during the image recording of the xzy-stack of size 2 µm × 2 µm × 4 µm in image 5.8b could not be observed, which speaks for the gentle handling of the fluorophore in the developed imaging scheme.

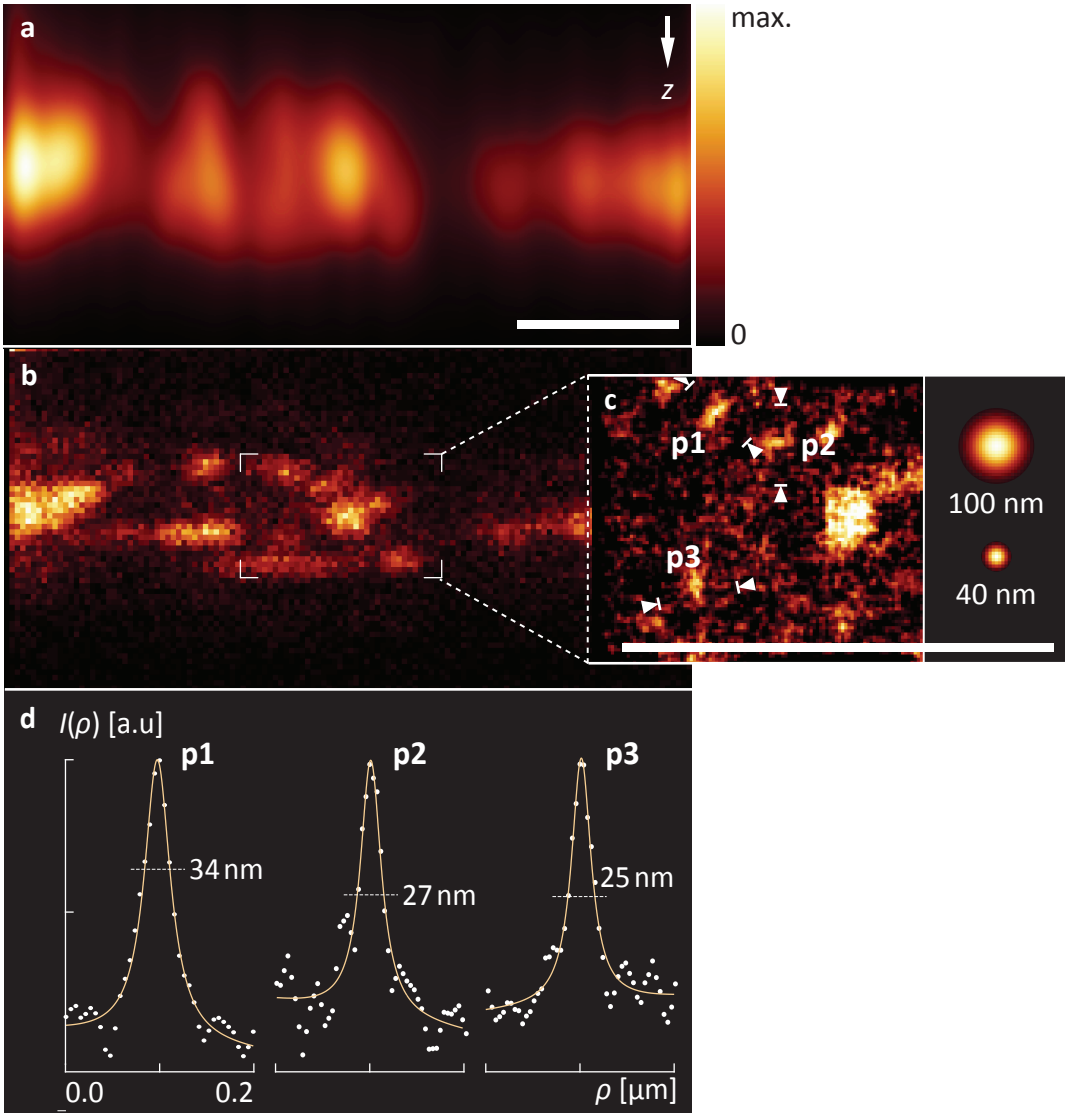

Figure 5.7: 3D 4Pi-RESOLFT nanoscopy (xz-sections). xz-section of actin fiber bundles of living HeLa cells expressing Lifeact-DronpaM159T. (a) Simulated confocal overview (xz-sections). (b) RSFP-based 4Pi microscopy image of the section displayed in (a), actin fiber bundles at an axial base resolution in the 100 nm range. (c) Addition of a 3D deactivation doughnut ($+h_{3d}$, E_{3d} = 2.6 µW · 3.2 ms) to the pulse sequence for 3D 4Pi-RESOLFT nanoscopy reveals Dronpa pattern with apparent feature sizes well below 40 nm (inset, Gaussian reference spheres). (d) Lorentzian fits, plus a linear local background, to box-profiles p1-3 over marked features in (c) along different directions. Numbers indicate full width at half maximum (FWHM) over background. Pulse parameters: E_{ac}, E_{ro} = 1.6 mW · 0.2 ms, 3.1 µW · 2.5 ms. Scale bars 1 µm.

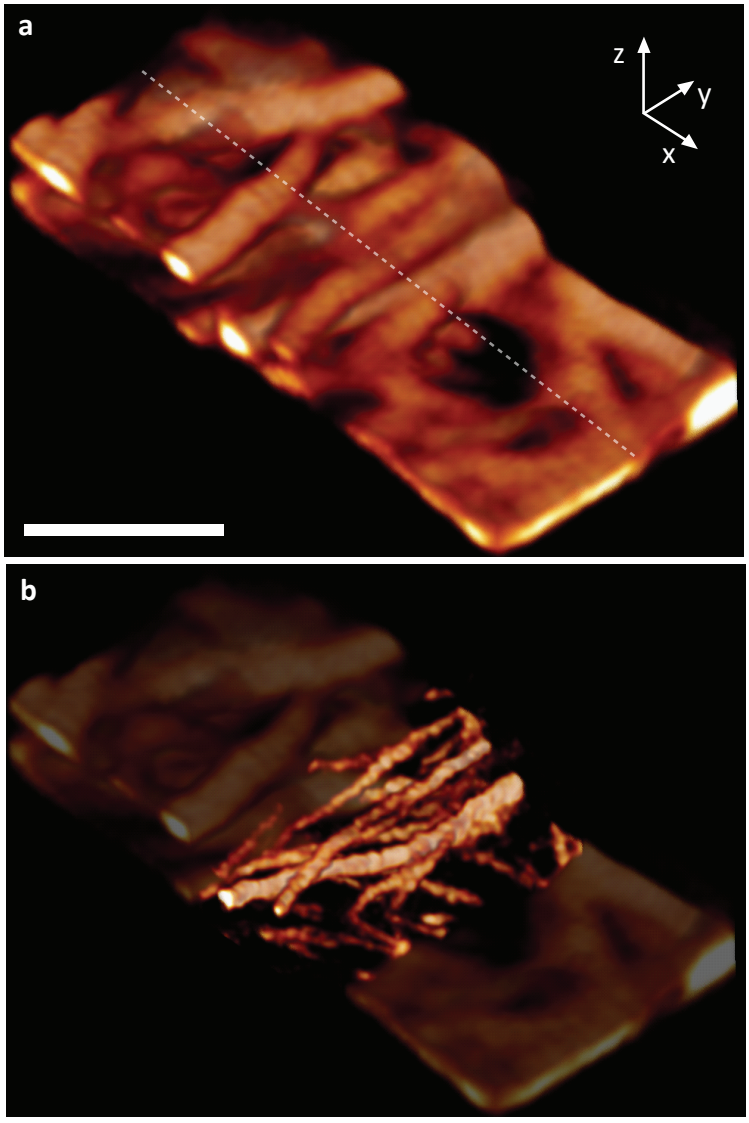

Figure 5.8: 3D 4Pi-RESOLFT nanoscopy (renderings). Renderings of actin fiber bundles of living HeLa cells expressing Lifeact-DronpaM159T. (a) RSFP-based 4Pi microscopy rendering of the volume surrounding the xz-section in Figure 5.7a (dashed line indicates the location of the xz-section), size: 8 µm × 4 µm × 2 µm. (b) 3D 4Pi-RESOLFT nanoscopy rendering of a part of the region in (a) with the addition of a 3D deactivation doughnut (E_{3d} = 1.3 µW · 1.6 ms). size: 2 µm × 4 µm × 2 µm. Additional pulse parameters: E_{ac}, E_{ro} = 1.6 mW · 0.2 ms, 3.1 µW · 2.5 ms. Scale bar 2 µm.

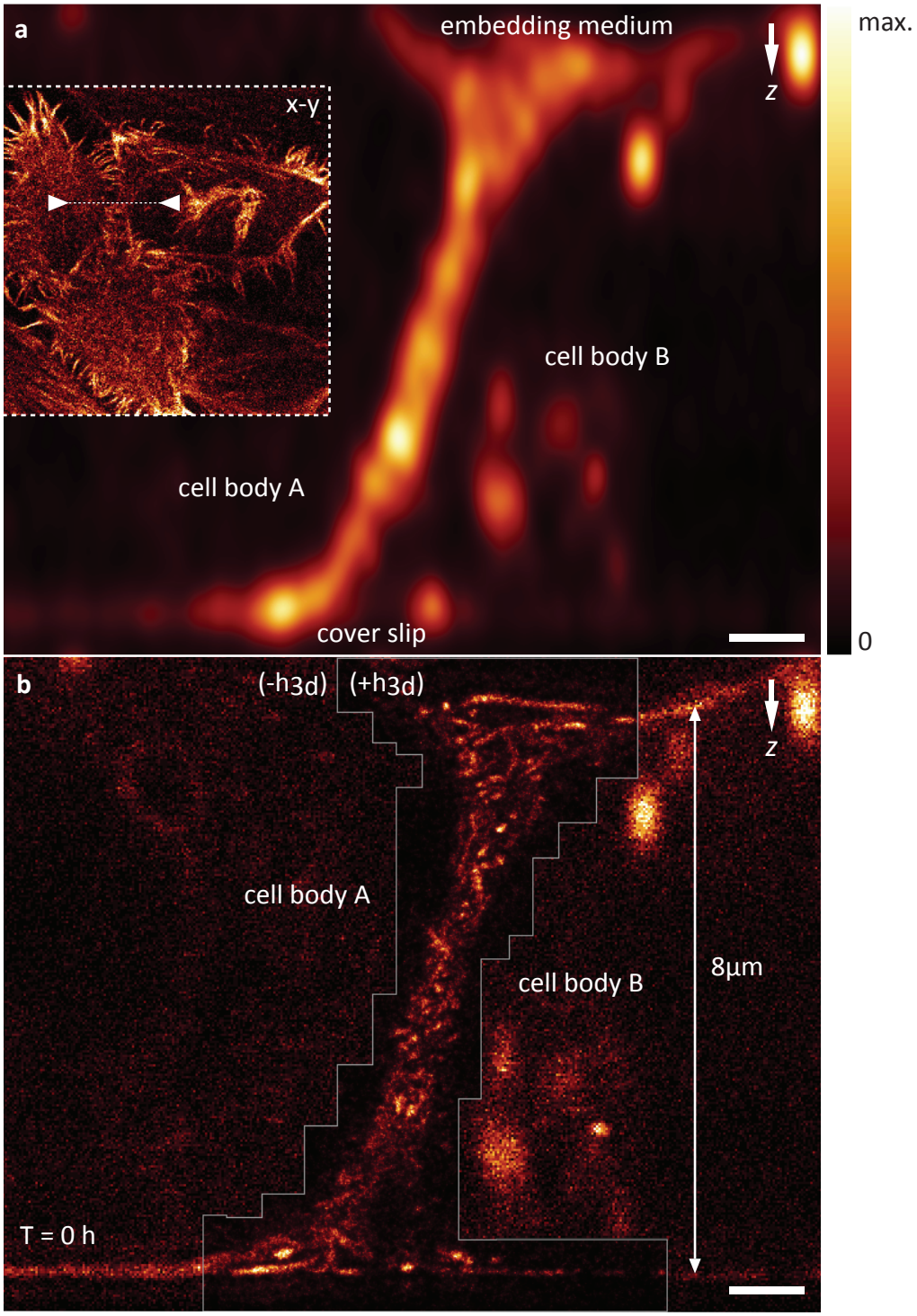
a
embedding medium
z
x-y
cell body B
cell body A
cover slip
max.
0
b
(-h3d)
(+h3d)
z
cell body A
cell body B
8µm
T = 0 h

Particularly challenging areas to image are densely labeled and vertically extended (along the optical axis) regions of living cells. While CV-1 cells, which have been used in the previous examples, grow flat on the cover glass and do not stretch wide along the optical axis (extension along the optical axis: 3-4 µm), HeLa cells grow more compact and develop extended contact regions with other cells (7-9 µm) along the optical axis. Such regions are ideal to evaluate the strong optical sectioning capability of the imaging system. Thus, to test the robustness of the performance of the 4Pi-RESOLFT nanoscope, the vertically extended contact regions of two neighboring HeLa cells were imaged (Figure 5.9).
While in the confocal simulated images (Figure 5.9a) the contact region does not allow to separate individual fibers, a separation of the fibers across the full region of > 8µm depth is possible with 3D 4Pi-RESOLFT nanoscopy (Figure 5.9b) when using the 3D off-switching patterns $h_{3d}(\vec{r})$ and $h_{zd}(\vec{r})$. Despite the challenging imaging conditions, stacked actin structures are unambiguously resolved across the full axial extent of the cell layer. The images were taken at a relaxed target resolution of 50 nm and an acquisition time of 3.3 min/µm^2.

The observation of cell dynamics in time-lapse measurements of the contact region in Figure 5.9 is shown in Figure 5.10. The time evolution of the actin scaffold at the vertical region is clearly visible (grayscale overlays of the preceding time steps).

The recordings show that 3D 4Pi-RESOLFT nanoscopy offers 3D-nanoscale (< 40 nm) imaging of living cells at low-light level (W-kW/cm^2) and strong optical sectioning at densely packed and axially extended cellular regions. All of the displayed figures verify the robust applicability of the constructed sphere-like sub-diffraction effective PSF $h_{ef}(\vec{r})$ in living cells for isotropic nanoscale imaging with the built nanoscope and the implemented imaging routines.

Figure 5.9 *(facing page)*: 3D 4Pi-RESOLFT nanoscopy of a > 8 µm thick, densely labeled, vertical contact region between two adjacent cells (xz-section as marked in the xy-overview in the inset of (a)). (a) Simulated confocal xz-section of the contact region. (b) 3D 4Pi-RESOLFT nanoscopy imaging of the contact region. A narrowed region of interest was generated online from initial overview scans ($-h_{3d}$) at each time frame and imaged at 50 nm target resolution ($+h_{3d}$, gray outline, E_{3d}, E_{zd} = 1.3 µW · 1.6 ms, 1.8 µW · 0.5 ms). Pulse parameters; E_{ac}, E_{ro} = 1.6 mW · 0.2 ms, 3.1 µW · 0.5 ms. Scale bars 1 µm.

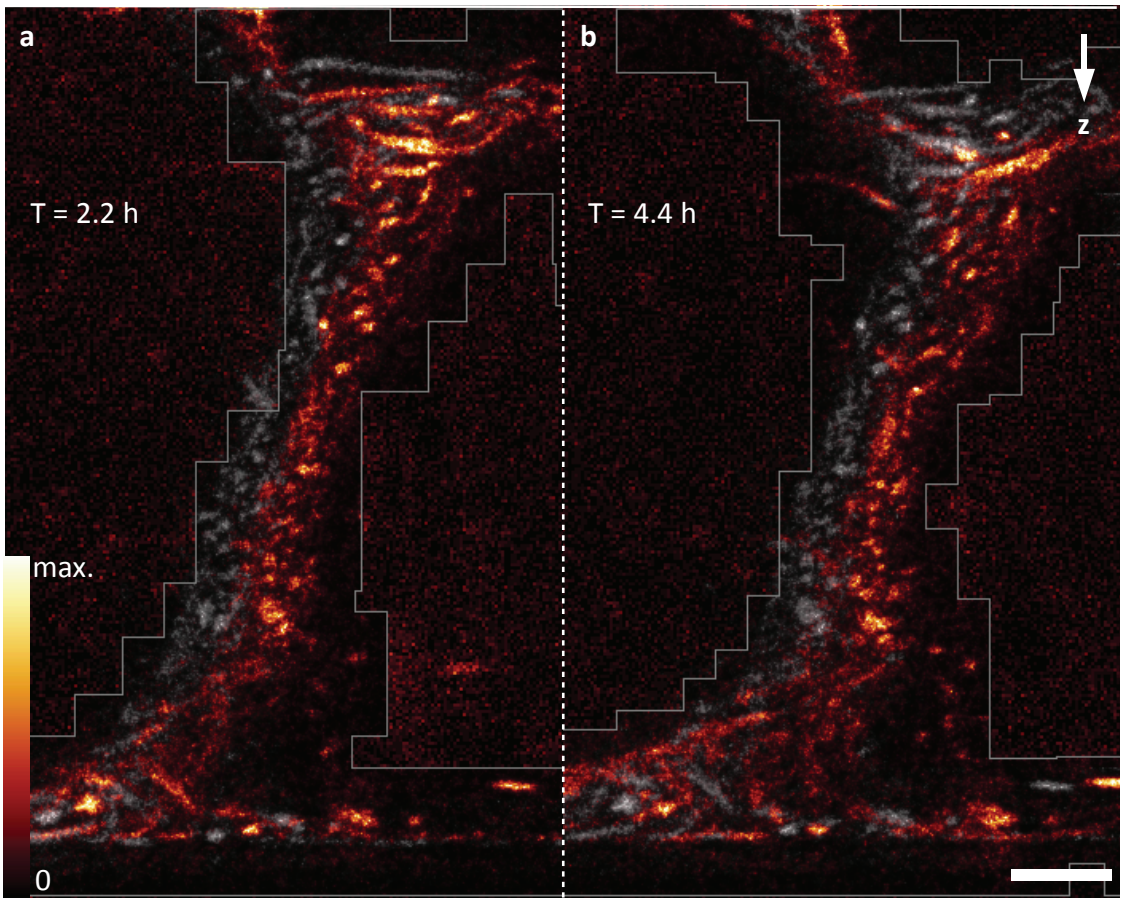

Figure 5.10: Time-lapse recording with 4Pi-RESOLFT nanoscopy of the > 8 µm thick densely labeled vertical contact region between two adjacent cells of Figure 5.9b. Grayscale overlays depict the preceding time step in each case in (a) and (b). Pulse parameters according to Figure 5.9. Scale bar 1 µm.

5.4 Discussion

Chapter 4 showed that the optical sectioning of a 4Pi microscope benefits when using RSFPs because they offer an additional step in order to reach the ON-state: the activation step. Unfortunately, this scheme is still diffraction-limited. Here, the introduced pulse sequence per pixel (Figure 4.2) was expanded by an additional deactivation step with a '3D-doughnut' deactivation pattern (Figure 5.3) to push the resolution even further for isotropic super-resolved images.

Calculations using a vectorial diffraction theory [122] exemplify the improvement brought about by higher order on-switching (Section 2.3) in comparison to modalities of 2^{nd}-order such as those reported in isoSTED microscopy [5] (Figure 5.2).

The recorded images with the introduced scheme show that low-light level (W/cm^2-kW/cm^2) 3D-nanoscale (< 40 nm) imaging of living cells and high optical sectioning and thus robust access to densely packed axially extended cellular regions becomes possible (Section 5.3).

The confinement of the fluorescent on-state, i.e. of $h_{\mathrm{ef}}(\vec{r})$ to sub-diffraction 3D volumes described in this chapter means that fewer fluorophores are interrogated at any point in time. This reduction in number of interrogated molecules (that are inherently co-localized) greatly facilitates the quantitative assessment of the properties of the fluorescent labels as they vary in the sample. In the implemented 'rate-gated' RESOLFT detection scheme, which made use of the system's local sensitivity, it was possible to discriminate individual signal components to improve both the signal-to-noise ratio in the image and the resolution (Section 5.2 and Figure 5.4). Using the current RSFP DronpaM159T, rate-gating allowed to obtain images based on switching speeds (switch half-time $T^{1/2}$ = 10-17 µs at 11.5 kW/cm^2 illumination intensity, section A.6) that were over an order of magnitude faster than the previously reported corresponding values for rapid switching RSFPs ($T^{1/2}$, rsEGFP: 250 µs [75], DronpaM159T: 230 µs [125]). The recording speed of the 4Pi-RESOLFT scheme can be made substantially faster by parallelization using a multi-spot [121] or a line scanning arrangement [126].

Further improvements of 3D 4Pi-RESOLFT nanoscopy could be brought along by the implementation of new 3D switching patterns (like Figure 3.1c or [110]) to better suppress remaining fluorescence in unwanted areas (low off-center amplitudes in Figure 5.1) and by further increase of the on-switching order (e.g. by combining 4Pi-RESOLFT with STED).

Chapter 6

Summary and outlook

In this thesis, I demonstrated the first realization of 4Pi-RESOLFT nanoscopy – a combination of 4Pi microsocpy with RSFP-based RESOLFT nanoscopy to image living cells with a spatially uniform 3D resolution at the nanometer scale.
The use of RSFP-based RESOLFT was particularly attractive because it operates with low light levels which makes it gentle to living cells. Furthermore, optical sectioning benefits from the additional switching step (activation) involved in the RSFP switching cycle to reach the ON-state with respect to modalities that do not make use of a meta-stable state like STED (Chapter 2.3).

For the realization of the project, a 4Pi-RESOLFT nanoscope was designed and built. Furthermore, low-aberration, live-cell 4Pi optics were developed to counteract optical aberrations introduced by (living) cells such that the system could be controlled and stabilized over many hours. The scheme of reducing the global refractive index variance turned out to sufficiently mitigate sample-induced aberrations without adding the complexity associated with adaptive optical elements. The implementation of low-aberration, live-cell optics should also be considered for other live-cell imaging techniques (Chapter 3).

Even without the implementation of the '3D-doughnut' deactivation pattern for sub-diffraction imaging, it was already possible to improve the optical sectioning performance of diffraction-limited 4Pi microscopy with the 4Pi-RESOLFT imaging scheme in living cells. The axial (z) resolutions in recorded images of thick mammalian cells (> 5 µm) were in the range of 100 nm with axial lobes of only ~ 15 % of the main peak of the z-response and did not need mathematical post-processing (i.e. deconvolution) dedicated to lobe-removal that is usually applied in 4Pi-based methods. This improved performance of a 4Pi system for live-cell imaging when using RSFPs stresses the advantages brought along when multiple states are required for the on-switching (Chapter 4).

In order to resolve features below the diffraction limit with the 4Pi-RESOLFT nanoscope, the '3D-doughnut' pattern for the deactivation of RSFPs around the focal center was integrated in the 4Pi-RERSOLFT imaging scheme. In addition a rate-gated detection scheme was implemented which enabled the extraction of a fast switching component from the fluorescence signal which improved the image resolution of the system further. To test the 3D 4Pi-RESOLFT nanoscopy scheme and its strong optical sectioning capability, cellular structures that are more demanding for 3D-superresolution imaging due to their high spatial density and wide axial extension were recorded. It was possible to measure raw and rate-gated image data with isotropic resolution below 40 nm. Furthermore, the rearrangement of the entwined actin fibers in actin networks which appeared particularly crowded and extended over 8 µm along the optic axis could be traced in time-lapse recordings in great detail. All those recordings were conclusive without mathematical post-processing (i.e. deconvolution) (Chapter 5).

The 4Pi-RESOLFT scheme could be improved by the implementation of modified off-switching patterns (e.g. 'aberrated 3D-doughnut' in Section 3.1) and by the use of additional switching steps to increase the on-switching order and thus the optical sectioning performance of the system. Furthermore, the system's recording speed could be improved by the implementation of multi-spot scanning or 4Pi line-scanning arrangements, not forgetting the further improvement of the switching kinetics of the RSFPs.

In summary, one can say that by realizing 4Pi-RESOLFT nanoscopy based on RSFPs, the exceptional optical sectioning in coordinated-targeted far-field fluorescence nanoscopy was demonstrated, which greatly facilitates nanometer scale 3D fluorescence imaging in living cells. Many accepted constraints to the sample have been lifted, which opens up an imaging regime that has so far been systematically avoided.

Appendix

A.1 PSF of a multiphoton type-C 4Pi microscope

The effective point spread function (PSF) $h_{\mathrm{ef}}(\vec{r})$ of a multiphoton 4Pi microscope of type-C is given by the product of the 4Pi detection and the multiphoton 4Pi illumination (read-out) PSFs:

$$h_{\mathrm{ef}}(\vec{r}) = h_{\mathrm{4Pi,det}}(\vec{r}) \cdot h^{m}_{\mathrm{4Pi,ro}}(\vec{r}) \tag{A.1}$$

with

$$\begin{aligned} h_{\mathrm{4Pi,det}}(\vec{r}) &= |\vec{E}_{1,\mathrm{det}}(\vec{r}) + \vec{E}_{2,\mathrm{det}}(\vec{r})|^2 \otimes p(\vec{r}) \\ &= |\vec{E}_{1,\mathrm{det}}(\vec{r}) + \hat{M}\cdot\vec{E}_{1,\mathrm{det}}(\hat{M}\cdot\vec{r})e^{i\phi_1}|^2 \otimes p(\vec{r}) \end{aligned} \tag{A.2}$$

and

$$\begin{aligned} h_{\mathrm{4Pi,ro}}(\vec{r}) &= |\vec{E}_{1,\mathrm{ro}}(\vec{r}) + \vec{E}_{2,\mathrm{ro}}(\vec{r})|^{2m} \\ &= |\vec{E}_{1,\mathrm{ro}}(\vec{r}) + \hat{M}\cdot\vec{E}_{1,\mathrm{ro}}(\hat{M}\cdot\vec{r})e^{i\phi_2}|^{2m} \end{aligned} \tag{A.3}$$

with $\vec{E}_{\mathrm{det}}(\vec{r})$ and $\vec{E}_{\mathrm{ro}}(\vec{r})$ denote the focal field describing the detection and the read-out by a single lens at λ_{fl} and λ_{ro}, respectively. $\phi_{1,2}$ is the phase delay between the two fields which has to be 0 for constructive interferences in case of type-C 4Pi microscopy. $\vec{r}$ is a spatial coordinate originating at the focal point. The transformation matrix $\hat{M}$ considers the orientation of the counterpropagating light fields and is given by:

$$\hat{M} = \begin{pmatrix} 1 & 0 & 0 \\ 0 & 1 & 0 \\ 0 & 0 & -1 \end{pmatrix} \tag{A.4}$$

The function $p(\vec{r})$ describes the the opening of the detector that is conjugated to the focal plane, e.g. the area of a confocal pinhole. If no pinhole is used, $p(\vec{r}) = 1$. The parameter $m = 1, 2, \ldots$ gives the number of photons involved in the read-out process, e.g. $m = 2$ for two-photon excitation.
A detailed description of the 4Pi theory has been given elsewhere [127].

A.2 4Pi unit construction and degrees of freedom

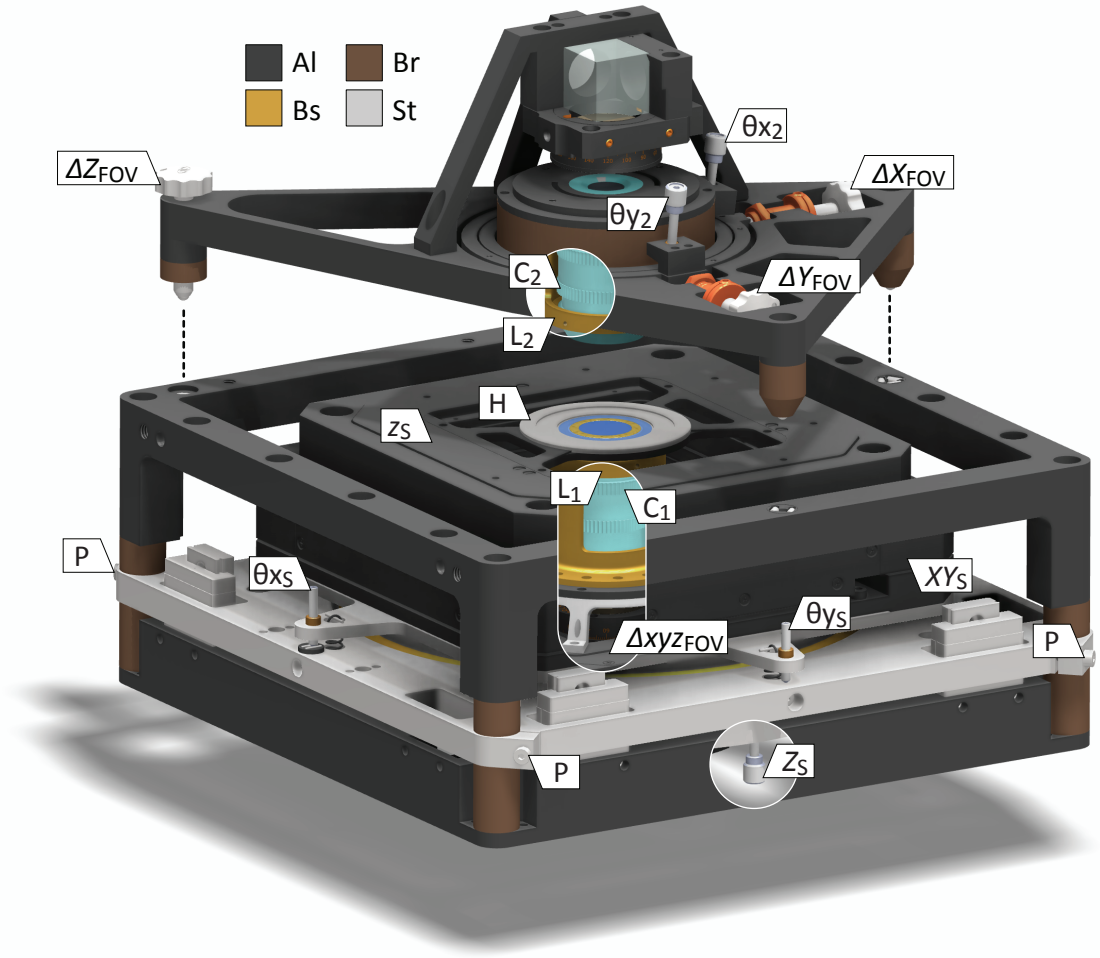

Figure A.1: 4Pi unit construction and degrees of freedom. Correction collars $C_{1,2}$, sample holder H, lens cages $L_{1,2}$, clamp screws P, field of view coarse $\Delta X, Y, Z_{\mathrm{FOV}}$ and fine $\Delta xyz_{\mathrm{FOV}}$ control, sample angle $\theta x, y_s$, upper objective angle $\theta x, y_2$, axial sample position coarse Z_s and fine z_s control, lateral sample position coarse XY_s control. Color coded materials; aluminum alloy Al, bronze Br, brass Bs, stainless steel St.

A.3 Cell culture and sample preparation

HeLa (*human epithelial carcinoma*) and CV-1 (*cercopithecus aethiops monkey kidney*) cells were cultured under constant conditions at 37°C and 5 % CO_2 in DMEM (Invitrogen, Carlsbad, California) containing 5 % FCS (PAA, Pasching, Austria), 100 µg/ml streptomycin, 100 µg/ml penicillin (all Biochrom, Berlin, Germany) and 1 mM pyruvate (Sigma, St. Louis, USA).
'Large' cover glasses (No. 0, diameter 30 mm, hand-selected thickness 100 µm ± 2 µm, Thermo Scientific) were coated with reference beads (FluoSpheres, orange, diameter 100 nm, Life Technologies, Carlsbad, CA, USA) according to a standard Poly-L-lysine protocol [99].
Imaging medium stock solution was prepared as a 15.16 % m/m solution of Polyvinylpyttolidone (PVP40-50G, Sigma-Aldrich, St-Louis, USA) in phenol red-free DMEM (fDMEM, Invitrogen, Carlsbad, CA, California). The refractive index was then adjusted to 1.362 and verified by a refractometer.
Prior to transfection, cells were seeded onto 'small' coverslips (No. 0, 18 mm × 18 mm, hand-selected thickness 100 µm ± 2 µm, Marienfeld, Lauda-Königshofen, Germany) in 6-well plates. On the following day, the cells were transfected with plasmid DNA using Turbofect (Thermo Scientific, Waltham, USA) according to the manufacturer's instructions. 24 hours past transfection, the coverslips were washed for 5 minutes in fDMEM and subsequently covered with 150 µl of a diluted suspension (5 % v/v in fDMEM) of 10 µm beads (FluoSpheres, yellow-green, 10 µm, for blood flow determination, Life Molecular Probes,) that stick to the sample and act as spacers. After 5 minutes of incubation, the coverslips were briefly rinsed with fDMEM to remove non-adherent beads, and immersed into imaging medium for another 20 minutes. For paraformaldehyde (PFA) fixation, the respective samples were incubated for 5 minutes in 4 % PFA solution and washed twice in PBS before the immersion medium was applied. 'Small' cover glasses are then stacked on top of their 'large' counterparts, with cells and beads facing inside. The resulting sandwich is gently weighted down in order to bring glass and spacer into contact, sealed by epoxy resin (UHU Plus Sofortfest, UHU, Bühl, Germany), and finally glued into the sample holder (Figure 3.4) using nail polish.

A.4 Plasmids

In this study, the term 'DronpaM159T' denotes the 'DronpaM159T$^{v2.0}$' variant [103] of the reversibly switchable fluorescent protein Dronpa.

Expression plasmids for Lifeact-DronpaM159T were generated by cloning of the coding sequences of Lifeact [123] and DronpaM159T, connected by the linker GAAGGGGATCCACCGGTCGCCACC, into the vector pcDNA3.1(+) (Clontech, Mountain View, CA, USA).

Expression plasmids for DronpaM159T-tagged vimentin (Vim) were constructed by Gateway vector conversion (Invitrogen, Carlsbad, CA, USA) from the donor vector pDONR223-Vim.

Expression plasmid for DronpaM159T targeted to mitochondria were constructed from the mitochondrial targeting sequence from subunit VIII of human cytochrome C oxidase (from vector pDsRed-Mito, Clontech).

A.5 4Pi microscopy with rsGFP2 in yeast

Baker's yeast, *Saccharomyces cerevisiae*, is the simplest eukaryotic model system. Yeast cells are robust, easy to care for, grow and reproduce quickly. Furthermore, they possess a relatively simple genetic structure that lends itself to easy manipulation. Importantly, being eukaryotes, they share many of the cell structures and cellular mechanisms of mammalian cells.
Here, eisosomes in living yeast were labeled with the negative switching RSFP rsGFP2 [75]. These large, heterodimeric, immobile protein complexes are located at the plasma membrane and mark the site of endocytosis in some eukaryotes [128, 129]. According to electron microscopy measurements eisosomes have a diameter of ~ 50 nm [130].
Due to rsGFP2 different spectroscopic properties [75, 125], is was necessary to increase the activation intensity in the measurements.
Figure A.2 displays the raw data of two xz-sections of yeast cells taken according to scheme 4.2 with profiles over eisosomes. Only minor axial lobes in the 15 % range are visible (like in Figure 4.3). Furthermore, the associated volume rendering in Figure A.3 did not show noticeable bleaching during the measurement process.

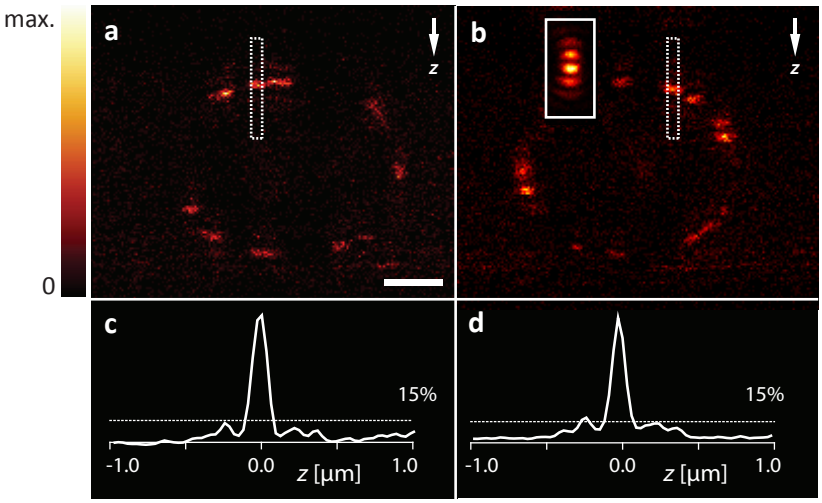

Figure A.2: xz-sections of eisosomes in yeast cells labeled with rsGFP2 with profiles over eisosomes. The interference pattern of a reference bead is clearly visible in b, since it does not contain RSFPs but standard fluorescent dyes and thus can not benefit from the additional activation step to decrease its side lobes. Pulse parameters: E_{ac}, E_{ro} = 3.2 mW · 50 µs, 3.1 µW · 50 µs. Scale bar 1 µm.

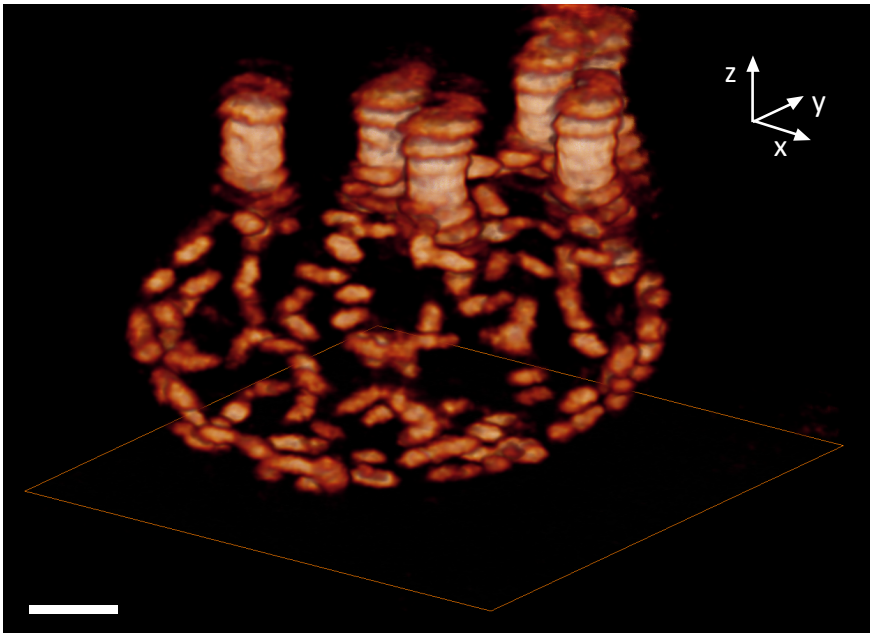

Figure A.3: Volume rendering of eisosomes in yeast cells labeled with rsGFP2. Rendering of the volumes surrounding the sections in Figure A.2 with interference pattern of reference beads at the top. Scale bar 1 µm.

Yeast preparation

Standard methods were used for growth and manipulation of yeast strains [131]. The yeast strain expressing the epitope-tagged fusion protein Pil1-rsEGFP2 was obtained using the protocol described in [132] to endogenously tag YGR086C in BY4741 wildtype yeast cells with rsEGFP2. For imaging, yeast cells growing on agar YPD plates for 24 hours at 25°C were scraped from the plate, washed and mounted in PBS (137 mM NaCl, 3 mM KCl, 8 mM Na_2HPO_4, 1.5 mM KH_2PO_4, pH 7) immediately before imaging.

A.6 DronpaM159T off-switching kinetics

	Data set	λ_0 $[ms^{-1}]$	λ_1 $[ms^{-1}]$	a_0 [0]	a_1 [0]	a_2 [0]	$T_0^{1/2}$ $[\mu s]$
1.	Fig. 5.6 (ctr.)	71	5.6	0.12	0.19	0.69	9.7
2.	Fig. 5.6 (rgt.)	61	4.9	0.11	0.14	0.75	11
3.	Fig. 5.7c	56	4.6	0.046	0.076	0.88	12
4.	Fig. 5.9b	47	4.6	0.17	0.29	0.54	15

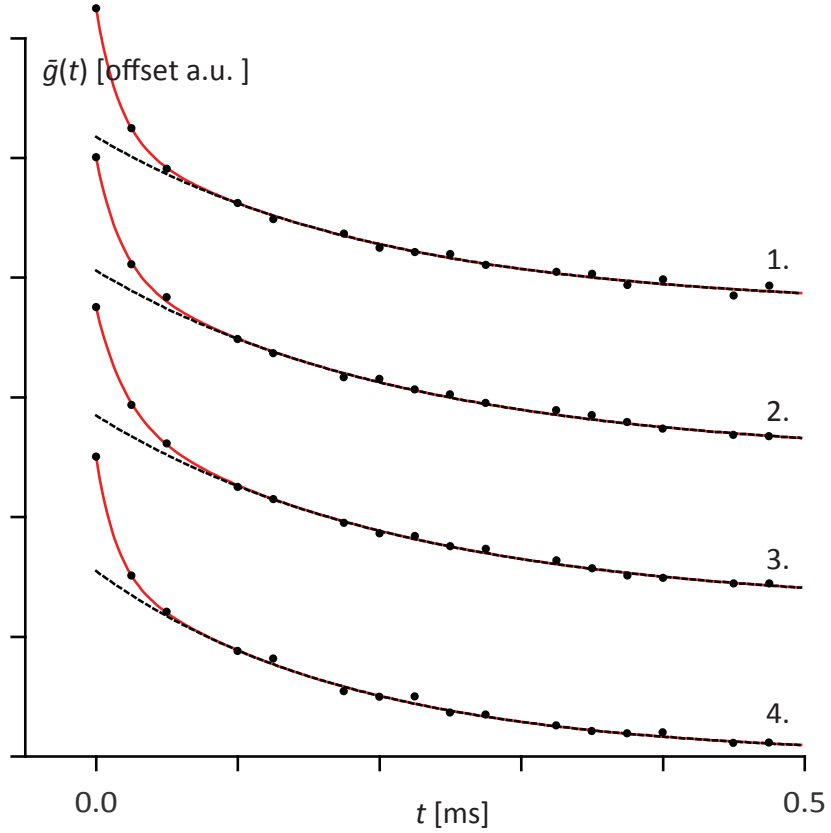

Figure A.4: DronpaM159T off-switching kinetics in living cells. Multi-exponential fits (red line) to spatial average $\bar{g}(t)$ of the indicated data sets, that were measured at a local read out intensity of 11.5 kW/cm^2. Model function $\hat{g}(t) = \sum_{i=0}^{2} a_i \cdot e^{-\lambda_i \cdot t}$, $\lambda_i > \lambda_{i+1}$, $\lambda_2 = 0$. Dotted black lines correspond to the fit less its fastest component ($i = 0$). Switch-off half-time of fastest component $T_0^{1/2} := \ln(2)/\lambda_0$.

A.7 Number of on-factors O^{ON} for different types of microscopes

	det	ac	ro	O^{on}
confocal microscopy	1	0	1	2
STED	1	0	1	2
two-photon confocal microscopy	1	0	2	3
RESOLFT	1	1	1	3
4Pi-RESOLFT with 2ph-activation	1	2	1	4

Bibliography

[1] S. W. Hell, "Double-scanning confocal microscope," *European Patent*, p. 0491289, 1992.

[2] S. Hell and E. H. K. Stelzer, "Fundamental improvement of resolution with a 4Pi-confocal fluorescence microscope using 2-Photon excitation," *Optics Communications*, vol. 93, no. 5-6, pp. 277–282, 1992.

[3] M. Gustafsson, D. A. Agard, and J. W. Sedat, "Sevenfold improvement of axial resolution in 3D widefield microscopy using two objective lenses," *Proc. SPIE*, vol. 2412, pp. 147–156, 1995.

[4] C. Eggeling, K. I. Willig, S. J. Sahl, and S. W. Hell, "Lens-based fluorescence nanoscopy," *Quarterly Reviews of Biophysics*, vol. 48, no. 2, pp. 178–243, 2015.

[5] R. Schmidt, C. Wurm, S. Jakobs, J. Engelhardt, A. Enger, and S. Hell, "Spherical nanosized focal spot unravels the interior of cells," *Nat Methods*, vol. 5, pp. 539–544, 2008.

[6] G. Shtengel, J. A. Galbraith, C. G. Galbraith, J. Lippincott-Schwartz, J. M. Gillette, S. Manley, R. Sougrat, C. M. Waterman, P. Kanchanawong, M. W. Davidson, R. D. Fetter, and H. F. Hess, "Interferometric fluorescent super-resolution microscopy resolves 3D cellular ultrastructure," *Proc Natl Acad Sci U S A*, vol. 106, no. 9, pp. 3125–30, 2009.

[7] S. W. Hell, R. Schmidt, and A. Egner, "Diffraction-unlimited three-dimensional optical nanoscopy with opposing lenses," *Nature Photonics*, vol. 3, no. 7, pp. 381–387, 2009.

[8] M. C. Lang, J. Engelhardt, and S. W. Hell, "4Pi microscopy with linear fluorescence excitation," *Opt Lett*, vol. 32, no. 3, pp. 259–61, 2007.

[9] R. Schmidt, C. A. Wurm, A. Punge, A. Egner, S. Jakobs, and S. W. Hell, "Mitochondrial cristae revealed with focused light," *Nano Lett*, vol. 9, no. 6, pp. 2508–10, 2009.

[10] C. K. Ullal, R. Schmidt, S. W. Hell, and A. Egner, "Block copolymer nanostructures mapped by far-field optics," *Nano Lett*, vol. 9, no. 6, pp. 2497–500, 2009.

[11] P. Kanchanawong, G. Shtengel, A. M. Pasapera, E. B. Ramko, M. W. Davidson, H. F. Hess, and C. M. Waterman, "Nanoscale architecture of integrin-based cell adhesions," *Nature*, vol. 468, no. 7323, pp. 580–U262, 2010.

[12] M. Born and E. Wolf, *Principles of Optics*. Cambridge Univ. Press, Cambridge, 2002.

[13] G. Airy, "On the diffraction of an object-glass with circular aperture," *Transactions of the Cambridge Philosophical Society*, vol. 5, pp. 283–291, 1834.

[14] E. Abbe, "Beiträge zur Theorie des Mikroskops und der mikroskopischen Wahrnehmung," *Archiv fr Mikrokopische Anatomie*, vol. 9, no. 1, pp. 413–418, 1873.

[15] J. Rayleigh, "On the theory of optical images, with special reference to the microscope," *Philos Mag.*, vol. 42, pp. 167–195, 1896.

[16] M. Minsky, *Microscopy apparatus US Patent*. 1961.

[17] J. Pawley, *Handbook of Biological Confocal Microscopy*. New York: Springer, 2006.

[18] T. Wilson and C. J. R. Sheppard, *Theory and Practice of Scanning Optical Microscopy*. New York: Academic Press, 1984.

[19] N. Bloembergen, *Nonlinear Optics*. New York: Benjamin, 1965.

[20] W. Denk, J. H. Strickler, and W. W. Webb, "2-Photon laser scanning fluorescence microscopy," *Science*, vol. 248, no. 4951, pp. 73–76, 1990.

[21] C. J. R. Sheppard and R. Kompfner, "Resonant scanning optical microscope," *Applied Optics*, vol. 17, no. 18, pp. 2879–2882, 1978.

[22] A. Schonle, P. E. Hanninen, and S. W. Hell, "Nonlinear fluorescence through intermolecular energy transfer and resolution increase in fluorescence microscopy," *Annalen Der Physik*, vol. 8, no. 2, pp. 115–133, 1999.

[23] S. W. Hell and E. H. K. Stelzer, "Properties of a 4Pi concofal fluorescence microscope," *Optical Society of America Journal A: Optics, Image Science, and Vision*, vol. 9, pp. 2159–2166, 1992.

[24] J. Bewersdorf, B. T. Bennett, and K. L. Knight, "H2AX chromatin structures and their response to DNA damage revealed by 4pi microscopy," *Proc Natl Acad Sci U S A*, vol. 103, no. 48, pp. 18137–42, 2006.

[25] A. Egner and S. W. Hell, "Fluorescence microscopy with super-resolved optical sections," *Trends Cell Biol*, vol. 15, no. 4, pp. 207–15, 2005.

[26] A. Egner, S. Jakobs, and S. W. Hell, "Fast 100-nm resolution three-dimensional microscope reveals structural plasticity of mitochondria in live yeast," *Proc Natl Acad Sci U S A*, vol. 99, no. 6, pp. 3370–5, 2002.

[27] A. Egner, S. Verrier, A. Goroshkov, H. D. Soling, and S. W. Hell, "4Pi-microscopy of the Golgi apparatus in live mammalian cells," *J Struct Biol*, vol. 147, no. 1, pp. 70–6, 2004.

[28] H. Gugel, J. Bewersdorf, S. Jakobs, J. Engelhardt, R. Storz, and S. W. Hell, "Cooperative 4Pi excitation and detection yields sevenfold sharper optical sections in live-cell microscopy," *Biophys J*, vol. 87, no. 6, pp. 4146–52, 2004.

[29] S. Hell, "Improvement of lateral resolution in far-field light microscopy using two-photon excitation with offset beam," *Opt. Commun.*, vol. 106, pp. 19–22, 1994.

[30] S. Hell and M. Kroug, "Ground-state-depletion fluorescence microscopy: a concept for breaking the diffraction limit," *Appl. Phys. B*, vol. 60, pp. 495–497, 1995.

[31] S. W. Hell and J. Wichmann, "Breaking the diffraction resolution limit by stimulated emission: stimulated-emission-depletion fluorescence microscopy," *Opt Lett*, vol. 19, no. 11, pp. 780–2, 1994.

[32] T. A. Klar and S. W. Hell, "Subdiffraction resolution in far-field fluorescence microscopy," *Opt Lett*, vol. 24, no. 14, pp. 954–6, 1999.

[33] T. A. Klar, S. Jakobs, M. Dyba, A. Egner, and S. W. Hell, "Fluorescence microscopy with diffraction resolution barrier broken by stimulated emission," *Proc Natl Acad Sci U S A*, vol. 97, no. 15, pp. 8206–10, 2000.

[34] S. Bretschneider, C. Eggeling, and S. W. Hell, "Breaking the diffraction barrier in fluorescence microscopy by optical shelving," *Phys Rev Lett*, vol. 98, no. 21, p. 218103, 2007.

[35] S. W. Hell, "Strategy for far-field optical imaging and writing without diffraction limit," *Physics Letters A*, vol. 326, no. 1-2, pp. 140–145, 2004.

[36] S. W. Hell, S. Jakobs, and L. Kastrup, "Imaging and writing at the nanoscale with focused visible light through saturable optical transitions," *Applied Physics a-Materials Science Processing*, vol. 77, no. 7, pp. 859–860, 2003.

[37] M. Hofmann, C. Eggeling, S. Jakobs, and S. W. Hell, "Breaking the diffraction barrier in fluorescence microscopy at low light intensities by using reversibly photoswitchable proteins," *Proc Natl Acad Sci U S A*, vol. 102, no. 49, pp. 17565–9, 2005.

[38] E. Betzig, G. H. Patterson, R. Sougrat, O. W. Lindwasser, S. Olenych, J. S. Bonifacino, M. W. Davidson, J. Lippincott-Schwartz, and H. F. Hess, "Imaging intracellular fluorescent proteins at nanometer resolution," *Science*, vol. 313, no. 5793, pp. 1642–5, 2006.

[39] S. T. Hess, T. P. Girirajan, and M. D. Mason, "Ultra-high resolution imaging by fluorescence photoactivation localization microscopy," *Biophys J*, vol. 91, no. 11, pp. 4258–72, 2006.

[40] M. J. Rust, M. Bates, and X. Zhuang, "Sub-diffraction-limit imaging by stochastic optical reconstruction microscopy (STORM)," *Nat Methods*, vol. 3, no. 10, pp. 793–5, 2006.

[41] B. Harke, J. Keller, C. K. Ullal, V. Westphal, A. Schonle, and S. W. Hell, "Resolution scaling in STED microscopy," *Opt Express*, vol. 16, no. 6, pp. 4154–62, 2008.

[42] J. Keller, "Optimal de-excitation pattern for RESOLFT-microscopy," *Thesis*, 2006.

[43] K. I. Willig, J. Keller, M. Bossi, and S. W. Hell, "STED microscopy resolves nanoparticle assemblies," *New Journal of Physics*, vol. 8, 2006.

[44] M. Dyba and S. W. Hell, "Focal spots of size lambda/23 open up far-field fluorescence microscopy at 33 nm axial resolution," *Phys Rev Lett*, vol. 88, no. 16, p. 163901, 2002.

[45] M. Dyba, S. Jakobs, and S. W. Hell, "Immunofluorescence stimulated emission depletion microscopy," *Nat Biotechnol*, vol. 21, no. 11, pp. 1303–4, 2003.

[46] B. Harke, "3D STED microscopy with pulsed and continuous wave lasers," *Thesis*, 2008.

[47] B. Harke, C. K. Ullal, J. Keller, and S. W. Hell, "Three-dimensional nanoscopy of colloidal crystals," *Nano Lett*, vol. 8, no. 5, pp. 1309–13, 2008.

[48] R. Schmidt, "3D fluorescence microscopy with isotropic resolution on the nanoscale," *Thesis*, 2008.

[49] M. G. Gustafsson, "Nonlinear structured-illumination microscopy: wide-field fluorescence imaging with theoretically unlimited resolution," *Proc Natl Acad Sci U S A*, vol. 102, no. 37, pp. 13081–6, 2005.

[50] R. Heintzmann, T. M. Jovin, and C. Cremer, "Saturated patterned excitation microscopy–a concept for optical resolution improvement," *J Opt Soc Am A Opt Image Sci Vis*, vol. 19, no. 8, pp. 1599–609, 2002.

[51] E. H. Rego, L. Shao, J. J. Macklin, L. Winoto, G. A. Johansson, N. Kamps-Hughes, M. W. Davidson, and M. G. Gustafsson, "Nonlinear structured-illumination microscopy with a photoswitchable protein reveals cellular structures at 50-nm resolution," *Proc Natl Acad Sci U S A*, vol. 109, no. 3, pp. E135–43, 2012.

[52] M. A. Schwentker, H. Bock, M. Hofmann, S. Jakobs, J. Bewersdorf, C. Eggeling, and S. W. Hell, "Wide-field subdiffraction RESOLFT microscopy using fluorescent protein photoswitching," *Microsc Res Tech*, vol. 70, no. 3, pp. 269–80, 2007.

[53] A. Chmyrov, J. Keller, T. Grotjohann, M. Ratz, E. d'Este, S. Jakobs, C. Eggeling, and S. W. Hell, "Nanoscopy with more than 100,000 'doughnuts'," *Nat Methods*, vol. 10, no. 8, pp. 737–40, 2013.

[54] T. J. Gould, J. R. Myers, and J. Bewersdorf, "Total internal reflection STED microscopy," *Opt Express*, vol. 19, no. 14, pp. 13351–7, 2011.

[55] M. Leutenegger, C. Ringemann, T. Lasser, S. W. Hell, and C. Eggeling, "Fluorescence correlation spectroscopy with a total internal reflection fluorescence STED microscope (TIRF-STED-FCS)," *Opt Express*, vol. 20, no. 5, pp. 5243–63, 2012.

[56] P. Bethge, R. Chereau, E. Avignone, G. Marsicano, and U. V. Nagerl, "Two-photon excitation sted microscopy in two colors in acute brain slices," *Biophysical Journal*, vol. 104, no. 4, pp. 778–785, 2013.

[57] P. Bianchini and A. Diaspro, "Fast scanning STED and two-photon fluorescence excitation microscopy with continuous wave beam," *Journal of Microscopy*, vol. 245, no. 3, pp. 225–228, 2012.

[58] J. B. Ding, K. T. Takasaki, and B. L. Sabatini, "Supraresolution imaging in brain slices using stimulated-emission depletion two-photon laser scanning microscopy," *Neuron*, vol. 63, no. 4, pp. 429–437, 2009.

[59] Q. F. Li, S. S. H. Wu, and K. C. Chou, "Subdiffraction-limit two-photon fluorescence microscopy for GFP-tagged cell imaging," *Biophysical Journal*, vol. 97, no. 12, pp. 3224–3228, 2009.

[60] G. Moneron and S. W. Hell, "Two-photon excitation STED microscopy," *Opt Express*, vol. 17, no. 17, pp. 14567–73, 2009.

[61] K. T. Takasaki, J. B. Ding, and B. L. Sabatini, "Live-cell superresolution imaging by pulsed STED two-photon excitation microscopy," *Biophysical Journal*, vol. 104, no. 4, pp. 770–777, 2013.

[62] D. Wildanger, R. Medda, L. Kastrup, and S. W. Hell, "A compact STED microscope providing 3D nanoscale resolution," *J Microsc*, vol. 236, no. 1, pp. 35–43, 2009.

[63] C. Osseforth, J. R. Moffitt, L. Schermelleh, and J. Michaelis, "Simultaneous dual-color 3D STED microscopy," *Opt Express*, vol. 22, no. 6, pp. 7028–39, 2014.

[64] M. Friedrich, Q. Gan, V. Ermolayev, and G. S. Harms, "STED-SPIM: Stimulated emission depletion improves sheet illumination microscopy resolution," *Biophysical Journal*, vol. 100, no. 8, pp. L43–L45, 2011.

[65] T. J. Gould, D. Burke, J. Bewersdorf, and M. J. Booth, "Adaptive optics enables 3D STED microscopy in aberrating specimens," *Opt Express*, vol. 20, no. 19, pp. 20998–1009, 2012.

[66] T. J. Gould, E. B. Kromann, D. Burke, M. J. Booth, and J. Bewersdorf, "Auto-aligning stimulated emission depletion microscope using adaptive optics," *Optics Letters*, vol. 38, no. 11, pp. 1860–1862, 2013.

[67] S. W. Hell, "Microscopy and its focal switch," *Nat Methods*, vol. 6, no. 1, pp. 24–32, 2009.

[68] M. Andresen, M. C. Wahl, A. C. Stiel, F. Grater, L. V. Schafer, S. Trowitzsch, G. Weber, C. Eggeling, H. Grubmuller, S. W. Hell, and S. Jakobs, "Structure and mechanism of the reversible photoswitch of a fluorescent protein," *Proc Natl Acad Sci U S A*, vol. 102, no. 37, pp. 13070–4, 2005.

[69] M. Andresen, A. C. Stiel, S. Trowitzsch, G. Weber, C. Eggeling, M. C. Wahl, S. W. Hell, and S. Jakobs, "Structural basis for reversible photoswitching in dronpa," *Proc Natl Acad Sci U S A*, vol. 104, no. 32, pp. 13005–9, 2007.

[70] S. Habuchi, P. Dedecker, J. I. Hotta, C. Flors, R. Ando, H. Mizuno, A. Miyawaki, and J. Hofkens, "Photo-induced protonation/deprotonation in the GFP-like fluorescent protein Dronpa: mechanism responsible for the reversible photoswitching," *Photochemical Photobiological Sciences*, vol. 5, no. 6, pp. 567–576, 2006.

[71] P. G. Wilmann, J. Petersen, R. J. Devenish, M. Prescott, and J. Rossjohn, "Variations on the GFP chromophore," *Journal of Biological Chemistry*, vol. 280, no. 4, pp. 2401–2404, 2005.

[72] A. C. Stiel, S. Trowitzsch, G. Weber, M. Andresen, C. Eggeling, S. W. Hell, S. Jakobs, and M. C. Wahl, "1.8 A bright-state structure of the reversibly switchable fluorescent protein Dronpa guides the generation of fast switching variants," *Biochem J*, vol. 402, no. 1, pp. 35–42, 2007.

[73] T. Grotjohann, I. Testa, M. Leutenegger, H. Bock, N. T. Urban, F. Lavoie-Cardinal, K. I. Willig, C. Eggeling, S. Jakobs, and S. W. Hell, "Diffraction-unlimited all-optical imaging and writing with a photochromic GFP," *Nature*, vol. 478, no. 7368, pp. 204–8, 2011.

[74] T. Brakemann, A. C. Stiel, G. Weber, M. Andresen, I. Testa, T. Grotjohann, M. Leutenegger, U. Plessmann, H. Urlaub, C. Eggeling, M. C. Wahl, S. W. Hell, and S. Jakobs, "A reversibly photoswitchable GFP-like protein with fluorescence excitation decoupled from switching," *Nat Biotechnol*, vol. 29, no. 10, pp. 942–7, 2011.

[75] T. Grotjohann, I. Testa, M. Reuss, T. Brakemann, C. Eggeling, S. W. Hell, and S. Jakobs, "rsEGFP2 enables fast RESOLFT nanoscopy of living cells," *Elife*, vol. 1, p. e00248, 2012.

[76] A. C. Stiel, M. Andresen, H. Bock, M. Hilbert, J. Schilde, A. Schonle, C. Eggeling, A. Egner, S. W. Hell, and S. Jakobs, "Generation of monomeric reversibly switchable red fluorescent proteins for far-field fluorescence nanoscopy," *Biophys J*, vol. 95, no. 6, pp. 2989–97, 2008.

[77] W. Denk, "Two-photon excitation in functional biological imaging," *J Biomed Opt*, vol. 1, no. 3, pp. 296–304, 1996.

[78] J. Folling, V. Belov, R. Kunetsky, R. Medda, A. Schonle, A. Egner, C. Eggeling, M. Bossi, and S. W. Hell, "Photochromic rhodamines provide nanoscopy with optical sectioning," *Angew Chem Int Ed Engl*, vol. 46, no. 33, pp. 6266–70, 2007.

[79] J. Folling, V. Belov, D. Riedel, A. Schonle, A. Egner, C. Eggeling, M. Bossi, and S. W. Hell, "Fluorescence nanoscopy with optical sectioning by two-photon induced molecular switching using continuous-wave lasers," *Chemphyschem*, vol. 9, no. 2, pp. 321–6, 2008.

[80] A. G. York, A. Ghitani, A. Vaziri, M. W. Davidson, and H. Shroff, "Confined activation and subdiffractive localization enables whole-cell PALM with genetically expressed probes," *Nat Methods*, vol. 8, no. 4, pp. 327–33, 2011.

[81] B. Huang, W. Wang, M. Bates, and X. Zhuang, "Three-dimensional super-resolution imaging by stochastic optical reconstruction microscopy," *Science*, vol. 319, no. 5864, pp. 810–3, 2008.

[82] M. J. Mlodzianoski, M. F. Juette, G. L. Beane, and J. Bewersdorf, "Experimental characterization of 3D localization techniques for particle-tracking and super-resolution microscopy," *Optics Express*, vol. 17, no. 10, pp. 8264–8277, 2009.

[83] I. Izeddin, M. El Beheiry, J. Andilla, D. Ciepielewski, X. Darzacq, and M. Dahan, "PSF shaping using adaptive optics for three-dimensional single-molecule super-resolution imaging and tracking," *Optics Express*, vol. 20, no. 5, pp. 4957–4967, 2012.

[84] M. F. Juette, T. J. Gould, M. D. Lessard, M. J. Mlodzianoski, B. S. Nagpure, B. T. Bennett, S. T. Hess, and J. Bewersdorf, "Three-dimensional sub-100 nm resolution fluorescence microscopy of thick samples," *Nat Methods*, vol. 5, no. 6, pp. 527–9, 2008.

[85] D. Aquino, A. Schonle, C. Geisler, C. V. Middendorff, C. A. Wurm, Y. Okamura, T. Lang, S. W. Hell, and A. Egner, "Two-color nanoscopy of three-dimensional volumes by 4Pi detection of stochastically switched fluorophores," *Nat Methods*, vol. 8, no. 4, pp. 353–9, 2011.

[86] H. L. D. Lee, S. J. Sahl, M. D. Lew, and W. E. Moerner, "The double-helix microscope super-resolves extended biological structures by localizing single blinking molecules in three dimensions with nanoscale precision," *Applied Physics Letters*, vol. 100, no. 15, p. 153701, 2012.

[87] M. K. Lee, P. Rai, J. Williams, R. J. Twieg, and W. E. Moerner, "Small-molecule labeling of live cell surfaces for three-dimensional super-resolution microscopy," *Journal of the American Chemical Society*, vol. 136, no. 40, pp. 14003–14006, 2014.

[88] S. R. Pavani, M. A. Thompson, J. S. Biteen, S. J. Lord, N. Liu, R. J. Twieg, R. Piestun, and W. E. Moerner, "Three-dimensional, single-molecule fluorescence imaging beyond the diffraction limit by using a double-helix point spread function," *Proc Natl Acad Sci U S A*, vol. 106, no. 9, pp. 2995–9, 2009.

[89] S. J. Sahl and W. E. Moerner, "Super-resolution fluorescence imaging with single molecules," *Current Opinion in Structural Biology*, vol. 23, no. 5, pp. 778–787, 2013.

[90] A. S. Backer, M. P. Backlund, A. R. von Diezmann, S. J. Sahl, and W. E. Moerner, "A bisected pupil for studying single-molecule orientational dynamics and its application to three-dimensional super-resolution microscopy," *Applied Physics Letters*, vol. 104, no. 19, 2014.

[91] S. Jia, J. C. Vaughan, and X. W. Zhuang, "Isotropic three-dimensional super-resolution imaging with a self-bending point spread function," *Nature Photonics*, vol. 8, no. 4, pp. 302–306, 2014.

[92] Y. Shechtman, S. J. Sahl, A. S. Backer, and W. E. Moerner, "Optimal point spread function design for 3D imaging," *Phys Rev Lett*, vol. 113, no. 13, p. 133902, 2014.

[93] K. Xu, H. P. Babcock, and X. Zhuang, "Dual-objective storm reveals three-dimensional filament organization in the actin cytoskeleton," *Nat Methods*, vol. 9, no. 2, pp. 185–8.

[94] K. Xu, G. S. Zhong, and X. W. Zhuang, "Actin, spectrin, and associated proteins form a periodic cytoskeletal structure in axons," *Science*, vol. 339, no. 6118, pp. 452–456, 2013.

[95] F. C. Zanacchi, Z. Lavagnino, M. P. Donnorso, A. Del Bue, L. Furia, M. Faretta, and A. Diaspro, "Live-cell 3D super-resolution imaging in thick biological samples," *Nature Methods*, vol. 8, no. 12, pp. 1047–1049, 2011.

[96] H. Shroff, C. G. Galbraith, J. A. Galbraith, and E. Betzig, "Live-cell photoactivated localization microscopy of nanoscale adhesion dynamics," *Nat Methods*, vol. 5, no. 5, pp. 417–23, 2008.

[97] A. R. Small, "Theoretical limits on errors and acquisition rates in localizing switchable fluorophores," *Biophysical Journal*, vol. 96, no. 2, pp. L16–L18, 2009.

[98] P. Annibale, S. Vanni, M. Scarselli, U. Rothlisberger, and A. Radenovic, "Identification of clustering artifacts in photoactivated localization microscopy," *Nature Methods*, vol. 8, no. 7, pp. 527–528, 2011.

[99] C. A. Wurm, D. Neumann, R. Schmidt, A. Egner, and S. Jakobs, "Sample preparation for STED microscopy," *Live Cell Imaging: Methods and Protocols*, vol. 591, pp. 185–199, 2010.

[100] F. Opazo, M. Levy, M. Byrom, C. Schafer, C. Geisler, T. W. Groemer, A. D. Ellington, and S. O. Rizzoli, "Aptamers as potential tools for super-resolution microscopy," *Nature Methods*, vol. 9, no. 10, pp. 938–939, 2012.

[101] K. A. K. Tanaka, K. G. N. Suzuki, Y. M. Shirai, S. T. Shibutani, M. S. H. Miyahara, H. Tsuboi, M. Yahara, A. Yoshimura, S. Mayor, T. K. Fujiwara, and A. Kusumi, "Membrane molecules mobile even after chemical fixation," *Nature Methods*, vol. 7, no. 11, pp. 865–866, 2010.

[102] J. J. Sieber, K. I. Willig, C. Kutzner, C. Gerding-Reimers, B. Harke, G. Donnert, B. Rammner, C. Eggeling, S. W. Hell, H. Grubmuller, and T. Lang, "Anatomy and dynamics of a supramolecular membrane protein cluster," *Science*, vol. 317, no. 5841, pp. 1072–6, 2007.

[103] K. I. Willig, A. C. Stiel, T. Brakemann, S. Jakobs, and S. W. Hell, "Dual-label STED nanoscopy of living cells using photochromism," *Nano Lett*, vol. 11, no. 9, pp. 3970–3, 2011.

[104] I. Testa, N. T. Urban, S. Jakobs, C. Eggeling, K. I. Willig, and S. W. Hell, "Nanoscopy of living brain slices with low light levels," *Neuron*, vol. 75, no. 6, pp. 992–1000, 2012.

[105] W. Vandenberg, M. Leutenegger, T. Lasser, J. Hofkens, and P. Dedecker, "Diffraction-unlimited imaging: from pretty pictures to hard numbers," *Cell and Tissue Research*, vol. 360, no. 1, pp. 151–178, 2015.

[106] M. Schneider, S. Barozzi, I. Testa, M. Faretta, and A. Diaspro, "Two-photon activation and excitation properties of PA-GFP in the 720-920-nm region," *Biophysical Journal*, vol. 89, no. 2, pp. 1346–1352, 2005.

[107] S. W. Hell, "Toward fluorescence nanoscopy," *Nat Biotechnol*, vol. 21, no. 11, pp. 1347–55, 2003.

[108] K. I. Willig, S. O. Rizzoli, V. Westphal, R. Jahn, and S. W. Hell, "STED microscopy reveals that synaptotagmin remains clustered after synaptic vesicle exocytosis," *Nature*, vol. 440, no. 7086, pp. 935–9, 2006.

[109] E. Auksorius, B. R. Boruah, C. Dunsby, P. M. P. Lanigan, G. Kennedy, M. A. A. Neil, and P. M. W. French, "Stimulated emission depletion microscopy with a supercontinuum source and fluorescence lifetime imaging," *Optics Letters*, vol. 33, no. 2, pp. 113–115, 2008.

[110] X. Hao, E. S. Allgeyer, M. J. Booth, and J. Bewersdorf, "Point-spread function optimization in isoSTED nanoscopy," *Optics Letters*, vol. 40, no. 15, pp. 3627–3630, 2015.

[111] V. Tuchin, *Handbook of Optical Biomedical Diagnostic*, vol. PM107. SPIE Press, Washington, 2002.

[112] A. Egner, M. Schrader, and S. W. Hell, "Refractive index mismatch induced intensity and phase variations in fluorescence confocal, multiphoton and 4pi-microscopy," *Optics Communications*, vol. 153, no. 4-6, pp. 211–217, 1998.

[113] S. H. Deng, L. Liu, Y. Cheng, R. X. Li, and Z. Z. Xu, "Effects of primary aberrations on the fluorescence depletion patterns of STED microscopy," *Optics Express*, vol. 18, no. 2, pp. 1657–1666, 2010.

[114] S. Berning, "STED nanoscopy of the living brain," *Thesis*, 2011.

[115] M. Schuster, "Adaptive Optik in der STED-Mikroskopie - Verbesserung der Auflösung in dicken Proben," *Masterarbeit*, 2012.

[116] R. Arimoto and J. M. Murray, "A common aberration with water-immersion objective lenses," *J Microsc*, vol. 216, no. Pt 1, pp. 49–51, 2004.

[117] D. S. Wan, M. Rajadhyaksha, and R. H. Webb, "Analysis of spherical aberration of a water immersion objective: application to specimens with refractive indices 1.33-1.40," *J Microsc*, vol. 197, no. Pt 3, pp. 274–84, 2000.

[118] S. W. Hell, M. Schrader, and H. T. van der Voort, "Far-field fluorescence microscopy with three-dimensional resolution in the 100-nm range," *J Microsc*, vol. 187, no. Pt 1, pp. 1–7, 1997.

[119] R. Schmidt, J. Engelhardt, and M. Lang, "4Pi Microscopy," *Methods Mol Biol*, vol. 950, pp. 27–41, 2013.

[120] M. C. Lang, T. Staudt, J. Engelhardt, and S. W. Hell, "4Pi microscopy with negligible sidelobes," *New Journal of Physics*, vol. 10, pp. 1–13, 2008.

[121] A. Egner, "Multifokale hochauflösende 3D-Fluoreszenzmikroskopie," *Thesis*, 2002.

[122] B. Richards and E. Wolf, "Electromagnetic diffraction in optical systems. 2. structure of the image field in an aplanatic system," *Proceedings of the Royal Society of London Series a-Mathematical and Physical Sciences*, vol. 253, no. 1274, pp. 358–379, 1959.

[123] J. Riedl, A. H. Crevenna, K. Kessenbrock, J. H. Yu, D. Neukirchen, M. Bista, F. Bradke, D. Jenne, T. A. Holak, Z. Werb, M. Sixt, and R. Wedlich-Soldner, "Lifeact: a versatile marker to visualize F-actin," *Nature Methods*, vol. 5, no. 7, pp. 605–607, 2008.

[124] M. P. Murrell and M. L. Gardel, "F-actin buckling coordinates contractility and severing in a biomimetic actomyosin cortex," *Proceedings of the National Academy of Sciences of the United States of America*, vol. 109, no. 51, pp. 20820–20825, 2012.

[125] I. Testa, E. D'Este, N. T. Urban, F. Balzarotti, and S. W. Hell, "Dual channel RESOLFT nanoscopy by using fluorescent state kinetics," *Nano Lett*, vol. 15, no. 1, pp. 103–6, 2015.

[126] F. Curdt, "4Pi Nanoscopy parallelized by line scanning," *Thesis*, 2013.

[127] M. Nagorni and S. W. Hell, "Coherent use of opposing lenses for axial resolution increase in fluorescence microscopy. i. comparative study of concepts," *J Opt Soc Am A Opt Image Sci Vis*, vol. 18, no. 1, pp. 36–48, 2001.

[128] T. C. Walther, J. H. Brickner, P. S. Aguilar, S. Bernales, and P. Walter, "Eisosomes mark static sites of endocytosis," *Nature*, vol. 439, no. 7079, pp. 998–1003, 2006.

[129] G. Grossmann, J. Malinsky, W. Stahlschmidt, M. Loibl, I. Weig-Meckl, W. B. Frommer, M. Opekarova, and W. Tanner, "Plasma membrane microdomains regulate turnover of transport proteins in yeast," *Journal of Cell Biology*, vol. 183, no. 6, pp. 1075–1088, 2008.

[130] V. Stradalova, W. Stahlschmidt, G. Grossmann, M. Blazikova, R. Rachel, W. Tanner, and J. Malinsky, "Furrow-like invaginations of the yeast plasma membrane correspond to membrane compartment of can1," *Journal of Cell Science*, vol. 122, no. 16, pp. 2887–2894, 2009.

[131] F. Sherman, "Getting started with yeast," *Guide to Yeast Genetics and Molecular and Cell Biology, Pt B*, vol. 350, pp. 3–41, 2002.

[132] A. De Antoni and D. Gallwitz, "A novel multi-purpose cassette for repeated integrative epitope tagging of genes in saccharomyces cerevisiae," *Gene*, vol. 246, no. 1-2, pp. 179–185, 2000.

List of Figures

List of Figures

List of Publications

Parts of this thesis have been published in the following publication:

1. U. Boehm, S. W. Hell, and R. Schmidt. "4Pi-RESOLFT nanoscopy," (submitted).

Preliminary work for the project was part of the following publication:

1. C. K. Ullal, S. Primpke, R. Schmidt, U. Boehm, A. Egner, P. Vana, S. W. Hell. "Flexible Microdomain Specific Staining of Block Copolymers for 3D Optical Nanoscopy," *Macromolecules*, vol. 44, no. 19, pp. 7508-7510, 2011.

Contributions to conferences:

1. U. Boehm, R. Schmidt, S. W. Hell (2015) *Live cell 4Pi nanoscopy.* Talk at the 15th international European Light Microscopy Initiative (ELMI) meeting, Sitges, Spain.
2. U. Boehm (2015) *STED Nanoscopy: From Principles to Applications.* Invited Talk at the XLAB, Göttingen, Germany.
3. U. Boehm, S. W. Hell, R. Schmidt (2015) *4Pi-RESOLFT nanoscopy.* Flash Talk and Poster at the symposium Seeing is Believing - Imaging the Processes of Life, Heidelberg, Germany.
4. U. Boehm (2015) *Far-field optical nanoscopy: principles and recent advancements.* Invited Talk at the Deutsche Physikerinnen Tagung, Göttingen, Germany.

Acknowledgments

Achieving the results presented in this thesis has been facilitated by many people who I am very thankful for their support and help

Prof. Dr. Stefan W. Hell for giving me the opportunity to work on the exciting projects, any stimulating discussions and ideas as well as for providing an environment that allows to carry out the research with high efficiency.

Prof. Dr. Rainer Fink for agreeing to be the second referee, and **Prof. Dr. Christian Enss** and **Prof. Dr. Matthias Bartelmann**, for being the remaining members of the examining board.

Roman Schmidt, **Johann Engelhardt** and **Alexander Egner** for sharing many insights on 4Pi microscopy and support with the project.

Tim Grotjohann and **Ilaria Testa** for sharing many insights on RSFPs and RESOLFT microscopy in the initial phase of the project.

Marco Roose and **Björn Thiel** for their software support.

Francisco Balzarotti and **Jaydev Jethwa** for sharing many insights on electronics and lasers.

Tanja Gilat, **Ellen Rothermel**, **Carola Gregor**, **Daniel Jans**, **Nickels Jensen** and **Christian Wurm** for the supply with cells, plasmids and know-how.

Udo Gemm, **Frank Meyer** and all members of the electronic workshop for their fast and reliable support.

Mario Lengauer, **Rainer Schürkötter** and all members of the precision mechanics workshop for their excellent manufacturing and adjustment of mechanical components.

Wolfgang Kluge for the silver-coating of hundreds of cover glasses.

Jaydev Jethwa, **Nicolai Urban** and **Jan Keller-Findeisen** for proofreading the manuscript.

Our secretaries **Julia Guhlich**, **Stefanie Kruse**, **Sarah Leondarakis** and **Alena Stephan** for their competent and fast support with all kind of paperwork.

The whole NanoBiophotonics department including former members and guests for their support and creating a friendly atmosphere at work.

Meinem Bruder Christian für Deinen bedingungslosen Rückhalt. Vielen Dank, dass Du die letzten Jahre immer für mich da warst!